Università degli Studi della Calabria

Facoltà di Scienze MM. FF. NN.

Dottorato di Ricerca in Fisica
XVII Ciclo (FIS/05)

Tesi di Dottorato

Three-Dimensional Hybrid Code for Earth's Magnetotail Dynamics

Dottorando:

Rosita De Bartolo

Supervisore:
prof. Gaetano Zimbardo,
dott.ssa Antonella Greco

Coordinatore:
prof. Gennaro Chiarello

2002 — 2006

A mio padre

Oggi non ci sarai. Nè domani, nè il giorno che verrá dopo domani. Questo é il mio dolore. Te ne sei andato una sera di Settembre, in silenzio, con la dignitá che ha segnato la tua vita. Ricordo l'ultima volta che mi hai salutato, con respiro affannoso hai detto: "A domani". Avrei cambiato vita con vita per vederti arrivare a quel domani, per vederti vecchio. Ricordo le passeggiate a parlare dei nipoti che avresti voluto avere, le discussioni animate su tutto, i consigli che mi davi, le paure...ricordi quando mi hai insegnato a guidare? Sapevi che avrei preso subito la macchina e cercavi di opporti. Lo sapevi perché io e te siamo uguali, stesso carattere, stessa forza e perseveranza. E questa perseveranza mi ha portato qui, e anche se tu ormai non sei piú, voglio pensarti come eri, pensare che mi ascolti e mi sorridi...pensare che ancora vivi.
Ciao, Papá.

Contents

Chapter 1

Introduction

This work is dedicated to the development and exploitation of a new three-dimensional (3D) particle code for equilibrium plasma configurations. The code is of the so-called hybrid type, that is ions are treated as particles and electrons as fluid. The development of the code involved the use of techniques such as ion tracing, semi-Lagrangian methods, quadratic interpolation on a 3D grid, and 3D fast Fourier transforms. An iterative procedure was developed to asses the convergence of the required solution. The code has been applied to the study of the equilibrium structure of the Earth's magnetotail current sheet. Investigating such a structure has become a major scientific challange since the unambiguos detection, by the Cluster spacecraft, of bifurcated current sheets. We have obtained a relatively wide class of solutions for the current sheet structure, and we found that the double peak current profile is due to electrons when the ions are injected into an Harris-like quasi-neutral sheet, computing ion moments on a 3D grid in space, and the electron fluid equations are solved with appropriate boundary conditions.
A detailed comparison of the simulation results with in situ spacecraft observations is carried out, too, showing that our solutions are consistent with the experimental data.

1.1 Solar-Wind Magnetosphere Interactions

The sun generates a strong *solar wind*, which is quite different from our surface winds created by differences in our atmospheric pressures. The *solar wind* is a flow of ionized solar plasma and a remnant of the solar magnetic field that pervades interplanetery space. It is a result of the huge difference in gas pressure between the solar corona and interstellar space. This pressure

difference drives the plasma outward, despite the restraining influence of solar gravity. The existence of a solar wind was surmised in the 1950*s* [70, 27, 66] on the basis of the evidence that small variations in the Earth's magnetic field (geomagnetic activity) were produced by observable phenomena on the sun (solar activity), as well as from theoretical models for the equilibrium state of the solar corona. It was first observed directly and definetively by space probes in the mid-1960*s*.

Measurements taken by spacecraft-borne instruments since that time (and until recently) have yielded a detailed description of the solar wind across an area from inside the orbit of Mercury to well beyond the orbit of Neptune and, lately, of the solar wind termination shock. Solar-wind observations and theory have been the subject of several books [71, 12, 40] and a continuing series of conferences summarizing new research (e.g., [73]). Why has this distant and tenuos plasma been the subject of sustained interest in the scientific community? The answer to this question stems from two important aspects of solar-wind research.

The first of these concerns the role of the solar wind in the interdisciplinary subject known as *solar-terrestrial relations*. The solar wind is significantly influenced by solar activity (or, in physical term, by changes in the solar coronal conditions and magnetic field) and transmits the influence to planets, comets, dust particles, and cosmic rays that are immersed in the wind. The origin of the solar influence through interaction of the solar magnetic field with the expanding coronal plasma has become a major topic in present-day solar-wind research. The second important aspect of solar-wind research that helps to explain the sustained interest in the subject concerns the physical processes that occur in its formation and expansion from the hot solar corona to the cool and far more tenuos regions of the outer solar system. This expansion causes the magnetized plasma through huge variations in its properties; for example, collisions among ions or electrons in the expanding plasma are frequent in the corona, but extremely rare in interplanetary space. Thus the physics of this plasma system can be examined under a wide variety of conditions, some of which are difficult to attain in terrestrial laboratories or in the immediate vicinity of the Earth. Yet the solar wind is accessible to space probes, and its properties can be measured and its physical processes studied at a level of detail impossible for most astrophysical plasmas.

1.1.1 A brief Survey of Solar Wind Properties

The solar wind carries about one million tons of hot plasma, at a temperature of about 10^5 K, away from the sun every second. Solar wind plasma contains a mixture of 95.9% protons (H+) and 4% α particles (He2+). The remaining 0.1% is made up of ions of other elements, including carbon, nitrogen, oxygen, neon, magnesium, silicon, and iron and enough electrons to electrically balance all the positive ions. The exact composition has been routinely measured on Ulysses and ACE, two spacecraft carrying a Solar Wind Ion Composition Spectrometer. The plasma behaves like an electrically conducting fluid, carrying with it a magnetic field arising from systems of electrical currents within the sun's corona. The strength of this magnetic field decreases with increasing distance from the sun.
Because plasma particles have sufficient kinetic energy to escape the sun, the solar wind becomes an extension of the sun's corona, continuously present in the interplanetary space. Evidence of the solar wind has been observed well beyond the orbit of Neptune, at a distance of about 88 AU by Voyager II and 94 AU by Voyager I.
Solar wind streams move at different speeds. When streams collide, they produce regions of strong, turbulent magnetic fields. After escaping from the sun's gravitational field, the solar wind flows radially outward. A rotating garden sprinkler is a good analogy. Each drop moves straight out from the source, but the pattern rotates. The streams' travel speeds vary from 300 to 1000 km/sec and are independent of their distance from the sun. The density of the solar wind varies between 1 and 10 particles/cm^3 at the orbit of Earth and diminishes with the inverse square of the distance from the sun's center.

1.1.2 The Geomagnetic Tail

Solar activity can cause sporadic order-of-magnitude fluctuations of the solar wind parameters, however.
The solar wind has a negligible effect on the movements of planets, but it can have other profound effects in their immediate vicinity.
So what has protected the Earth's atmosphere, its water supply, and its inhabitants from the searing effect of the solar wind? The ionized gases of the solar wind are prevented from striking the Earth's atmosphere by its magnetic field. Earth, infact, is one of the planets that has a strong internal magnetic field. In the absence of any external drivers, the geomagnetic field can be approximated by a dipole field with an axis tilted about 11 degrees from the spin axis. The forcing by the solar wind is able to modify this field, creating a cavity called the magnetosphere. This cavity shelters the surface

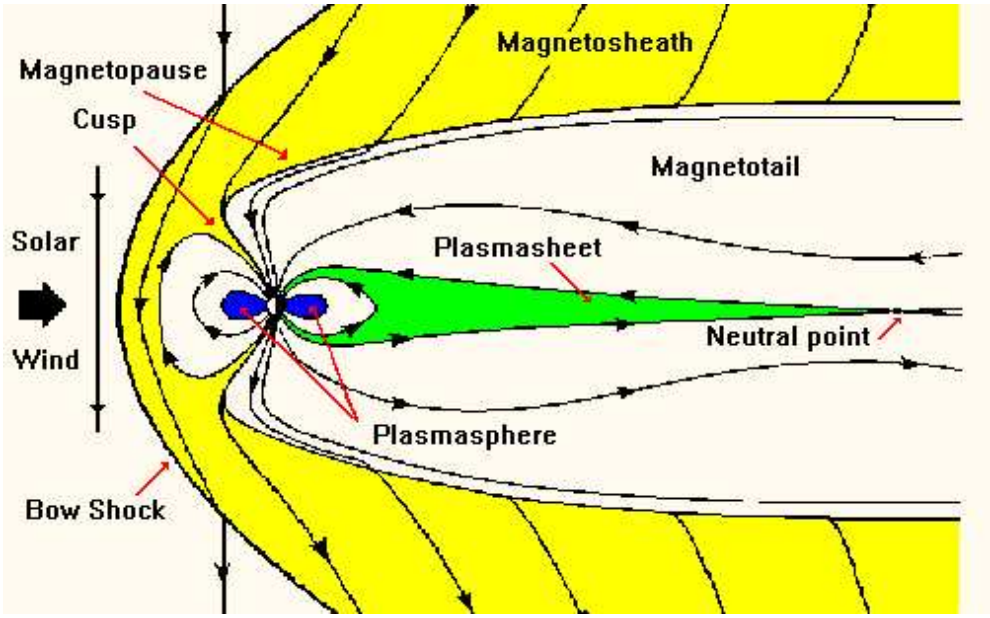

Figure 1.1: Schematic of Earth's magnetosphere. The solar wind flows from left to right.

of the planet from the high energy particles of the solar wind.
The Earth's magnetosphere and the solar wind do not interact smoothly. When the solar wind plasma flows past the Earth, it has difficulty penetrating into the planet's magnetic field. This leads to the creation of a huge bow-shaped shock wave, similar to that of the wake of a speed boat moving through water, which deflects the solar wind around the magnetopause. The bow shock, which marks the limit of the Earth's magnetic influence, occurs where the velocity of solar wind particles decreases from supersonic to subsonic speeds.

The solar wind compresses the Earth's magnetic field on the sunward side, and, as the magnetic field accompanying the solar-wind plasma partially merges with that of the planet, the planetary field is stretched into a magnetotail, an elongated "wake" on the side opposite the sun. The geomagnetic tail is a region of great importance to the magnetosphere, for, as we shall see, it acts as a reservoir of plasma and energy. The energy and the plasma are released into the inner magnetosphere aperiodically during magnetically disturbed episodes called magnetospheric substorms.
The length of the Earth's magnetotail was determined by spacecraft instrumentation to be at least several million kilometers long. This part of the magnetosphere is quite dynamic, since large changes can take place there,

and ions and electrons are often energized.
Most of the volume of the tail is taken up by two large bundles of nearly parallel magnetic field lines. In the bundle north of the equator, the magnetic field points earthwards and leads to a roughly circular region including the northern magnetic pole, while in the southern bundle the magnetic field points away from Earth and is linked to the southern polar region. These two bundles, known as the "tail lobes", extend far from Earth: ISEE-3 and Geotail found them well-defined even at 200-220 R_E (Earth radii) from Earth. At those distances the lobes are already penetrated by some solar wind plasma, but near Earth they are almost empty.

The extremely low tail lobe density suggests that field lines of the lobe ultimately connect to the solar wind, somewhere far downstream from Earth. Ions and electrons then can easily flow away along lobe field lines, until they are swept up by the solar wind; but very, very few solar wind ions can oppose the wind's general flow and head upstream, towards Earth. With such a one-way traffic, rather little plasma remains in the lobes.
Separating the two tail lobes is the "neutral plasma sheet", a layer of weaker magnetic field and denser plasma, centered on the equator and typically 2-6 Earth radii thick. Unlike field lines of the tail lobes, those of the plasma sheet do cross the equator, though they are quite stretched out. A weak magnetic field means that the plasma is less restrained here than nearer to Earth, and on occasion it sloshes or flaps around.

In the early $1960s$, spacecraft observations estabilished the existence of the tail. The hystory of those early observations has been reviewed by [65]. Those early measurements showed that the geomagnetic field strength in the near-Earth tail (that is, at about 10-20 R_E from the Earth) lobes is about 20 nT. Here we shall use this one observational parameter, together with parameters derived from observations of the Earth's polar ionosphere, the polar cap, to derive the basic properties of the tail. The magnetic flux from each tail lobe connetcs to one of the polar caps. By requiring that the magnetic flux be conserved between the polar cap and the tail lobe, we can obtain an estimate of the radius of the tail. The polar cap is the area around the geomagnetic pole bounded by the auroral oval. The flux leaving the polar cap, given by integral of the vertical component of the field strength over the area of the polar cap, is:

$$\Phi_{PC} = 2\pi(R_E \sin\theta_{PC})^2 B_0$$

where θ_{PC} is the colatitude of the equatorward edge of the polar cap (assumed circular), and B_0 is the equatorial field strength (half the polar field strength). This must equal the flux in a tail lobe (assumed to be a semicircle in the

cross section):

$$\Phi_T = \frac{1}{2}\pi R_T^2 B_T \tag{1.1}$$

where R_T is the tail radius and B_T is the magnetic-field strength in the tail lobe. Equating the fluxes in the tail lobe and the polar cap gives:

$$\frac{R_T}{R_E} = \left(\frac{4B_0}{B_T}\right)^{\frac{1}{2}} \sin\theta_{PC}$$

Taking $\theta_{PC} = 15^o$, $B_0 = 31000$ nT and $B_T = 20$ nT, we find $R_T = 20R_E$; if $B_T = 10$ nT (which is more typical of the distant tail), $R_T = 29R_E$. In a static tail there must be pressure equilibrium between the tail lobe and both the plasma sheet and the solar wind. We can use this to estimate the plasma sheet properties and the geometry of the distant tail. Equating the magnetic pressure (which is much larger than the particle pressure) in the tail lobes with the particle pressure (which is much larger than the magnetic pressure) in the plasma sheet, we find

$$\frac{B_T^2}{2\mu_0} = nk(T_i + T_e)$$

where n is the particle number density in the plasma sheet, k is the Boltzmann constant and T_i and T_e are the ion and electron temperatures, respectively. Again, using $B_T = 20$ nT, we get a plasma sheet pressure of 0.24 nPa or 1500 eV cm^{-3}. This argument tells us nothing about n or T separately, but agrees well with typical plasma sheet parameters of $n \sim 0.3$ cm^{-3}, $T_i \sim 4.2$ keV, and $T_e \sim 0.6$ keV [11]. We can calculate the current that must be carried by this plasma by applying Ampere's law across the current sheet. The total change in magnetic field across the plasma sheet is twice the lobe field strength, because the fields on either side are equal in size but oppositely directed. So:

$$\Delta B = 2B_T = \mu_0 I$$

Where I is the sheet height-integrated current density. Again, using $B_T = 20$ nT gives $I = 30$ mAm^{-1}. This may appear to be a rather small current, until we consider the length of the current sheet. This same current height-integrated density can also be given as 30 Akm^{-1} or 2×10^5 AR_E^{-1}. Thus, 10^6 A is carried in each $5R_E$ of the length of the tail, which means that the diversion of only a small part of the tail current is sufficient to explain the ionospheric auroral electrojet currents observed during substorms.

Pressure balance across the tail magnetopause was used by [18] to deduce how the tail radius increases with the distance down the tail or how the tail

flares. If the tail flares there will be a component of the solar wind dynamic pressure normal to the tail magnetopause. So the normal pressure used in the balance must include a component of the dynamic pressure plus an isotropic pressure p_0, which includes both thermal and magnetic pressures. Balancing this with the tail-lobe magnetic pressure gives:

$$\rho u_{sw}^2 \sin^2 \alpha + p_0 = \frac{B_T^2}{2\mu_0}$$

where $\rho = n(m_e + m_i)$ is the mass density and the subscript sw in the flow speed refers to solar wind.
The tail flaring angle α is related to the increase in tail radius with distance,

$$\frac{dR_T}{dx} = \tan \alpha$$

and the magnetic field strength in the lobe, B_T, is given by

$$B_T(x) = \frac{2\Phi_T}{\pi R_T^2(x)}$$

where Φ_T is the total magnetic flux in one tail lobe and equals Φ_{PC}. We shall assume that Φ_T is not a function of downtail distance. Neither of these assumptions is strictly true, but as we shall see, over a limited range of distances along the tail axis the amount of flux crossing both of these boundaries is small. If α is small so that $\sin \alpha \sim \tan \alpha = dR_T/dx$, where x is positive in the antisolar direction, then:

$$\rho u_{sw}^2 \left(\frac{dR_T}{dx}\right)^2 + p_0 = \frac{1}{2\mu_0}\left(\frac{2\Phi_T}{\pi R_T^2}\right)^2$$

Rearranging, we get:

$$M^2 \left(\frac{dR_T^2}{dx}\right)^2 + 1 = \left(\frac{R_*}{R_T}\right)^4 \tag{1.2}$$

where $M = (\rho u_{sw}^2/p_0)^{\frac{1}{2}}$ is the solar-wind Mach number (sonic or Alfvén, depending on the dominant part of p_0) and

$$R_* = \left(\frac{2\Phi_T^2}{\mu_0 \pi^2 p_0}\right)^{\frac{1}{4}} \tag{1.3}$$

is the asymptotic radius of the tail. Rewriting equation (1.2) we get

$$\frac{dR_T}{dx} = \frac{1}{M}\left[\left(\frac{R_*}{R_T}\right)^4 - 1\right]^{\frac{1}{2}} \tag{1.4}$$

Integrating equation (1.4) and applying an earthward boundary condition that $R_T = R_0$ at $x = x_0$ gives

$$\frac{x - x_0}{MR_*} = \int_{R_0/R_*}^{R_T/R_*} \frac{dr}{(r^{-4} - 1)^{\frac{1}{2}}} \tag{1.5}$$

where $r = R_T/R_*$. The distant downtail at which tail flaring ceases, x_*, is finite and can be estimated by evaluating equation (1.5) for the case $R_T = R_*$. Ref. [18] shows that this gives

$$x_* - x_0 \simeq MR_* \left[0.6 - \frac{1}{3}(R_0/R_*)^3 \right] \tag{1.6}$$

Taking as the solar-wind parameters $M = 9$ and $p_0 = 3.2 \times 10^{-11}$ Nm^{-2}, the estimate of Φ_T from equation (1.1) as 4.3×10^8 Wb and the initial tail radius and distance as $R_0 = 18R_E$ and $x_0 = 10R_E$ yields $R_* \sim 27R_E$ and $x_* \sim 140R_E$ and an asymptotic lobe field strength of 9 nT. Thus, the tail reaches an asymptotic radius when the magnetic pressure of the lobes balances the thermal pressure of the solar wind. This occurs at around $150R_E$, but clearly depends on solar-wind conditions. Numerical estimates for geotail properties, starting from rather simple assumptions of static equilibrium, show that these estimates agree remarkably well with observations.

1.2 Hybrid Codes

In many plasmas, in particular in space science, protons govern much of the essential physics. However, electron effects usually appear on much smaller spatial and temporal scales. For more than two decades, scientists have refined computational models that concentrate on the dominating and larger-scale ion kinetic physics, while treating the much ligher electrons, presumably less important, as a charge-neutralizing fluid.
These physics-based, algorithmic model descriptions are called *hybrid codes*, which have estabilished an invaluable position for themselves - clearly distinct from Magnetohydrodynamic (MHD) calculations, but simpler and much more efficient than full-particle simulations. Broadly speaking, there are three main techniques used to address issues concerning plasma physics: methods that examine the behaviour of single charged particles (Vlasov method, the PIC method, Monte Carlo simulation, test particle method); statistical methods (*i.e*, solving the kinetic equation for the particle distribution function); and fluid theory.

MHD methods have an important role in plasma research. This is attributable to the relative simplicity of their mathematical description (compared with the methods of kinetic theory) and their ability to produce highly graphic descriptions due to the use of averaged characteristics. The MHD codes are based on the fluid equations, that is plasma dynamics problem is approached from the point of view of a fluid. Depending on the nature of the problem, the plasma can be treated by the multiple fluid equations describing the different species present or the single fluid description can be used.

Although the MHD approximation has been successfully used for several decades, the MHD theory is incaple of adeguately describing certain small scale phenomena that are of considerable interest in physics. The MHD approximation breaks down for very weak magnetic fields, in the magnetic field dissipation region at small scales, where electron and ion motion decouple, such as, in thin current sheets like the magnetopause and the magnetotail neutral sheets. The validity of MHD model is doubtful also in the presence of strong currents parallel to the magnetic field, in these cases, adeguate description of plasma behaviour requires using the kinetic theory.

Numerical models describing the hydrodynamic behaviour of plasma ignore physical effects that are of considerable interest in some applications. Moreover, the MHD equations do not describe physical processes that take place at distances of the order of several ion inertial lengths. The MHD approach has the advantage of being able to use large cells with a superior computational performance compared with particle simulations.

On the other hand, kinetic models, that address the problem of plasma dynamics by addressing the motion of individual particles, produce a description of plasma behaviour which is too detailed for macroscopic global scale studies. Kinetic codes are the most accurate numerical simulation approach available for the simulation of plasma dynamics, but complete simulation, with all plasma components represented by a collection of discrete particles, is very difficult problem because of excessive computer resource requirements (primarly computer time): the electrons with relatively large electron plasma frequency ω_{pe} and electron gyrofrequency Ω_{ce} have to be advanced at a relatively small Δt_e, while the ions, with much smaller ion plasma frequency ω_{pi} and ion gyrofrequency Ω_{ci}, have to be advanced at a relatively large Δt_i. Moreover spatial scale must include the Debye length in a plasma and the number of particles that, although large, is never anywhere as large as in nature (tipically 10^7 particles).

On one hand, MHD codes cannot capture all the physics in these plasma problems, (e.g. finite Larmor radius effect). On the other hand, full particle codes are computationally demanding and it is not possible to simulate such

large scale phenomena in three dimensions.
To model phenomena that occur on ion inertia and gyroradius scales, which fall between longer scales obtained by magnetohydrodynamic simulations and shorter scales attainable by full particle simulations, it makes sense to use hybrid codes, that is codes which assume different models of the medium for different plasma components. In hybrid algorithms one or more ion species are treated kinetically via standard PIC methods, Monte Carlo simulations or test particle methods used in particle codes and the electrons are treated as a single charge neutralizing massless fluid.
Physical processes in a magnetized plasma are fairly often studied by applying the particle method for the ion component only, while the electrons are considered as a fluid. Although all hybrid codes have similar properties, there are differences in their numerical implementation. This primarily concerns the methods used to solve the field equations. Much experience has been gained over time on these numerical properties. In recent years, the majority of published computations have used one of the three following types: a direct solver (one-pass method) [104, 69], the predictor-corrector scheme [15, 28, 78], a modified predictor-corrector scheme [44, 47, 68], and algorithms based on the moment method [78, 57]. Other variations of the hybrid code employ a tensor description of the electron pressure [111] and retain a finite electron mass term [54, 109], or simply include a different numerical method for the electric field solver and magnetic field advance [102].
Here, we develop a stationary conventional (particle ions and massless electrons) hybrid code. In such a model, the plasma is assumed quasi-neutral, and the displacement current is ignored in the Maxwell equations. In this approximation, the motion of plasma particles should be regarded as nonrelativistic. The quasi-neutrality condition assumes the the electron density is almost equal to the ion density. To trace the evolution of the system on long time and large spatial regions, the fast electron dynamics must be completely eliminated. This is accomplished by using hybrid codes, in which ions are treated as particles and electrons as a massless fluid ($m_e = 0$).
The general scheme of hybrid calculations can be described as follow:

- the electromagnetic fields are determined from the Ampere and Faraday equations;
- the parallel electric field is determined from the equation of motion of the electron component of the plasma;
- the dynamics of the ion component is simulated by particle integration method and the macroscopic ion characteristics are determined (as the moments of the ion distribution function);
- the electron temperature is obtained from its relation with the ion temper-

ature.

For simulation of physical processes in outer space, electrons are often considered in the isothermal or adiabatic approximation.
This work address the development and use of a hybrid particle code approach to magnetotail-like simulations.

1.3 Magnetotail Current Sheets

In space physics, current sheets play a key role. According to the Alfvén terminology [1], current sheets are the physical active regions, the processes in which determine the situation in the ambient physical passive space. These are fundamental structures for many physical phenomena, appearing mainly at the contact of different magnetic field configurations, for example in the Earth magnetopause, which separates the solar wind magnetic field from the magnetospheric field, and at the central plasma sheet in the magnetotail of the Earth's magnetosphere that separates oppositely directed magnetic fields.
The structure of the magnetotail has attracted much attention both on the theoretical and observational point of view. Literature on hybrid simulation of magnetotail current sheets provides results quite good at reproducing tail global configuration. Since the first analytical work by [30] our view of the tail has changed a lot; in previous years the theory was mostly based on one simplest 1D solution, known as Harris sheet. Its basic property is that both current and plasma density vary across the sheet as $\cosh^{-2}(z/L)$, whereas the sheet is considered as isothermal (with T_e=T_i) and with equal contributions from protons and electrons to the electric current.
The one-dimensional (1D) current sheet due to Harris is the simplest analytical description. Harris showed that this description is self-consistent using either MHD or kinetic theory. In a Harris neutral sheet, the magnetic field and plasma pressure are given by:

$$B(z) = B_0 \tanh(z/h)\hat{x}$$

$$p(z) = p_0 \cosh^{-2} z/h$$

It is simple to verify that the total pressure is constant in this structure. So the plasma pressure at the center of the neutral sheet balances the pressure of the asymptotic value of the magnetic field B_0 far from the sheet, where the plasma pressure becomes negligible. To complete this description of the

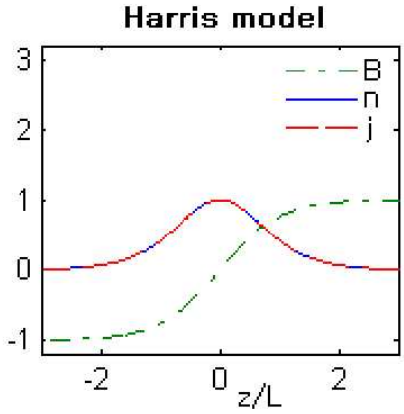

Figure 1.2: Equilibrium profiles of the density, magnetic field and current density.

current sheet , we can obtain the current from Ampere's law:

$$(\nabla \times \mathbf{B})_y = B_0 \frac{d}{dz}\left(\tanh\frac{z}{h}\right) = \frac{B_0}{h}\cosh^{-2}\frac{z}{h} = \mu_0 j_y(z)$$

and show that there is force balance between the gradient of pressure and the $\mathbf{j} \times \mathbf{B}$ force.

$$\mathbf{j} \times \mathbf{B} = \frac{B_0^2}{\mu_0 h}\cosh^{-2}\left(\frac{z}{h}\right)\tanh\left(\frac{z}{h}\right)\hat{z} =$$
$$= \frac{d}{dz}p_0\cosh^{-2}\left(\frac{z}{h}\right)\hat{z} = \nabla p$$

In the last 40 years, the semplicity of this current sheet has resulted in its often being used in theoretical models. The tail-like current sheets exhibts additionally a small component of the normal magnetic field [51, 52].
On the other hand, spacecraft observations have shown that the magnetotail current sheet exhibits a variety of different profiles, even during quiet (non disturbed) times. These profiles are often different from the Harris j current profile reported above (Figure 1.2).
Bifurcated current sheets have been observed or inferred in the near-Earth [90] or in the distant tail [39] and more recently and with great detail (using Cluster data) in the middle tail at about 20 R_E [63, 80, 81, 91]. The thickness of the current sheet and its dynamical structure has also been studied in the near-Earth magnetotail, using Geotail data [3, 5]; the current sheet

temporarily forms a double-peaked current sheet in which the current density becomes the largest away from the neutral sheet. Recent analysis of Voyager 2 data has shown that bifurcated current sheet can be found in Jupiter's magnetotail, too [41].
Such current sheets even exhibit magnetic overshoots, beside the double peak [60, 91, 116], which imply a current profile very different from the simple Harris sheet. Even when the magnetotail current profile is not bifurcated, it often exhibits a thin current sheet embedded in a thick plasma sheet, which again is different from the Harris solution, where the constant V_y velocity implies that the current profile coincides with the density profile (see Figure 1.2). Therefore, an investigation of current sheet structure which allows for a variety of solutions, different from the Harris one, is strongly needed. If such equilibrium solutions are obtained, an appropriate parametric study can allow to understand which physical conditions determine a given current profile.

1.4 Hybrid Simulations of Magnetotail Current Sheets

Hybrid simulation of the one-dimensional current sheet in the magnetotail has been used in [75, 14, 17]. The structure of the x-independent (one-dimensional) forced current sheet including a self-consistent B_y component is investigated for the case of small normal field component. A hybrid simulation model is used to demonstrate that such a current sheet has a time-dependent structure which radiates incompressible Alfvén waves with amplitude of the order of the asymptotic (lobe) field strength B_0 [75]. A one-dimensional, hybrid simulation code is used to study current sheets with a non-zero normal magnetic field B_z and a dawn-to-dusk electric field E_y. Such configurations are dependent upon only two parameters: the normalized normal magnetic field b_n and the drift velocity v_D [14]. One-dimensional hybrid simulations of the current sheet have been carried out for parameters corresponding to a quiet tail (v_D, b_n $<<1$) [17]. The determination of the properties of the distribution function of the magnetotail current sheet ions has been carried out with self-consistent hybrid simulations (e.g.,[33, 34, 49, 61]). In Refs. [46, 53] the authors have shown that the ion distribution function changes during ion motion from magnetotail lobes to the plasma sheet, with a two-dimensional hybrid simulation, discussing the non-Maxwellian distribution in plasma sheet boundary layer. On the basis of adiabatic and quasi-adiabatic particle motion, the formation of non-Maxwellian distribu-

tions have been presented [49].
Two-dimensional hybrid simulations of magnetotail reconnection have been developed to study ion dynamics [62], or kinematic effects in the reconnection layer [55]; because of the small magnetic field curvature, drifting cold ions move from magnetotail lobes toward the the center of the reconnection region along the so-called Speiser orbits [97], then return to the lobe magnetic lines, showing that the cross-tail current in the thin current sheet is due primarly to ion drift motion.
On the other hand, hybrid simulations about the analysis of charged particle behaviour during thin current sheet formation [35, 36] have shown that most of the current is transported by electrons due to the formation of strong localized electric fields; because of $\mathbf{E} \times \mathbf{B}$ drift, these fields reduce ion current and increase the electron one.

Electron processes have been studied much less intensively than ion processes, although they are implicitely included in full particle models. Hybrid simulation of these processes have been carried out to study collisionless tearing instabilities and magnetic reconnection with electron anisotropy effects [34, 50, 32, 33, 48]; some works have studied the mechanism that mantains the reconnection-region electric field sustaining the nonlinear growth of the collisionless tearing instability in the one dimensional current sheet [32, 33]. The simulation results show that the dominant term in the electric field equation on the magnetic neutral line is proportional to the divergence of the off-diagonal component of the electron pressure tensor and the electron effects substantially alter the growth of the, initially 1D, ion tearing mode.
Additional studies covered nongyrotropic electron effects in the collisionless tearing mode dynamics of 2D current sheets with a small normal magnetic field component [34]; self-consistent structure and dynamics of the dissipative region in the neighborhood of the X-line, which ultimately may form in the magnetotail thin current sheets [50]; the simulation results show that in the neighborhood of the neutral X-line, where the plasma pressure exceeds magnetic pressure, the electric field is primarly determinated by electron quasi-viscosity (the off-diagonal electron pressure terms are retained in the generalized Ohm's law, derived from the electron momentum equation) and to a lesser extent by the electron stream inertia; in the weak magnetic field region the amplitude scale of the 'Speiser' orbits is approximately equal to the half-width of the region where the contribution of the non-gyrotropic component of electric field exceeds the contributions of all other components; electron inertia effects may dominate quasi-viscosity effects only if the characteristic evolution time is comparable to the time for the thermal electron to pass a distance of the order of electron skin length. The main equations of the model studied by [50] do not assign a specific scale for the evolution

of the system. In principle, electron dynamics includes scales that are determinated by electron cyclotron frequencies. However, a detailed study of the system evolution shows that the evolution time scale is dominated by ions, which are responsible for most of the pressure and the inertia. Their large mass allows the ions to break the magnetization condition already on spatial scales comparable with the ion inertia length. The Hall effect leads to a separation of ion and electron dynamics at distances smaller than these scales.
Although the dynamic properties of the system as a whole are determindimension ed by ions, electrons produce the dissipation necessary for breaking the frozen-in condition of the electron stream.

1.5 Plan of Thesis

In Chapter 2 we begin with the fundamental aspects of the hybrid method used in this work and lay out the basic underlying assumptions and equations of the model.

In Chapter 3 the details of a three-dimensional hybrid algorithm as well as the numerical methods used in the analysis are presented. The topics include a discussion of alternative methods to solve the electromagnetic field equations in the massless electron fluid approximation.

In Chapter 4 we discuss a few simple numerical tests, which are useful in verifying the accuracy of the calculations, that is how sensitive are the results to the numerics.

In Chapter 5 the results of the study of the three-dimensional simulation for a set of parameters close to the observed values in the Earth's magnetotail are presented, together with several numerical iterations which show the convergence of the numerical method.

In Chapter 6 the most interesting effects anticipated in the previous chapter are identified and their dependence on the simulation parameters are discussed.

Finally, in Chapter 7, a summary of the relevant conclusions is made; some final remarks are made and future developments are suggested.

Chapter 2

The Hybrid Model

One and two dimensional electromagnetic hybrid codes (fluid electron, particle ions) have been used extensively in the past to study a variety of phenomena occurring in the magnetotail structure and have proved to be quite good at reproducing the global configuration, well comparing with in situ observations. On the other hand, plasma dynamics evolve in a more complicated manner and 1D or 2D field geometry is an obvious limitation. It is of fundamental importance to learn the nature of three-dimensional properties of magnetotail because it is the three-dimensional properties that determine how the magnetotail current sheet propagates away from the Sun. This work addresses the development and the use of a stationary 3D hybrid particle code to search for possible equilibrium magnetotail-like configurations.

2.1 Governing Equations

In modeling plasma phenomena one needs to decide how to describe the electric and magnetic field as well as the plasma species, electrons and ions. In our hybrid model these are electromagnetic fields, massless fluid electrons, and kinetic ions. Specifically, the following equations are used.

(A) Maxwell's equations in the low frequency approximation, which implies the displacement current is neglected in Ampere's law (2.1), supplemented by Faraday's law (2.2), and two field divergence equations (2.3,2.4):

$$\nabla \times \mathbf{B} = \frac{4\pi}{c}\mathbf{J} + \frac{1}{c}\frac{\partial \mathbf{E}}{\partial t} \tag{2.1}$$

$$\nabla \times \mathbf{E} = -\frac{1}{c}\frac{\partial \mathbf{B}}{\partial t} \tag{2.2}$$

$$\nabla \cdot \mathbf{B} = 0 \tag{2.3}$$

$$\nabla \cdot \mathbf{E} = -4\pi q_e(n_e - n_i) \tag{2.4}$$

where $\mathbf{J}$ is the total current density, q_e is the electron charge, and n_e with n_i are the *densities* of electrons and singly charged ions, respectively.

(B) Fluid equations for the electrons including finite electron temperature (T_e); the continuity (2.5) and electron momentum (2.6) equations:

$$\frac{\partial n_e}{\partial t} + \nabla \cdot (n_e \mathbf{v}_e) = 0 \tag{2.5}$$

$$m_e n_e \left(\frac{\partial n_e}{\partial t} + \mathbf{v}_e \cdot \nabla \right) \mathbf{v}_e = -\nabla \cdot \mathbf{P}_e + n_e q_e \left(\mathbf{E} + \frac{\mathbf{v}_e \times \mathbf{B}}{c} \right) + \mathbf{R}_e \tag{2.6}$$

The last term in (2.6) represents the effect of the collisional drag between the electrons and ions.
The momentum flux is closely related to a generalized definition of pressure, in the case where pressure is viewed as a tensor quantity, the 'pressure tensor'. This pressure tensor $\mathbf{P}_e$ is defined in index form by

$$P_{ij} = m\, n(\langle v_i v_j \rangle - u_i u_j)$$

where we have used the components of mean velocity $\mathbf{u}$ and where the angle brakets denote an ensamble average. For the special case of a Maxwellian distribution $P_{ij} = 0$ for $i \neq j$, and $P_{ij} = nT$ for $i = j$; then, in the case where the plasma is nearly Maxwellian (or at least nearly isotropic), $\nabla \cdot \mathbf{P}_e$ can be replaced by the gradient of a scalar pressure, ∇p_e. Even in the very simplest cases where the pressure tensor is isotropic, to provide a complete set of equations, some kind of 'equation of state' must be added to describe how the plasma pressure p changes as a function of the other moments. To avoid dealing with the heat-flux tensor explicitly, we will approximate heat flow by introducing a thermodinamic equation of state for the plasma. This is an equation of the form

$$p = C n_e^{\gamma} \tag{2.7}$$

which relates the scalar pressure p to the density n. The quantity γ expresses how much the temperature of plasma increses as it is compressed,

since $pV^\gamma = constant$, where V is the plasma volume. As such, the equation of state constitutes a simple (and therefore only approximate) statement about the heat flow.
For the case of compression that is slow compared to thermal conduction, we have $\gamma = 1$, i.e. *isothermal* compression. The pressure goes up only because the density goes up. In many cases, bacause particles can freely stream along magnetic field $\mathbf{B}$, conduction parallel to $\mathbf{B}$ provides an avenue for the plasma to remain isothermal, if the compression is, for example, periodic or wave-like along $\mathbf{B}$.
On the other hand, if the compression is fast enough to be *adiabatic* (faster then heat conduction), but slow enough that energy is collisionally exchanged between the three degree of freedom, then $\gamma = 5/3$. Later, we will see that a plasma can support a number of different types of waves, some of which compress the plasma isothermally, while others compress it adiabatically, but this has a no significant effect on the large scale dynamics.

(C) Kinetic treatment of the ions so that for individual particles, the non-relativistic equations of motion can be written:

$$m_i \frac{d\mathbf{v}_i}{dt} = q_i \left(\mathbf{E} + \frac{\mathbf{v}_i \times \mathbf{B}}{c} \right) \tag{2.8}$$

$$\frac{d\mathbf{r}_i}{dt} = \mathbf{v}_i \tag{2.9}$$

Here m_i is the mass of the ion, $\mathbf{v}_i$ its velocity, q_i its charge and $\mathbf{r}_i$ is the location of the ion.

2.2 Ions: Test Particle Simulation

As already explained in the Introduction, we are searching for stationary solutions ($\partial/\partial t = 0$) of magnetotail configurations, in which ions are treated as particles.
At a first step, we assign time-independent magnetic and electric fields, say B_0 and $\mathbf{E}_0$ respectively. Ions move in these fields in accordance with the equations of motion (2.8, 2.9). From the solution of equation (2.8), we cal-

culate the ion moments, namely ion density n_i, ion current density $\mathbf{J}_i$, ion temperature T_i and so on.

2.3 Electrons: Fluid Description

In contrast to ions, electrons are assumed to be a fluid. The electron momentum equation, which represents the first moment of the Vlasov equation for the electrons and the continuity equation have the form of equations (2.5)-(2.6), without any approximations. We now go on the make a few approximations in order to specialize equations (2.5)-(2.6) to the conditions appropriate tp the Earth's magnetotail.

2.3.1 Approximations to Electron Equations: our Hypotheses

-The magnetotail plasma sheet is characterized by a particle density in the range of 1-10 cm^{-3} and a temperature of about 1-10 keV; the density is low enough and the temperature is high enough, that the collisions can be neglected, because the plasma time scales of interest are shorter than the particle collision times τ_{ei}; this suggests that the last term in equation (2.6) is negligible:

$$\mathbf{R}_e = \frac{n_e m_e(\mathbf{v}_e - \mathbf{v}_i)}{(m_e/m_i)\tau_{ei}} \rightarrow 0$$

-In order to eliminate kinetic electron effects, the electrons are treated as an inertia-less fluid ($m_e \rightarrow 0$). This will be valid for phenomena that are sufficiently slow that electrons have time to reach dynamical equilibrium in regard to their motion along the magnetic field.

-We substitute the full electron pressure tensor by the scalar pressure p_e, which we calculate using the isothermal equation of state

$$p_e = n_e k_B T_e \,; \tag{2.10}$$

this hypothesis is justified by experimental observations that show that no substantial global gradients in electron temperature occur in the magnetotail [72]. Moreover, we made runs with the adiabatic approximation and we did not find any substantial difference between the cases.

-Ignoring effects on the electron Debye length scale implies that the plasma is quasi-neutral, so that the electron and ion charge densities are equal.

$$n_e \approx n_i = n$$

The density of particles is low enough that the characteristic plasma frequencies will not be small compared with the the collision frequency, so that damping of the plasma perturbations will occur very slowly; this condition excludes the electron plasma oscillation;

-Finally, in accordance with the steady state limit, $\partial/\partial t = 0$.
The motivation behind this approach is the realization that over a single time step the particle equations and the corresponding moment or fluid equations do not differ very much. One can then use an impicit set of equations to estimate the fields at the next iteration step. In the implicit scheme the solution of the new quantities involves knowledge of these quantities at the new iteration. The particles are then advanced using these new fields and the equations are reinitialized at each iteration step using the new particle information. The plasma is simulating as a collection of particles immersed in and evolving with an electromagnetic field that they self-consistently produce. The time evolution of the model is achieved through the repeatition of this iteration procedure until the desired convergent solution is reached.

With the general assumptions described above, the equations (2.1-2.6) reduce to:

$$\nabla \times \mathbf{B} = \frac{4\pi}{c}\mathbf{J} \tag{2.11}$$

$$\nabla \times \mathbf{E} = 0 \tag{2.12}$$

$$\nabla \cdot \mathbf{B} = 0 \tag{2.13}$$

$$\nabla \cdot \mathbf{E} = 0 \tag{2.14}$$

$$\nabla \cdot (n\mathbf{v}_e) = 0 \tag{2.15}$$

$$\mathbf{E} = \frac{\mathbf{v}_e \times \mathbf{B}}{c} - \frac{\nabla p_e}{n q_e} \tag{2.16}$$

2.3.2 Electron Perpendicular and Parallel Velocity

The electrons are treated using an isothermal equation of state and the quasi-neutrality approximation, thus where the electron density is needed, one uses $n_e \approx n_i$=n, which is found from moving the ions.
The momentum equation (2.16) can be solved for perpendicular electron bulk velocity, by taking its cross product with $\mathbf{B}_0$, being $\mathbf{B}_0$ and $\mathbf{E}_0$ the initial ambient magnetic and electric field, respectively:

$$0 = \mathbf{E}_0 \times \mathbf{B}_0 + \left(\frac{\mathbf{v}_e \times \mathbf{B}_0}{c}\right) \times \mathbf{B}_0 - \frac{\nabla p_e}{n q_e} \times \mathbf{B}_0 \tag{2.17}$$

The cross product (hereafter we'll omit the index 0) of $(\mathbf{v}_e \times \mathbf{B})$ and $\mathbf{B}$ is easily obtained as

$$(\mathbf{v}_e \times \mathbf{B}) \times \mathbf{B} = -B^2 \mathbf{v}_e - \mathbf{B}(\mathbf{B} \cdot \mathbf{v}_e)$$

with $(\mathbf{B} \cdot \mathbf{v}_e) = v_{e\|} B$. This gives

$$0 = \mathbf{E} \times \mathbf{B} - \frac{B^2 \mathbf{v}_e}{c} + \frac{\mathbf{B}}{c}(v_{e\|} B) - \frac{\nabla p_e \times \mathbf{B}}{n q_e} \tag{2.18}$$

Then equation (2.18) can be solved for $\mathbf{v}_e$:

$$\mathbf{v}_e = \frac{c(\mathbf{E} \times \mathbf{B})}{B^2} + v_{e\|} \frac{\mathbf{B}}{B} - \frac{(\nabla p_e \times \mathbf{B})c}{n q_e B^2} \tag{2.19}$$

where $\mathbf{B}/B = \hat{b}$ gives parallel electron velocity direction along magnetic field, yielding an equation for the perpendicular component of the electron bulk velocity:

$$\mathbf{v}_{e\perp} = \frac{c(\mathbf{E} \times \mathbf{B})}{B^2} - \frac{(\nabla p_e \times \mathbf{B})c}{n q_e B^2} \tag{2.20}$$

In order to obtain the parallel electron bulk velocity $v_{e\|}$, we use the electron continuity equation (2.15). By splitting velocity components into the parallel and perpendicular part:

$$\begin{aligned} v_{ex} &= (v_{e\|} + v_{e\perp})_x \\ v_{ey} &= (v_{e\|} + v_{e\perp})_y \\ v_{ez} &= (v_{e\|} + v_{e\perp})_z \end{aligned}$$

we can write the continuity equation (2.15) in the form:

$$\nabla \cdot (n v_{e\|} \hat{b}) = -\nabla \cdot (n \mathbf{v}_{e\perp}) \tag{2.21}$$

or in the Cartesian coordinates:

$$\frac{\partial}{\partial x}(nv_{e\|x}) + \frac{\partial}{\partial y}(nv_{e\|y}) + \frac{\partial}{\partial z}(nv_{e\|z}) = \Phi \tag{2.22}$$

where the function Φ is given by:

$$\Phi = -\sum_{i=1}^{3} \frac{\partial}{\partial x_i}\Big(nv_{e\perp i}\Big)$$

Rearranging the equation (2.22):

$$\frac{nv_{e\|}}{B}(\nabla \cdot \mathbf{B}) + (\mathbf{B} \cdot \nabla)\frac{nv_{e\|}}{B} = \Phi \tag{2.23}$$

Since the divergence of magnetic field is zero, see equation (2.13), the first term of (2.23) no longer appears in the equation, hence the resulting equation to solve is:

$$(\mathbf{B} \cdot \nabla)\frac{nv_{e\|}}{B} = \Phi\,. \tag{2.24}$$

The advantage of this method is that $\mathbf{v}_{e\perp}$ is obtained in a relatively simple and almost noise free way from equation (2.20), while the density, obtained from the ion test particle simulation, has a very low statistical noise, since number density is the zero order moment of the ion distribution function. Therefore, this tecnique promises for good numerical stability and rapid convergence of the iterative procedure (see later).

2.4 Self-consistent Magnetic Field

At this point the electron current density is obtained from the electron velocity as $\mathbf{J}_e = (nq_e\mathbf{v}_e) = nq_e(\mathbf{v}_{e\perp} + \mathbf{v}_{e\|})$. Once we have the total current $\mathbf{J} = \mathbf{J}_i + \mathbf{J}_e$, the new magnetic field is obtained from the Ampere's law equation (2.11):

$$\nabla \times \mathbf{B}^{new} = \frac{4\pi}{c}\mathbf{J} \tag{2.25}$$

The right-side of equation (2.25) contains the ion contribution which is obtained directly, along with the density, from moving the ions and collecting the moments, and the electron one which is obtained from the fluid equations. We make the hypothesis that the new magnetic field is the sum of the input magnetic field $\mathbf{B}_0$ plus a correction $\mathbf{b}$ as

$$\mathbf{B}^{new} = \mathbf{B}_0 + \mathbf{b}.$$

We assume that $\mathbf{b}$ is periodic along x, y and z directions and we impose parity rules for its components. In particular, the x component has to have even parity respect to the z plane, while the y and the z components have to have odd parity.
The equation (2.25) becomes an equation for the correction $\mathbf{b}$ as:

$$\nabla \times \mathbf{b} = \nabla \times \mathbf{B}^{new} - \frac{4\pi}{c}\mathbf{J}_0 = \frac{4\pi}{c}(\mathbf{J} - \mathbf{J}_0) \tag{2.26}$$

being $\mathbf{J}_0 = c/4\pi\nabla \times \mathbf{B}_0$ and $\mathbf{J}$ the input and the calculated total current densities, respectively.
With the position $\mathbf{b} = \nabla \times \mathbf{a}$, where $\mathbf{a}$ is the reduced-potential vector (*i.e.*, restricted to $\mathbf{b}$), the resulting equation is

$$\nabla^2\mathbf{a} = -\frac{4\pi}{c}(\mathbf{J} - \mathbf{J}_0) \tag{2.27}$$

The solution of this equation gives the vector potential over the space, which can then be used to calculate the correction $\mathbf{b}$ and then, the new magnetic field.

2.5 Electrostatic Potential and Electric Field

As for the magnetic field, we assume thet the new electric field is the sum of the input electric field $\mathbf{E}_0$, plus a correction $\mathbf{e}$

$$\mathbf{E}^{new} = \mathbf{E}_0 + \mathbf{e}$$

Since we consider an irrotational electric field, $\nabla \times \mathbf{E} = 0$, we can write it as the gradient of some scalar field, because the curl of a gradient is authomatically zero. This is clearly a useful thing to do since it enables us to replace a vector field by a much simpler scalar field:

$$\mathbf{e} = -\nabla\varphi \tag{2.28}$$

The quantity φ in the above equation is the well-known electric scalar potential. The dot product between equation (2.16) and the input magnetic field $\mathbf{B}$ provides:

$$nq_eE_\parallel = \nabla_\parallel p \tag{2.29}$$

from which we can obtain the relation for the variation of the density along a field line in equilibrium (Boltzmann equilibrium). If we combine equation (2.28) and equation (2.29), remembering the isothermal assumption, we obtain:

$$nq_e\nabla_\parallel\varphi + k_BT_e\nabla_\parallel n = 0 \tag{2.30}$$

or equivalently

$$\ln n + \frac{q_e \varphi(s)}{k_B T_e} = constant \ , \tag{2.31}$$

which determines the variation of the electric potential φ along s, the curvilinear coordinate along the magnetic field. When this electric field has been created, the electrons are in force balance. Provided the scale-length of the density hump is much larger than the Debye length, charge-neutrality will be maintained by n_e remaining almost equal to n_i. Unless the electrons are highly collisional, rapid parallel thermal conduction assures a flat electron temperature along the field line, i.e. $\nabla_\parallel T_e \approx 0$. Then with equation (2.10) and the quasi-neutrality assumption, equation (2.31) becomes

$$\varphi(s) = \varphi_0 + \frac{k_B T_e}{e} \ln \frac{n(s)}{n_0} \tag{2.32}$$

where φ_0 is the electrostatic potential associated with the input electric field and n_0 the density on the boundaries of the configuration or simulation box. The result of equation (2.32) is the knowledge of the electrostatic potential in each grid point. The electric field correction will be given by $e_x = -\partial\varphi/\partial x$, $e_y = -\partial\varphi/\partial y$, $e_z = -\partial\varphi/\partial z$.

Obviously, both electrons and ions cannot simultaneously be in Boltzmann equilibrium in the presence of an electric potential that varies along the field lines, or else charge neutrality would be violated in the absence of some externally introduced charge. The only charge-neutral equilibrium under normal circumstances is one in which the electric potential and ion and electron densities are costant along the field lines. However, if a density variation, say a density 'hump', is created dynamically along a field line in a charge-neutral plasma, electron and ion flow velocities parallel to the magnetic field will arise. The larger mass of the ions results in them responding relatively slowly to the presence of the 'hump' in n along a field line. Meanwhile, the lighter electrons respond much more quickly and set up a Boltzmann distribution in the presence of the density hump. Then, the electrons come to equilibrium on a time-scale much faster than the ions.

Chapter 3

3D Simulation Code

In the previous Chapter we have given the basic equations and the approximations of the model. Their numerical implementation is the next task to be discussed.

3.1 Dimensionless Variables

From B_0 and E_0, the static ambient fields, we can define the inverse ion gyrofrequency $\omega_{0i}^{-1} = m_i c/q_i B_0$ as the time unit and the drift velocity $V_E = cE_0/B_0$ as the velocity unit. With these units the spatial scales are in terms of $l = V_E/\omega_{0i}$.
In order to model the geomagnetic tail, we fix $L = 10^4$ km, $E_0 = 0.1$ mV/m and $B_0 = 10$ nT [25], so that the drift velocity $V_E = cE_0/B_0$ is equal to 10 km/s. We summarized the normalization and the typical values of the physical quantities in the code in Table 1.

Table 1. Normalization Used in the Model

Physical quantities	normalization	Typical values
Time	ω_{0i}^{-1}	1 s
Electric field	E_0	0.1 mV/m
Magnetic field	B_0	10 nT
Current density	$cB_0/4\pi L$	0.8 nA/m^2
Velocity	$V_E = cE_0/B_0$	10 km/s
Temperature	$\mathrm{T}_0 = m_i {V^2}_E/k_B$	1.2×10 K
Ion density	$\mathrm{n}_0 = cB_0/4\pi e L V_E$	0.5 cm^{-3}
Pressure	$\mathrm{p}_0 = \mathrm{n}_0 k_B T_0$	8.4×10^{-5} nPa

With this choice there are no costants (4π, c, etc.) in electron equations and in (2.8) for ion motion, while ion velocity (2.9) and momentum (2.16) equations are expressed in terms of a constant parameter χ, which value comes from normalization parameters in Table 1:

$$\chi = \frac{\omega_{0i}^{-1} L}{V_E} = 10^3$$

In part this choice of normalization represents well-estabilished and convenient-sized units. One could instead normalize lengths to the unit length L and time to the inverse ion gyrofrequency ω_{0i}. The other variables are normalized using L and ω_{0i} with magnetic field background value B_0. The table below lists these normalization units (Table 2):

Table 2.

Physical quantities	normalization	Typical values
Length	L	10^4 km
Time	ω_{0i}^{-1}	1 s
Electric field	$E_0 = (B_0 \omega_{0i} L \zeta)/c$	0.1mV/m
Magnetic field	B_0	10 nT
Current density	$cB_0/4\pi L$	0.8 nA/m^2
Velocity	$V_E = cE_0/B_0$	10 km/s
Temperature	$\mathrm{T}_0 = m_i {V^2}_E/k_B$	1.2×10 K
Ion density	n_0=1/L^3	0.5 cm^{-3}
Pressure	p_0 =$\mathrm{n}_0 k_B T_0$	8.4×10 nPa

In these units, the free value electric field in ion motion (2.8), electron perpendicular velocity (2.20) and electric field potential (2.32) equations, is expressed as ζE, where ζ-factor is defined by

$$\zeta = \frac{cE_0}{B_0 \omega_{0i}} L = 3 \times 10^5$$

according to typical values of physical quantities in Table 2.
We carry out our simulation runs with normalization parameters which are shown in Table 1.

3.1.1 Spatial Grid

We consider a rectangular simulation box, with dimension coordinates x, y, z such that:

$$-0.5L \leq x \leq 0.5L$$
$$-2.5L \leq y \leq 2.5L$$
$$0 \leq z \leq 5L$$

where L is the total length along x-direction, as already explained.
The spatial domain is subdivided into N_x, N_y, N_z computational cells of equal length, $\Delta x = L_x/N_x$, $\Delta y = L_y/N_y$, $\Delta z = L_z/N_z$, respectively. From a physical point of view, we choose the cell size $(1/64L)$ in order to resolve the ion Larmor scales and the physical processes which occur on these scales. The number of cells in each direction is chosen equal to $2^6 = 64$. $N_x = N_y = N_z$=64, is a reasonable number that yields a total number of grid points $2^{18} = 262144$. This requires, at least, a number of $\sim 10^7$ particles. With this number the statistical error on the ion moments is of the order of 2% (see later).
The spatial grid is made up of $64 \times 64 \times 64$ mesh points, that define the centers of the N_x, N_y, N_z cells in the physical domain. All source terms (densities and currents), electromagnetic field components and scalar potential are specified at the mesh points, *i.e.*, the cell centers.

3.2 Simulation Algorithms

At this point, the general scheme of hybrid calculations can be described as follows [22]:

1. the dynamics of the ion component is simulated by the particle method and the macroscopic ion characteristics are determinated (as the moments of the ion distribution function) on the above spatial grid;

2. the electron parallel and perpendicular bulk velocity equations are solved to compute the electron current density;

3. the magnetic field is determined from Ampere equation;

4. the electric field is determinated from Faraday equation.

5. repeat all steps in the new fields in order to obtain the convergence of the iterative process.

We discuss the numerical implementation of our hybrid model, describing the methods used to solve each equation in turn.

3.2.1 Ion Dynamics

To introduce the discussion of the 'mechanics' of the hybrid code, we turn to how to get started: the initialization. We need to load the particles to initialize the fields. After all the particles are loaded, we can 'move' them to collect the moments and solve the field equation at first iteration.

Initialization: Ion Injection Scheme

Following [25], we set up an injection scheme corresponding to the inflow in the plasma sheet from the lobes of the magnetotail, that is particles entering from the planes at $x = \pm 0.5L$, with a distribution corresponding, in velocity space, to the flux of a shifted Maxwellian [8]:

$$f(v_{\parallel}, v_{\perp}) = (\sqrt{2\pi} v_{th}^3)^{-1} exp\left(- \frac{(v_{\parallel} - u)^2 + {v_{\perp}}^2}{2 v_{th}^2} \right) \tag{3.1}$$

here $v_{th} = \sqrt{k_B T/m}$ is the thermal velocity and u is the streaming velocity. The values of z and y are choosen at random on the planes $x = \pm 0.5L$. Since the particles are entering the simulation box by moving along x, this yields $F(v_x, v_y, v_z) \propto v_x f(v_{\parallel}, v_{\perp})$. We express $v_{\parallel}$ and $v_{\perp}$ through v_x, v_y and v_z to have

$$v_{\parallel} = \frac{\mathbf{v} \cdot \mathbf{B}}{|\mathbf{B}|} = \frac{v_x B_x + v_y B_y + v_z B_z}{\sqrt{B_x^2 + B_y^2 + B_z^2}} \tag{3.2}$$

$$v_{\perp} = v^2 - v_{\parallel}^2 = v_x^2 + v_y^2 + v_z^2 - v_{\parallel}^2 \tag{3.3}$$

The unperturbed magnetic field components at $x = \pm 0.5L$ surface are equal to $B_x = B_n$, $B_y = 0$, $|B_z| = B_0$. We introduce the components of the unit vector along $\mathbf{B}$ at $x = \pm 0.5L$,

$$\hat{b}_x = \frac{B_n}{\sqrt{B_n^2 + B_0^2}} \tag{3.4}$$

$$\hat{b}_z = \frac{B_0}{\sqrt{B_n^2 + B_0^2}} \tag{3.5}$$

Inserting these expressions into equation (3.1), we finally come to the equation that has to be solved for the variables v_x, v_y and v_z, distributed according to a shifted Maxwellian:

$$\frac{\exp(-u^2/2v_{th}^2)}{(\sqrt{2\pi}v_{th}^3)}\exp\left(-\frac{v_z^2-2u\hat{b}_z v_z}{2v_{th}^2}\right)\exp\left(-\frac{v_y^2}{2v_{th}^2}\right)$$

$$v_x\exp\left(-\frac{v_x^2-2u\hat{b}_x v_x}{2v_{th}^2}\right)dv_x dv_y dv_z = Cd\xi d\eta d\zeta \tag{3.6}$$

where ξ, η ζ are random numbers evenly distributed in the interval [0,1], and C is a constant calculated from the condition specified below. The coefficient $\sqrt{2\pi}v_{th}^3)^{-1}\exp(-u^2/v_{th}^2)$ depends only on the constant parameters u and v_{th} and hereinafter cam be included in the constant C. We will also assume for this discussion, that all velocities are normalized to the thermal velocity v_{th}, and drop v_{th} in what follows. As it is clear from the equation (3.6), the dependence on each of the velocity components is factorized, and we can solve independently three different equations, namely:

$$v_x\exp\left[-\left(v_x^2-2u\hat{b}_x v_x\right)/2\right]dv_x = C_\xi d\xi \tag{3.7}$$

$$\exp\left[-v_y^2/2\right]dv_y = C_\eta d\eta \tag{3.8}$$

$$\exp\left[-\left(v_z^2-2u\hat{b}_z v_z\right)/2\right]dv_z = C_\zeta d\zeta \tag{3.9}$$

Clearly, v_y is distributed according to a Maxwellian and we can use the Central Limit Theorem for v_y [106].
For v_x and v_z we have to take into account the assymetry introduced by the streaming velocity u. Assuming that ζ varies in the interval $0<\zeta<1$ with the uniform probability, and integrating the equation (3.9) from $-\infty$ to v_z on the l.h.s. and from 0 to ζ on the r.h.s., we can easily obtain the equation to be solved for v_z:

$$1+\mathrm{erf}\left[\left(\mathrm{v_z}-\mathrm{u\hat{b}_z}\right)/\sqrt{2}\right] = \mathrm{C}_\zeta\zeta \tag{3.10}$$

where the coefficient $(\sqrt{\pi}/2)\exp(u^2\hat{b}_x^2/2)$ can again be assumed to be included in C_ζ, and erf(z) is the well-known Error function:

$$\mathrm{erf(z)} = (2/\sqrt{\pi})\int_0^{\mathrm{z}}\exp(-\mathrm{t}^2)\mathrm{dt}$$

It is evident that for $\zeta = 0$, $v_z = -\infty$ ($\mathrm{erf}(-\infty) = -1$). The coefficient C_ζ is fixed by the condition that for $\zeta = 1$, v_z is equal to $+\infty$. Thus for C_ζ we obtain from the equation (3.10): $C_\zeta = 1 + \mathrm{erf}(+\infty) = 2$. Finally, to get the distribution of v_z corresponding to function given by equation (3.9) we have to solve for each random number ζ ($0 < \zeta < 1$) the equation:

$$1 + \mathrm{erf}\left[\left(\mathrm{v_z} - \mathrm{u}\hat{\mathrm{b}}_\mathrm{z}\right)/\sqrt{2}\right] = 2\zeta$$

The integral in the equation (3.9) for v_z is positively defined over all the interval of integration. This is not the case of v_x component (see equation (3.7)), where we have to consider separately positive and negative v_x for particles entering into the current sheet from the lower ($x = -0.5L$) and upper ($x = 0.5L$) boundaries, respectively, of the simulation box. Integrating the equation (3.9) for $x > 0$ in the interval $-\infty < v_x < 0$ we obtain:

$$I^-(v_x, u) = -\exp\left[\left(v_x^2 - u^2\hat{b}_x^2\right)/2\right] + \alpha\mathrm{erf}\left[\left(\mathrm{v_x} - \mathrm{u}\hat{\mathrm{b}}_\mathrm{x}\right)\sqrt{2}\right] \qquad (3.11)$$

where $\alpha \equiv \sqrt{\pi/2}u\hat{b}_x \exp(u^2\hat{b}_x^2/2)$. For $v_x = 0$ we will have

$$I^-(0, u) = -1 + \alpha(1 - \Phi) \equiv C^{-1}$$

where $\Phi \equiv \mathrm{erf}(\mathrm{u}\hat{\mathrm{b}}_\mathrm{x}/\sqrt{2})$. Here we have used the asymmetric propery of the error function, $\mathrm{erf}(-\mathrm{z}) = -\mathrm{erf}(\mathrm{z})$. C^{-1} defines the weight of negative velocities v_x in the distribution. Now, integrating equation for v_x in the equation (3.7) for $x < 0$, in the interval $0 < v_x < \infty$, it is easy to show that the corresponding integral on the left side is equal to $I^+(v_x, u) = -I^-(-v_x, -u)$. Introducing the coefficient C^+ as the weight of positive v_x in the distribution, we will obtain

$$C^+ \equiv I^+(0, u) = 1 + \alpha(1 + \Phi) \qquad (3.12)$$

Now, the interval $[0, 1]$ for the random number ξ has to be divided, according to the corresponding weights, in two intervals: $0 < \xi < \xi_1$ for negative v_x and $\xi_1 < \xi < 1$ for positive v_x, where ξ_1 is equal to

$$\xi_1 = \frac{|C^-|}{|C^+| + |C^-|} = \frac{1 - \alpha(1 - \Phi)}{2(1 + \alpha\Phi)} \qquad (3.13)$$

Here we have used the fact that C^- is negative and C^+ is positive for any positive u. Integrating now equation (3.7) for the proper intervals, we will have for negative and positive v_x the following relations, respectively,

$I^-(v_x,u) = C_\xi^- \xi$ and $I^+(v_x,u) = C_\xi^+(1-\xi)$, where the coefficients C_ξ^- and C_ξ^+ have to satisfy the following conditions

$$C_\xi^- \xi_1 = I^-(0,u) \equiv C^-, \quad C_\xi^+(1-\xi_1) = I^+(0,u) \equiv C^+ \tag{3.14}$$

From this system of equations and the expressions for C^- and C^+, given by the equations (3.12) and (3.13) we will obtain for the coefficients C_ξ^- and C_ξ^+:

$$C_\xi^- = -2(1+\alpha\Phi), \quad C_\xi^+ = 2(1+\alpha\Phi) \tag{3.15}$$

solving equations (3.14) and (3.15) for each random number ξ in the corresponding interval we will obtain the required particle distribution.

Calculation of Ion Distribution Function Moments

In the numerical simulation, we follow the particles and record the positions $\mathbf{r}_i(t)$ and velocities $\mathbf{v}_i(t)$ when they pass from one cell of size Δy to the next along the y direction [106]. 'Virtual detectors' are perpendicular to the y direction because the main current is along y. Following [45], for an ensemble of M particles the fine-grained distribution function can be represented as

$$f(\mathbf{r},\mathbf{v},t) = \sum_{i=1}^{M} \delta[\mathbf{r} - \mathbf{r}_i(t)]\delta[\mathbf{v} - \mathbf{v}_i(t)] \tag{3.16}$$

The fine-grained particle density $n(\mathbf{r},t)$ is

$$n(\mathbf{r},t) = \int f(\mathbf{r},\mathbf{v},t)d^3v = \sum_{i=1}^{M} \delta[x - x_i(t)]\delta[y - y_i(t)]\delta[z - z_i(t)] \tag{3.17}$$

Now we want to obtain a coarse-grained particle density by considering those particles that cross the planes at $y = y_m$ considered above in a window of amplitude $\Delta x \Delta z$ around x_l and z_n. Assuming that the flow of particles is stationary we can average over Δx and Δz and over a very long time period Δt to obtain

$$n(x_l,y_m,z_n) = \frac{1}{\Delta t \Delta x \Delta z} \times \int_{-\Delta t/2}^{\Delta t/2} dt \int_{x_l+\Delta x/2}^{x_l-\Delta t/2} dx \int_{z_n+\Delta z/2}^{z_n-\Delta t/2} dz\, n(x,y,z,t) =$$

$$\frac{1}{\Delta t \Delta x \Delta z} \int_{-\Delta t/2}^{\Delta t/2} dt \sum_{i=1}^{M'} \delta[y_m - y^i(t)] \tag{3.18}$$

where M' represents the number of particles which at any time pass through $[x_l - \Delta x/2, x_l + \Delta x/2]$ and $[z_n - \Delta z/2, z_n + \Delta z/2]$. The change of integration variable inside the δ function gives

$$\delta[y_m - y^i(t)] = \sum_k \frac{\delta[t - {t_k}^i(y_m)]}{|dy^i/dt|} = \sum_k \frac{\delta[t - {t_k}^i(y_m)]}{|v^i_{y,k}(y_m)|} \tag{3.19}$$

where the sum over k denotes the multiple zeros of $y_m - y^i(t)$ and $v^i_{y,k}(y_m)$ indicates the velocity at the time ${t_k}^i(y_m)$ of the k-th crossing of the window $\Delta x \Delta z$ at $y = y_m$ by the i-th particle. Thus, the coarse grained density is obtained numerically on a three-dimensional grid as [106]

$$n(x_l, y_m, z_n) = \frac{1}{\Delta t \Delta x \Delta z} \sum_{i,k} \frac{1}{|v^i_{y,k}(y_m)|} \tag{3.20}$$

(in the following, we shall omit the index k). In the numerical computation, every time that a particle crosses the detector grids at y_m the contribution to n and to the other moments is taken into account. In the above expression there is a free parameter, Δt, which is fixed by specifying the density in a particular point. This may corresponds to the density required to have the right amount of total electric current. Moreover, Δt is taken long enough for ions to evolve in the plasma sheet and exit from the magnetic field model. The other moments of the distribution function, namely bulk velocity $\mathbf{V}(\mathbf{r}, t)$, pressure tensor P, including the off diagonal components P_{ij} and the heat flux $\mathbf{Q}(\mathbf{r}, t)$, are defined as

$$n\mathbf{V} = \int \mathbf{v} f d^3v \tag{3.21}$$

$$P_{ij} = nk_B T_{ij} = m \int (v_i - V_i)(v_j - V_j) f d^3v \tag{3.22}$$

$$\mathbf{Q} = \frac{m}{2} \int (\mathbf{v} - \mathbf{V})^2 (\mathbf{v} - \mathbf{V}) f d^3v \tag{3.23}$$

and are obtained in a way similar to equation (3.20). We also define the temperature parallel to the local magnetic field as

$$T_\parallel = \frac{m_i}{nk_B} \int (v_\parallel - V_\parallel)^2 f d^3v$$

where $v_\parallel = \mathbf{v} \cdot \mathbf{B}/B$ and the perpendicular temperature as

$$T_\perp = \frac{1}{2}(T_{xx} + T_{yy} + T_{zz} - T_\parallel)$$

3.2.2 Electron Bulk Perpendicular and Parallel Velocity Methods

We solve for $\mathbf{v}_{e\perp}$ (equation (2.20)) by using a 4-th order finite difference scheme to compute the pressure gradient in each mesh point. A Semi-Lagrangian scheme [101, 13] for solving the advection-reaction problem (equation (2.24)) for computing electron bulk parallel velocity is proposed. The

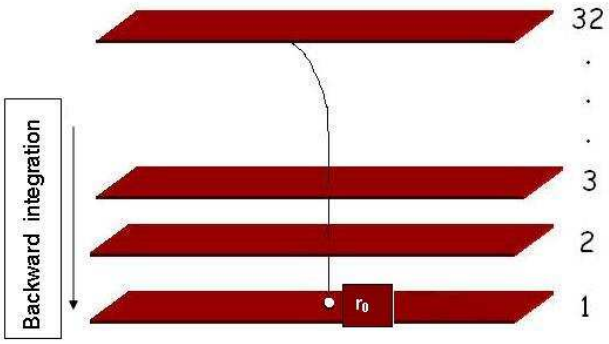

Figure 3.1: We integrate the equations (3.24) and (3.25) from the grid points (x, y, z) on the other planes (2-32) backward to the reference plane-1 (reference point $\mathbf{r}_0$), where the value of f is known.

method of characteristics for *each* point in the regular mesh is applied. This scheme is a combination of elements of the Eulerian and the Lagrangian approach. In an Eulerian advection scheme an observer watches the world evolve around him at a fixed point. Such schemes work well on regular Cartesian meshes, but often lead to overly restrictive iterative steps due to considerations of computational stability. In a Lagrangian advection scheme the observer watches the world evolve around him as he travels with a fluid particle. Such schemes can often use much larger iterative steps than Eulerian ones, but have disadvantages that initially regularly spaced set of particles will generally evolve to a highly irregularly spaced set, and important features of the flow may consequently not be well represented. The idea behind Semi-Lagrangian advection schemes is to try to get the best of both worlds: the regular resolution of Eulerian schemes and the enhanced stability of Lagrangian ones. In this numerical scheme at each "time" step the grid-points of the numerical mesh are representing the arrival points of backward trajectories at the future "time". The point reached during this back-tracking defines where a "particle" was at the beginning of the time-step. Essentially, all variables are then found through interpolation (using values at the previous time-step for the interpolation grid) to this departure point.
Taking into account that $(\mathbf{B}\cdot\nabla)/B$ is equal to $\partial/\partial s$, where s is the curvilinear coordinate along the magnetic field, equation (2.24) becomes

$$\frac{\partial f}{\partial s} = \frac{\Phi}{B}\,, \tag{3.24}$$

where $f = nv_{e\|}/B$. We solve it simultaneously with the magnetic field line equation

$$\frac{d\mathbf{r}}{ds} = -\frac{\mathbf{B}}{B}, \tag{3.25}$$

looking for the value of f at the mesh points. We assume Φ, n and the vector field $\mathbf{B}$ are defined on all grid points in the computational domain. The basic idea of the Semi-Lagrangian scheme is that it solves the equation (3.24) as an ordinary differential equation along the trajectory that connects the reference point $\mathbf{r}_0$ at length s to the point $\mathbf{r}$ at length $s + \Delta s$. In general it can be written as

$$f(s + \Delta s) = f_0(s) + \int_s^{s+\Delta s} \frac{\Phi}{B}(\mathbf{r}(s'))ds' \tag{3.26}$$

Actually, we choose $\mathbf{r}_0$ on a reference plane in the simulation box (which does not belong to the computational mesh in space) where the value of f is known (see *Sec.* 3.3.1) and integrate equations (3.24) and (3.25) from the grid points (x, y, z) on the other planes backward to this plane. Then the equation (3.26) becomes

$$f_0(r_0) = f(x, y, z) + \int_{\mathbf{r}=x,y,z}^{\mathbf{r_0}} \frac{\Phi}{B}(\mathbf{r})d\mathbf{r} \tag{3.27}$$

We use a three-dimensional quadratic interpolation [74] to evaluate Φ and $\mathbf{B}$ along the magnetic field force lines and a 4-th order Runge-Kutta method to calculate the term $\Delta f = \int_{r=x,y,z}^{r_0} \frac{\Phi}{B}(\mathbf{r})d\mathbf{r}$. We stop the integration when the magnetic field line reaches the reference plane and the value of f on the grid point $\mathbf{r}$ is given by $f_0 - \Delta f$.

The use of Semi-Lagrangian techniques are popular in the computer community. The Semi-Lagrangian scheme allows the use of large time-steps without limiting the stability. Therefore, the choice of time-step in the Semi-Lagrangian scheme is only limited by numerical accuracy. However, despite its stability properties severe truncation errors may cause misleading results. In particular, error is introduced through the linear particle trace and the interpolation. The linear trajectories introduce $O(k)$ error and the interpolation introduces $O(h^2)$ error for each length step $k = \Delta s$ (where $h = \Delta x = \Delta y = \Delta z$ is the grid spacing), giving the total error:

$$O(k) + O\left(\frac{h^2}{k}\right)$$

Thus the method is first order accurate if $k \geq Ch$, for some arbitrary constant C [101]. For an excellent introduction, review and details see [99, 98].

Method of Interpolation

Because both the function Φ and the magnetic field $\mathbf{B}$ are interpolated in a technically similar way, we briefly describe the method only for $\mathbf{B}$ interpolation. For a more detailed description see [74].
From any point $\mathbf{r} = (x, y, z)$, we have to determine the components of the magnetic field

$$\mathbf{B}(\mathbf{r}) = \Big(B_x(\mathbf{r}), B_y(\mathbf{r}), B_z(\mathbf{r})\Big)$$

that is $B_k(\mathbf{r})$ with $k = 1, 2, 3$. To realize a quadratic interpolation we have to calculate, for each k-component, ten coefficients, namely α_k^i $(i = 0, 1, 2, 3...9)$ which verify the following relation:

$$B_k(\mathbf{r}) = \alpha_k^1 x^2 + \alpha_k^2 y^2 + \alpha_k^3 z^2 + \alpha_k^4 xy + \alpha_k^5 xz + \alpha_k^6 yz + \alpha_k^7 x + \alpha_k^8 y + \alpha_k^9 z + \alpha_k^0 \,. \tag{3.28}$$

In order to solve this problem and find the ten coefficients for each component k, ten conditions have to be obtained by considering the magnetic field values in the ten points $\mathbf{r}_i$ around $\mathbf{r}$. The first point $(x_0 = x^{(l)}, y_0 = y^{(m)}, z_0 = z^{(n)})$ is the nearest point to $\mathbf{r}$ on the grid, with the index l, m and n in the three directions of the simulation grid. It is obvious to choose in the interpolation the six points around (x_0, y_0, z_0) on the grid, that are

$$(x^{(l\pm1)}, y^{(m)}, z^{(n)})$$

$$(x^{(l)}, y^{(m\pm1)}, z^{(n)})$$

$$(x^{(l)}, y^{(m)}, z^{(n\pm1)})$$

The remaining three points are chosen from the vertexes of the octant in the grid where the point $\mathbf{r}$ lies; this choice gives four points, so there is one point in excess. We eliminate the farthest one: the point $(x^{(ll)}, y^{(mm)}, z^{(nn)})$. For more details see [74].
When the equation (3.28) is written for each of the ten points, three systems of ten equations are obtained for each component. The equation (3.28) can be written in matricial form:

$$B_i^k = M_{ij} A_j^k \tag{3.29}$$

where B_i^k is a column vector formed by the ten values of the k-component of magnetic field $\mathbf{B}$ and A_j^k is another column vector made by the coefficients α_k^j that are the unknown of the system. In the 10×10 matrix M_{ij} (clearly M_{ij} is the same for each k because the ten points of the lattice are the

same for all three components of the magnetic field), each i row contains the values $(x_i^2, y_i^2, z_i^2, x_iy_i, x_iz_i, y_iz_i, x_i, y_i, z_i, 1)$ for each of the ten points chosen for the interpolation. To get the solution we have only to invert the system for each components k. We note that two techniques can speed up the calculation. The matrix M_{ij} does not depend on the component k of the magnetic field $\mathbf{B}$, thus the first step of the inversion, can be realized only once, and then the final part of the inversion has to be done for each of the three components for the triangular matrix M_{ij}. The second improvement is the analytic reduction of the 10×10 system in a 9×9 system, since in the last column of the matrix M_{ij} all the terms are equal to one. This can be done for example by substracting the first equation from all the others, keeping the a 9×9 system, without the coefficients α_k^{10}. In this case all the coefficients α_k^i, except α_k^0, are determinated by inverting the 9×9 system. The last coefficient is determinated by considering any equation of the 10×10 system. In the matricial form, while the first equation corresponds to the nearest point to $\mathbf{r}$, that is $\mathbf{r}_0 = (x_0, y_0, z_0)$, the reduced matrix M'_{ij} (9×9), will therefore contain on each row i the following values:
$(x_i^2 - x_0^2, y_i^2 - y_0^2, z_i^2 - z_0^2, x_iy_i - x_0y_0, x_iz_i - x_0z_0, y_iz_i - y_0z_0, x_i - x_0, y_i - y_0, z_i - z_0)$
for $i = 1, 2, 3, ...9$, corresponding to the other nine points. Having about N^2 operations for the inversion of a $N \times N$ system, it is possible to gain 20% time by reducing the system from 10 to 9 equations. For a further description and deeper insight see [74].

3.2.3 Ampere's Law: 3D FFT Method

In general we have expressed the magnetic field as the sum of a initial magnetic field $\mathbf{B}_0$ and the correction $\mathbf{b}$. Then, the components of the new field are:

$$B_x = B_0^x + b_x \tag{3.30}$$

$$B_y = B_0^y + b_y \tag{3.31}$$

$$B_z = B_0^z + b_z \tag{3.32}$$

We have assumed $\mathbf{b}$ to be periodic along each spatial direction, according to the parity rules we have to respect for these corrections. In particular the x component of the magnetic field corrections has to have even parity respect to the x=0 plane, *i.e*

$$b_x(x, y, z) = b_x(-x, y, z)$$

and the z component of $\mathbf{b}$ has to have odd parity:

$$b_z(x, y, z) = -b_z(-x, y, z)$$

The b_y component has authomatically odd parity from these conditons. Applying the Ampere's law to the correction $\mathbf{b}$, the equation, in dimensionless form, to be solved is (see *Ch.* 2)

$$\nabla^2 \mathbf{a} = (\mathbf{J} - \mathbf{J}_0) \tag{3.33}$$

The solution to this eqaution gives the vector potential over the space, which can then be used to calculate the correction and then the new magnetic field. Poisson's equation can be solved by various methods, including spectral methods (Discrete Fourier Transforms), finite element or finite volume methods. Here we consider a domain with periodic boundary conditions, then our algorithm takes a particularly simple form. The periodicity allows us to evaluate the vector potential components into the Fourier domain: we build a three dimensional FFT algorithm. We are given the current density $(\mathbf{J}-\mathbf{J}_0)$ and want to solve for the potential $\mathbf{a}$. The space has been discretized by breaking it into a uniform mesh. Solving for the potential on this mesh will give us an approximate answer to the continous solution and as long as the mesh is "fine enough" the approximation will be reasonably good. For semplicity, let's start by assuming 1-dimensional space, and let's consider the Discrete Fourier Transform (DFT) of the current density $\mathbf{J}$(x). The DFT is

$$\theta_j = \sum_{x_{-32}<x_l<x_{32}}^{n-1} \mathbf{J}(x) e^{2\pi i x j/n}$$

which transforms our current density function into a set of frequency components (i is the imaginary number $\sqrt{-1}$). Since the Poisson's equation is linear we can solve for each frequency component separately. Lets use the notation $k_j = 2\pi j/n$ and consider the j^{th} frequency component of the current density function : $f_j(x) = \theta_j e^{ik_j x}$. If we plug this component into Poisson's equation, we get

$$\nabla^2 \mathbf{a}_j(x) = -\theta_j e^{ik_j x}$$

The solution to this equation is

$$\mathbf{a}_j(x) = \theta_j \frac{1}{k_j^2} e^{ik_j x} = \frac{1}{k_j^2} f_j(x)$$

since $\nabla^2 e^{ik_j x} = -k_j^2 e^{ik_j x}$. In other words, to solve for j^{th} frequency component of the vector potential $\mathbf{a}$ we simply multiply the j^{th} frequency component of the current density function by $-1/k_j^2$.

We can similarly solve for each of the other frequency components of the vector potential, then add up the solutions to get the solution to our initial problem. This is equivalent to convolving the frequency component j with $1/k_j^2$ and then trasforming back to coordinate space, which can be done with a second FFT. This idea is applied in three dimensions by defining a 1-dimensional FFT on vectors in all dimensions. In this case the solution for a particular component with frequencies k_j,k_i and k_m is

$$\mathbf{a}_{jim}(\mathbf{r}) = \frac{1}{k_j^2 + k_i^2 + k_m^2} f_{jim}(\mathbf{r})$$

where j,i and m are the frequency components in the x, y and z dimensions respectively.
So the overall algorithm in three dimensions follows the following conceptual steps:

1. Break space into discrete uniform mesh points.
2. Determine $\mathbf{J}(\mathbf{r})$ and $\mathbf{J}_0$ for each point.
3. Do a 3D-FFT of $(\mathbf{J} - \mathbf{J}_0)$ on the mesh.
4. Convolve the results with the sum of inverse square frequencies.
5. Calculate the magnetic field $\mathbf{b}$ in the Fourier space as $i\mathbf{k} \times \mathbf{a}$
6. Do an inverse FFT back to the original mesh point.

This will give $\mathbf{a}(\mathbf{r})$ over the mesh from which we can derive the magnetic field components. For N mesh points the algorithm will take $O(N \log N)$ time steps.

3.2.4 Faraday's Law Method: Electric Field

As we have seen in *Sec.* 2.5, unless the electrons are highly collisional, rapid parallel thermal conduction assures a flat electron temperature along the field line, *i.e*, $\nabla_\parallel T_e \approx 0$. Then with $p_e = nk_B T_e$, the equation (2.30) becomes an exact derivative along field line:

$$\frac{\partial \varphi}{\partial s} = -\frac{1}{nq_e}\frac{\partial p_e}{\partial s} \tag{3.34}$$

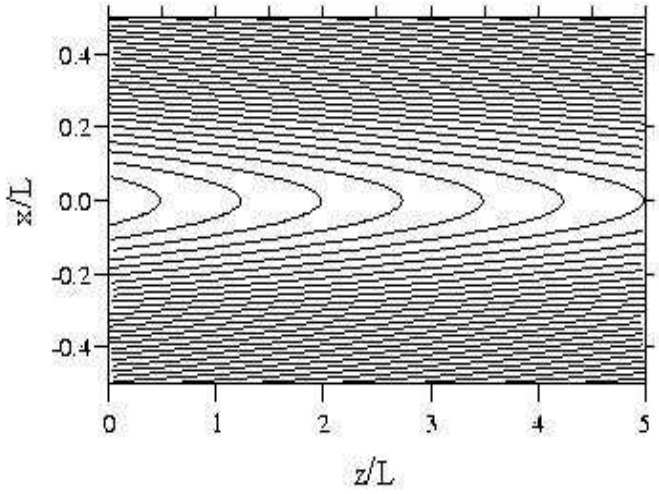

Figure 3.2: Parabolic field line configuration.

which integrates yields

$$\varphi = \varphi_0 - \frac{k_B T_e}{q_e} \ln \frac{n}{n_0} \tag{3.35}$$

The equation (3.35) is the Boltzmann relation used in mirror plasma [100]. It is applied in a new way here to infer how the potential varies from field line to field line. The equation (3.35) is solved with the Semi-Lagrangian scheme earlier described. The result is the knowledge of the electrostatic potential in each grid point. The new electric field components, E_x,E_y and E_z, can be found from equation (3.35) by differentiating with respect to spatial coordinates, with an usual 4-th order finite difference algorithm.

3.3 Initial and Boundary Conditions: Application to the Magnetotail Configuration

We use a coordinate system where the z-axis is defined along the line connecting the center of the Sun to the center of the Earth. The origin is defined

at the center of the Earth, and is positive away from the Sun. The y-axis is along the dawn-dusk direction. The x-axis is defined as the cross product of the y- and z-axes. The magnetic dipole axis lies within the xz plane. In this reference frame, the considered input magnetic field configuration consists of two component: a sign reversing component, directed along the Earth-Sun axis, $\mathbf{B}_{0z}(x) = B_{0z}(x)\mathbf{e}_z$, such that $B_{0z}(x) = -B_{0z}(-x)$ and a constant component normal to the sheet $\mathbf{B}_n = B_n\mathbf{e}_x$; thus, the total magnetic field is given by $\mathbf{B} = \mathbf{B}_{0z}(x) + \mathbf{B}_n$. The reversing field component $B_{0z}(x)$ is negative in the upper (northern) lobe of the tail and positive in the lower lobe. Following [106], we use for $B_{0z}(x)$ the expression of a modified Harris magnetic field reversal, setting it in such a way that the asymptotic value B_0 is reached smoothly at the edges of the simulation box at $x = \pm 0.5L$, where also the derivative of the field with respect to x becomes zero [106]:

$$B_{0z}(x) = -B_0 \frac{\tanh(x/\lambda) - (x/\lambda)\cosh^{-2}(L/2\lambda)}{\tanh(L/2\lambda) - (L/2\lambda)\cosh^{-2}(L/2\lambda)}\,. \tag{3.36}$$

L is the total thickness of the considered magnetic field configuration and $\lambda = 0.25L$ is the current sheet half thickness. This model describes the parabolic field line geometry which is found in the Earth's tail from approximately 10 to 60 R_E (R_E is the Earth's radius) downtail, and is shown for $B_n = 0.1\,B_0$ in Figure (3.2). Since usually $B_n \ll B_0$, this configuration is referred to as quasi-neutral current sheet.
In addition to the above magnetic field configuration, a cross tail electric field $\mathbf{E} = E_y\mathbf{e}_y$ (E_y is constant, say E_0) oriented in the dawn-dusk direction and whose origin lays in the solar wind-magnetosphere coupling, is also included [25].

3.3.1 Boundary Condition for the Parallel Electron Bulk Velocity and the New Electric Field

As it is easy to note, the x-component of the magnetic field, described in the previous paragraph, is an even function respect to $x = 0$ plane while the z-component is odd. With these parity conditions, the parallel electron bulk velocity $v_{e\|}$ is odd respect to $x = 0$ plane (this can be inferred from the equation (2.23)). This means that it must satisfy $v_{e\|} = 0$ on this plane; the product of charge density function n (even function) and parallel electron bulk velocity is once more an odd function, then the value of f in the *Sec.* 3.2.2 is 0 on the plane $x = 0$. We choose this plane as the reference one and it is sufficient to integrate the equation (3.24) with the magnetic field line equation on a half-space (*i.e.* $x > 0$), because we are able to reconstruct the

function $v_{e\|}$ on the whole simulation box with the condition $v_{e\|}(x, y, z) = -v_{e\|}(-x, y, z)$ for any values of x, y, z on the mesh.

In order to solve the equation (2.32) we need to specify the value of electron temperature T_e and the value of φ on the boundaries of the simulation box. For the electron temperature T_e we make the assumption that $T_e \approx 1/5 < T_i >_{xyz}$ (the average is over x, y and z directions) as in [89, 72, 43, 115] and as frequently observed in the magnetotail [11]; observations, indeed, have estabilished that in the plasma sheet the ion temperature is almost always greater than the electron temperature. In [96] the authors performed a statistical survey using ISEE 3 satellite data, and it was found that the ion to electron temperature ratio (T_i/T_e) varied between 4.8 and 7.8 in the deep magnetotail from 30 to 220 R_E downtail (see also [11]). In the near-Earth magnetotail, a statistical study of the plasma sheet using Active Magnetospheric Particle Tracer Explorer (AMPTE) satellite data showed that more than 80% of the particle data measurements fell within the range $5.5 < T_i/T_e < 11$, with a best fit in the inner central plasma sheet of $T_i = 7.8\ T_e$ [9]. More recent Geotail satellite observations shows that on average $T_i \sim 5T_e$.

For the value of φ on the boundaries of the simulation box, we impose that on the boundary planes, where $B \sim B_0$ (the lobe value), the new electric field has the constant value $E_y = E_0$, so that $\varphi_0 = -E_0 \Delta y$, where Δy is the y-displacement along the magnetic field line.
Moreover from the same parity arguments explained above, the electrostatic potential φ is an even function, so it is sufficient to integrate the equation (2.32) in the positive half-space, and then $\varphi(x, y, z) = \varphi(-x, y, z)$ for any value of x, y, z on the mesh.

Chapter 4

Checks of Accuracy and Internal Consistency of the Simulation Algorithm

Having developed a simulation code for the analysis of the magnetotail current sheets, we call attention to the question of the accurancy of the calculations, that is how sensitive are the results to the numerics. In the following sections we briefly discuss a few simple numerical checks which are performed to be certain that the obtained results are not influenced by numerical inaccuracy, which is useful in differentiating between physics and numerics.

4.1 Numerical Check on Ion Moments

The granularity of a particle representation inevitably introduces short-scale fluctuations, which are superimposed upon a smoother component. The averaged amplitude of these flucuations is proportional to $\sqrt{N_c}$, where N_c is the ion number per cell. The ratio of the averaged amplitudes of the fluctuations to the slowly varying component varies as $1/\sqrt{N_c}$. In the real systems these fluctuations cause particles to be scattered at frequency which we call the collision frequency. Because our numerical model typically uses far fewer particles than are present in reality, the effect of these fluctuations is greatly enhanced. This produces anomalously large collision frequencies. We need to take steps to reduce the significance of these fluctuations. Fortunately we do not need to reduce the fluctuation amplitudes to their correct values, but merely to levels at which they no longer influence the particles significantly during the course of our simulation. There are two ways to reduce the importance of the statistical fluctuations, either by increasing the number

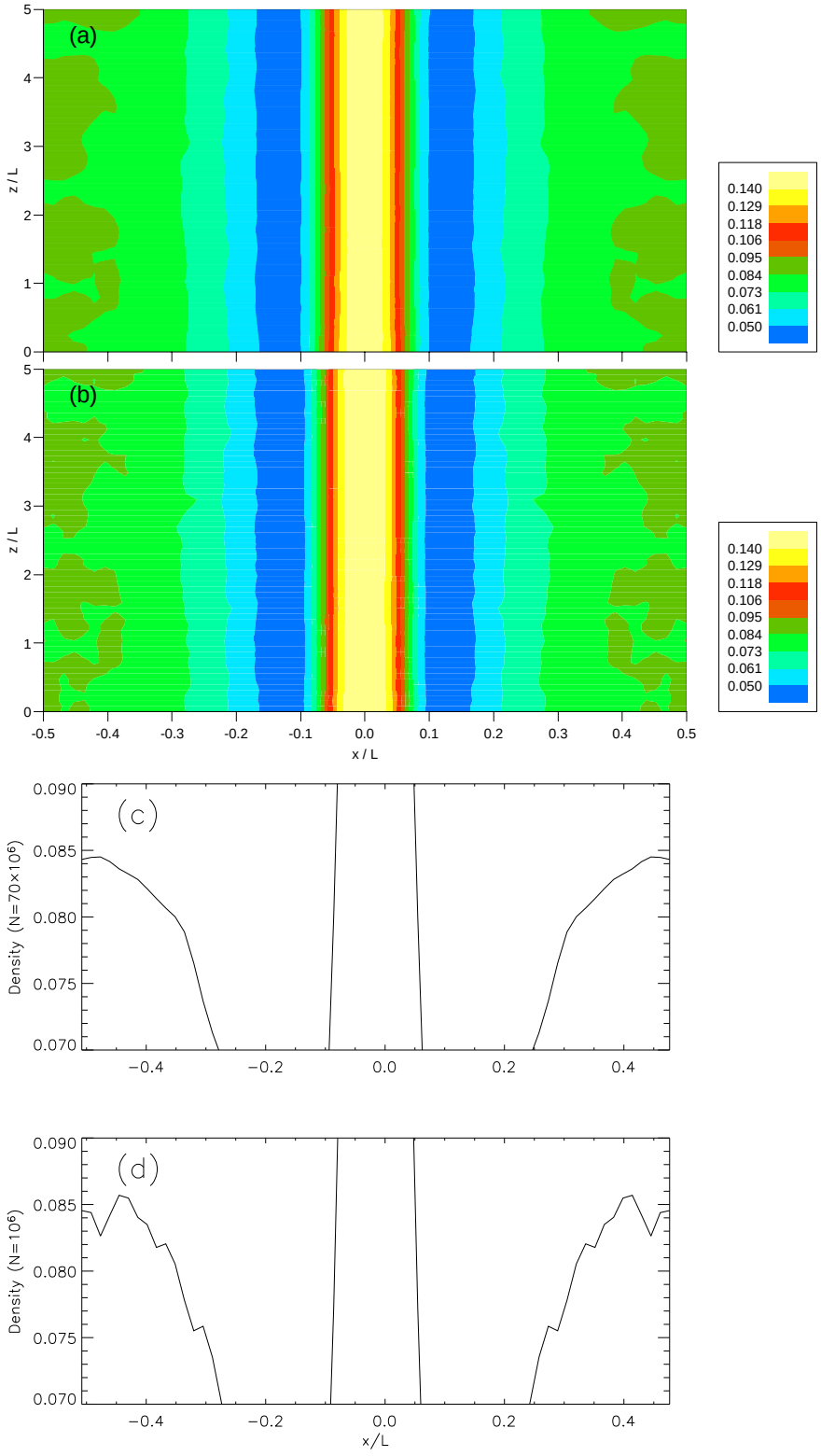

Figure 4.1: Two-dimensional contour plots of dimensionless ion density n_i in the meridian plane for two different numbers of injected ions: N=70×10^6 (panel (a)) and N=10^6 (panel (b)). The contours are computed for a fixed position along y. Fixing the position along z, too, the zoom in on a certain area shows the noise level of the ion density vertical profiles for N=70×10^6 (panel (c)) and N=10^6 (panel (d)).

of particles per cell, or by decreasing the grid size. One simple numerical test was to vary the number of simulation macroparticles from 10^6 ($\sim$244 particles/cell) to about ten milions (typically 2441-17090 particles/cell), on a three-dimensional grid of $N_x \times N_y \times N_z = 64^3$ points. Increasing the number of particles, reduces the noise level, however it is very dufficult to reduce this noise by increasing the number of particles, N, since statistical noise only decreases as $1/\sqrt{N_c}$ for random loading. Moreover, there is a tradeoff, as more particles increases the run time, and hence the expense of the calculation, for this reason we used 70×10^6 particles because it seemed a good compromise between the run time and the statistical fluctuations, which are reduced from $\sim 10\%$, for runs with $N=10^6$ particles, to $\sim 1\%$ (see Figure 4.1).

4.2 Numerical Check on Electron Velocity

We obtain the electron parallel bulk velocity $v_{e\parallel}$ by solving the advection-reaction equation (3.24) with a Semi-Lagrangian scheme (see *Ch.* 3). The integration procedes by steps from the initial point $\mathbf{r}_0$ towards the point $\mathbf{r}$. An approximate solution f is computed at each step. For each solution of f, the error made in the step, that is the local error, is estimated. The step size is choosen authomatically so that the integration will proceed efficiently, while keeping this local error estimate smaller than a tolerance that we specify by means of a parameter TOL in the simulation code, being TOL the desired relative accuracy. Roughly speaking, the code produces a solution that satisfies the differential equation (3.24) with a discrepancy bounded in magnitude by the error tolerance. To judge the accuracy of the numerical solution, we vary TOL from 10^{-3} to 10^{-12}.

Tolerance (TOL) values
10^{-3}
10^{-5}
10^{-7}
10^{-10}
10^{-12}

If we assume that the number density n is constant and that $\partial/\partial z$ and $\partial/\partial y << \partial/\partial x$, an analytical solution of equation (3.24) can be explicitly

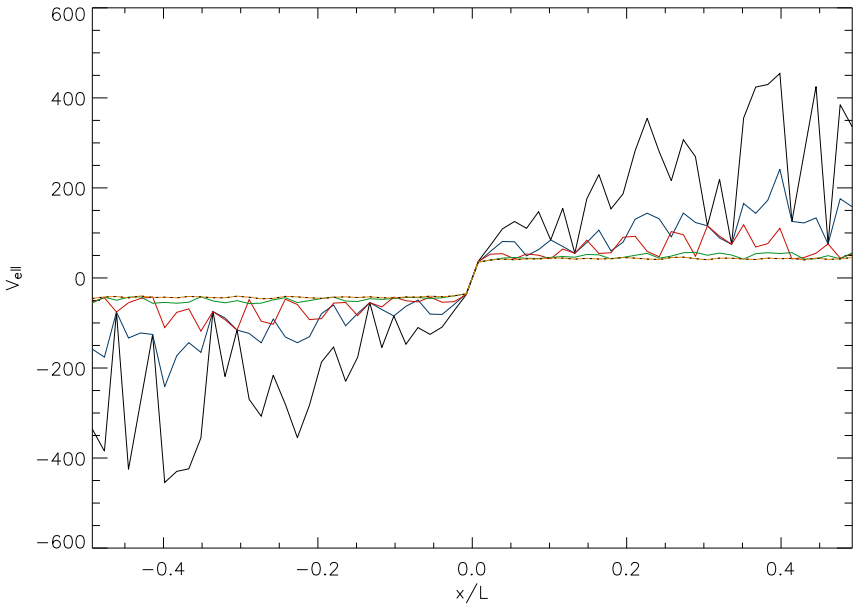

Figure 4.2: Vertical profiles of the electron parallel bulk velocity for different tolerance values: TOL=10^{-3} (black line), TOL=10^{-5} (blue line), TOL=10^{-7} (red line), TOL=10^{-10} (green line), TOL=10^{-12} (yellow line). The analytical solution (short-dashed line) coincides rather well with the electron parallel bulk velocity computed for TOL=10^{-12}.

written down. With the assumptions given above, the electron perpendicular bulk velocity components (see the equation (2.20)), in the dimensionless form, become:

$$v_{e\perp x} \approx \frac{E_y B_{0z}}{B^2}; \qquad v_{e\perp y} \approx -\frac{\partial p_e}{\partial x}\frac{B_{0z}}{nB^2}; \qquad v_{e\perp z} \approx -\frac{E_y B_n}{B^2} \tag{4.1}$$

giving an analytical expression for the function Φ

$$\Phi \approx -n\frac{d}{dx}\left(v_{e\perp x}\right) = -n\frac{d}{dx}\left(\frac{E_y B_{0z}}{B^2}\right) = -nE_y\frac{dB_{0z}}{dx}\left(\frac{B^2 - 2B_{0z}}{B^4}\right), \tag{4.2}$$

where $B = \sqrt{B_n^2 + B_{0z}^2}$ is the magnitude of the magnetic field. The continuity equation in the Cartesian coordinates (equation (2.22)) yields

$$n\frac{d}{dx}\left(v_{e\parallel}\frac{B_n}{B}\right) \approx \Phi = -n\frac{d}{dx}\left(\frac{E_y B_{0z}}{B^2}\right) \tag{4.3}$$

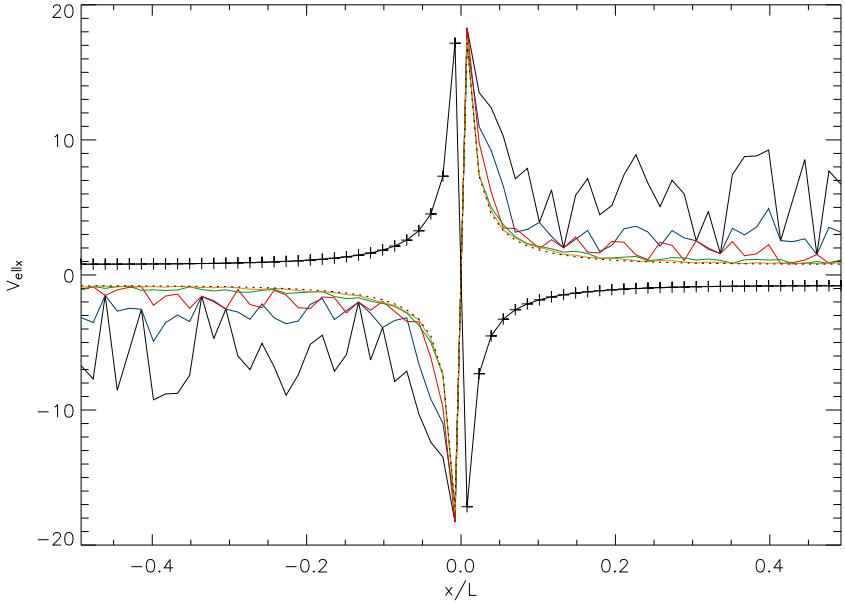

Figure 4.3: Vertical profiles of the electron parallel bulk velocity $v_{e\|x}$ for different tolerance values: TOL=10^{-3} (black line), TOL=10^{-5} (blue line), TOL=10^{-7} (red line), TOL=10^{-10} (green line), TOL=10^{-12} (yellow line). The electron parallel bulk velocity computed for TOL=10^{-12} rather coincides with the analytical solution (short-dashed line) that is the opposite of the perpendicular electron bulk velocity $v_{e\perp x}$ (black line with crosses).

and the analytical expression for electron parallel bulk velocity can be computed:

$$v_{e\|} \approx -\frac{1}{B}\frac{E_y B_{0z}}{B_n} \tag{4.4}$$

At this point, we integrate, with the Semi-Lagrangian method explained in *Ch.*3, the equation

$$\frac{d}{dx}\left(v_{e\|}\frac{B_n}{B}\right) = -E_y\frac{dB_{0z}}{dx}\left(\frac{B^2 - 2B_{0z}}{B^4}\right)$$

varying TOL, in order to obtain the numerical value of $v_{e\|}$. In the Figure 4.2 a comparison between the numerical and analytical solutions of the electron parallel bulk velocity is presented in terms of the tolerance values listed in the table above. We can note that the level of noise drastically decreases with the value of TOL, so that the numerical solution approaches to the

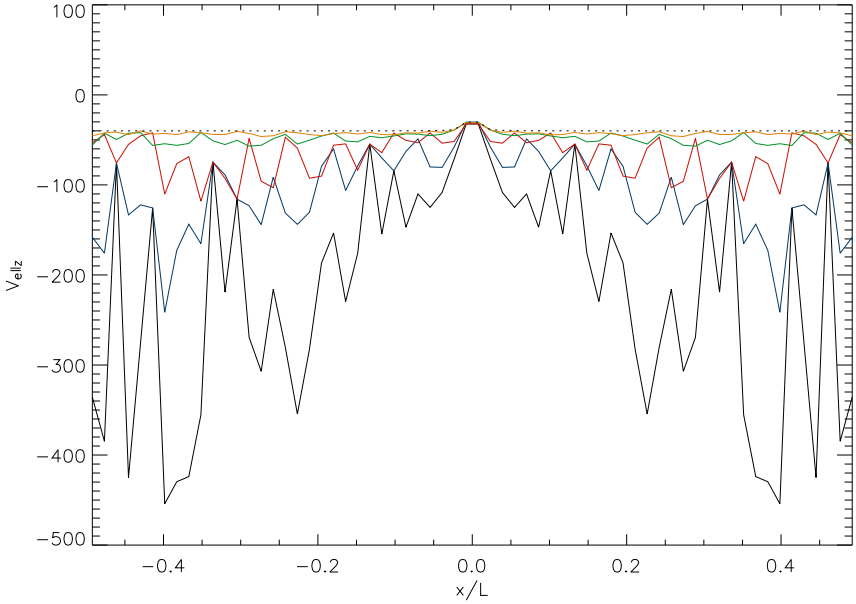

Figure 4.4: Vertical profiles of the electron parallel bulk velocity $v_{e\|z}$ for different tolerance values: TOL=10^{-3} (black line), TOL=10^{-5} (blue line), TOL=10^{-7} (red line), TOL=10^{-10} (green line), TOL=10^{-12} (yellow line). The analytical solution (short-dashed line) rather coincides with the electron parallel bulk velocity computed for TOL=10^{-12}.

analytical expression for $v_{e\|}$ (short-dashed line). The analytical expression for the x component of the electron parallel bulk velocity is

$$v_{e\|x} = v_{e\|}\frac{B_n}{B} \approx -\frac{E_y B_{0z}}{B^2} \tag{4.5}$$

which, in turn, is opposite to $v_{e\perp x}$, then $v_{ex} = v_{e\|x} + v_{e\perp x} \sim 0$. The expression for the z component of $v_{e\|}$ is

$$v_{e\|z} \approx -\frac{E_y B_{0z}^2}{B_n B^2}\,. \tag{4.6}$$

The run results with such tolerance values for $v_{e\|x}$ and $v_{e\|z}$ are plotted in Figure 4.3 and Figure 4.4, respectively. As seen in the Figures, there is again a reduction in the numerical noise, resulting in a smoother profile (yellow line -TOL=10^{-12}- of Figures 4.3 and 4.4) and a rather good convergence of the model results to the analytical solution (short-dashed lines of the two Figures)

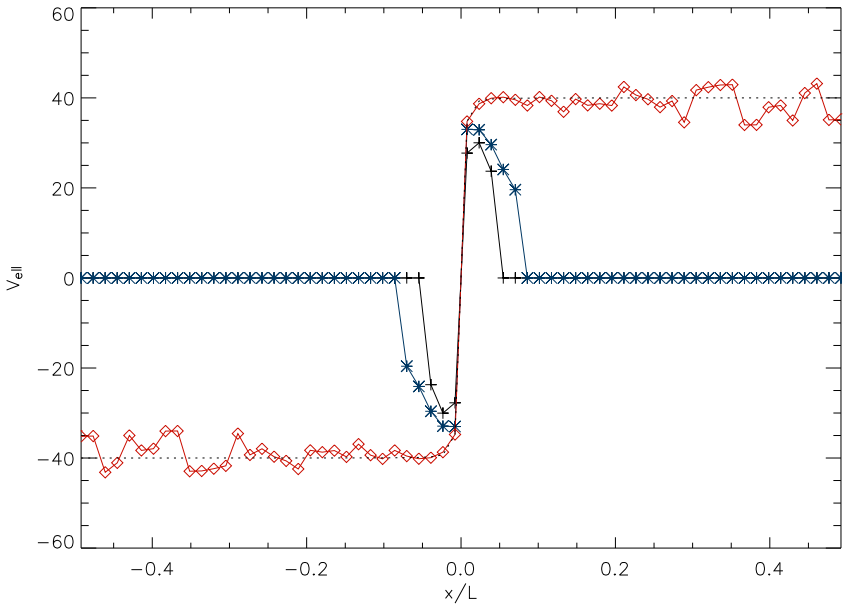

Figure 4.5: Vertical profiles of the electron parallel bulk velocity for different x spatial resolution and TOL=10^{-12}: N_x=128 (black line), N_x=256 (blue line), N_x=1024 (red line). The analytical solution (short-dashed line) rather coincides with the electron parallel bulk velocity computed for N_x=1024.

with decreasing tolerance. Clearly, since the numerical solution approaches better to the expression (4.5), we have the validation that $v_{ex} \sim 0$.
Making TOL smaller should normally make the integration more expensive. However, in the range of tolerances we used, the increase in cost is modest.

Once we have checked that the most suitable value of TOL which we can use is TOL=10^{-12}, we tested the simulation on the electrons by decreasing the step size used in the spatial discretization scheme. The accuracy of the method is assessed by integrating the equation (3.24) on a three-dimensional grid of fixed arbitrary number of points along y and z respectively, and varying the spatial resolution with 128, 256 and 1024 points along x; we think that the most significant effects and variations, as pressure gradient terms, are along x direction, whereas z is the statistically ignorable coordinate and the y dependence is weak. We again consider the number density constant and $\partial/\partial y$ and $\partial/\partial z << \partial/\partial x$. Unlike the previous case when we use the analytical expression of Φ (equation (4.2)), this time we evaluate the function

Φ by means of the interpolation of the following expression

$$\Phi \approx -n\frac{d}{dx}\left(v_{e\perp x}\right) \tag{4.7}$$

on a grid of $N_x \times N_y \times N_z$, varying N_x with 128, 256 and 1024 points, and we again integrate the equation

$$\frac{d}{dx}\left(v_{e\parallel}\frac{B_n}{B}\right) \approx -\frac{d}{dx}\left(v_{e\perp x}\right)$$

with the well-known Semi-Lagrangian method. A comparison is presented between the numerical and analytical solutions in terms of the increasing spatial resolution (Figure 4.5). Qualitatively, the comparison of the numerical to the analytical solutions indicates good agreement when we use N_x =1024. The results of varying the spatial resolution of the numerical model indicate rapid convergence to the analytical solution (short-dashed line) with increasing resolution (red line).

4.3 Summary and Conclusions

We have considered the important issue of the effect of the inherent noise in the simulation of the ions. As we have shown in detail, increasing the number of simulation macroparticles reduces the numerical noise level from 10% for runs which have 10^6 macroparticles, to 2% when we inject 70 $\times 10^6$ ions in the simulation box.

We have also discussed two numerical tests to check the accuracy of the electron calculations. An analytical solution has been presented for the case of constant number density and quasi-null y and z partial derivatives. The analytical solution is useful for the validation of the model. We considered the comparison of the numerical and analytical solutions of the electron parallel bulk velocity and its components in terms of the tolerance value. We had TOL=10^{-3} as well as TOL=10^{-5}, TOL=10^{-7}, TOL=10^{-10} and TOL=10^{-12}. Decreasing the tolerance we can observe a well defined decrease of numerical fluctuations, resulting in a rather good convergence of the model to the analytical solution when we have the lowest value of tolerance. The numerical results for three different grid resolutions (N_x=128, N_x=256, N_x=1024) have also been presented as an example of how the analytical solution can be used for such validation processes. The numerical results with the highest spatial resolution were shown to converge to that of the analytical model.

The results presented in the following refer to runs with a value of tolerance equal to 10^{-12}. The ion motion is integrated on a simulation grid of 64^3

points. For the function Φ, the spatial grid is made up of $2048 \times 16 \times 16$ mesh points, in order to resolve better its characteristic variations around $x = 0$. Then, the electron moments are computed on a simulation grid of 64^3 points, as well as the ions.

Chapter 5

Numerical Results

Lastly, we conclude the presentation of our simulation code with the description of the recent state of the art. In the version of code discussed here, various quantities are plotted out. These include the x vertical profiles and two-dimensional contour plots of electromagnetic fields and various moments of the ion distribution function plotted for specified number of particles to study the effect of the inherent noise in the simulation. These profiles are plotted with scales that adjust the minimum and the maximum value displayed in order to insure that all important effects are visible.

5.1 Ion Moment Results

The self-consistent system of equations for the plasma density and the other ion moments, the magnetic and electric fields, the total and the partial (ion and electron contributions) current densities as well as the electrostatic potential are solved numerically when we inject 70×10^6 ions and we use a value of the normal magnetic component $B_n = 0.02B_0$. The ion injection energy corresponds to 0.8 keV and the drift velocity at the edges of the simulation box equal to $v_D = 500$ km/s. We also define $\epsilon = v_{th}/v_D$ as a parameter which quantifies the ion source anisotropy of the injection distribution function. These plasma parameters have been choosen to be close to the observed values in the Earth's magnetotail [6]. The first results of this model are shown in Figure 5.1, where the vertical profile and two-dimensional contours of ion density n_i are plotted. In the top panel, the ion density on the xy-plane is diplayed, panel (a), and in the meridian plane xz, panel (b). It can be seen that the density has relatively small variations along y and z directions (save for some very weak variations near the sides where some boundary effects are found), therefore we can consider these directions as statistically

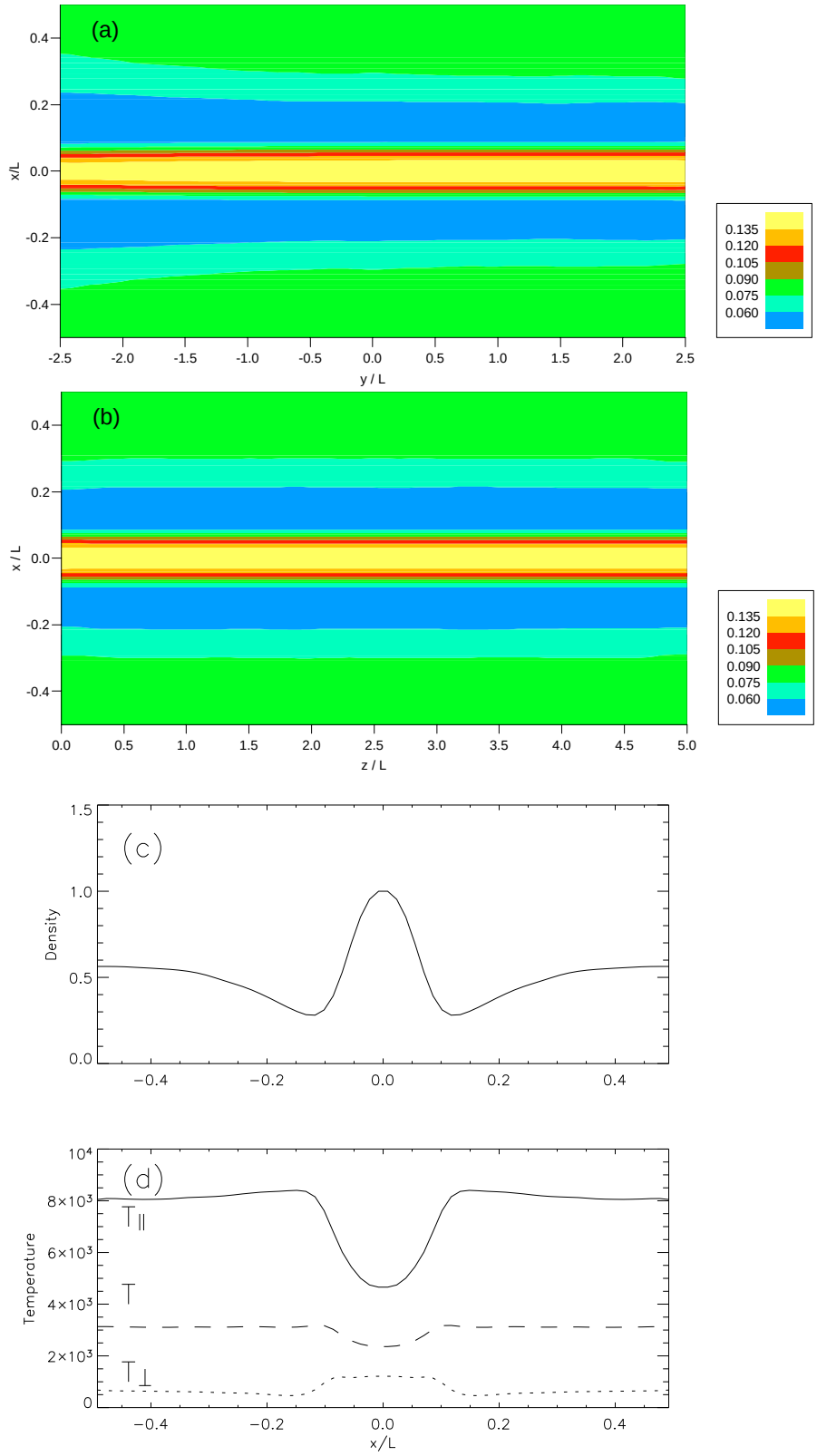

Figure 5.1: Top: two-dimensional contour plots of dimensionless ion density n_i: in the xy-plane (panel (a)) and in the meridian one (panel (b)). On the middle (c) and in the bottom (d) panels, density and temperature vertical profiles are shown in units of density peak value and $m_i V_E^2/k_B$, respectively.

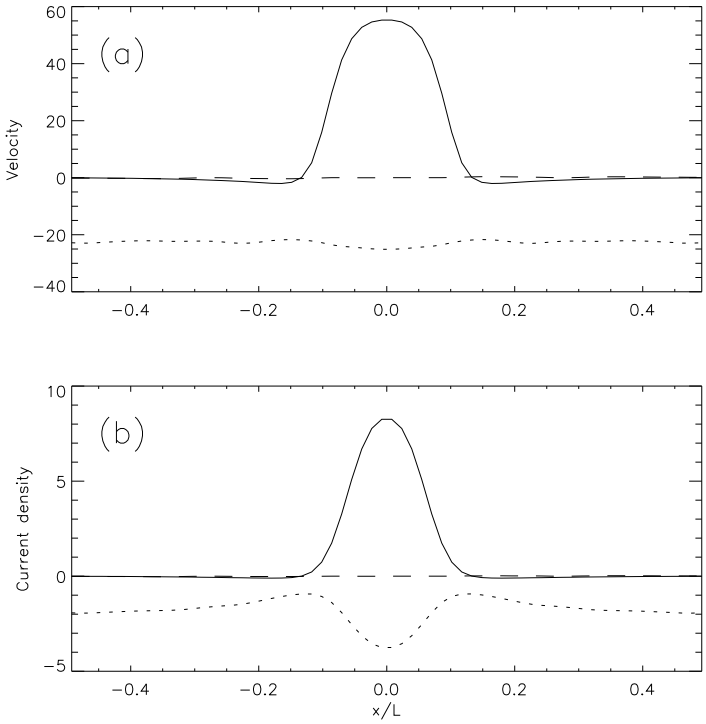

Figure 5.2: Panel (a): vertical profiles of velocity components V_x (long dashes), V_y (solid) and V_z (short dashes). Panel (b): vertical profiles of velocity components J_{ix} (long dashes), J_{iy} (solid) and J_{iz} (short dashes). Ion velocities are in units of V_E and ion current densities in units of $cB_0/4\pi L$.

homogeneous. Then ion density, as well as the other ion distribution function moments in the following, has been averaged over z and y, to show the characteristic dependence on the x coordinate (Figure 5.1, panel (c)).
The vertical profile of the temperature at the bottom of Figure 5.1 (panel (d), long-dashed line) is rather flat and temperature appears to be increased with respect to the injection value ($\simeq$ 20 times larger). In addition, the ions are heated in the direction perpendicular to the magnetic field resulting in a smaller temperature value in the central region, which may be roughly characterized in terms of ion $T_\parallel$ (solid line) temperature, and two small peaks at $|x| \simeq 0.1$ L due to the mixing of incoming ions, which have large velocity dispersion, with ions performing mandering orbits (see [25]). Note that there are substantial differences between $T_\parallel$ and $T_\perp$ (short-dashed line), showing that the heating is rather anisotropic.

From the panel (a) of Figure 5.2, it can be seen that the x component of

the bulk velocity V_x (long-dashed line) is smaller than V_y (solid line) and V_z (short-dashed line), it is zero on average and there are no spatial features. This means that at any location in the simulation box there are as many particles going up along x as many going down. On the other hand, V_y is oriented along the electric field $E_0 = E_y$, and it is clearly larger in the central region around $x = 0$, where $|B_{0z}|$ is smaller and the ions are unmagnetized. The z component V_z is negative. Taking into account the fact that the z axis in our system of coordinates is orientated toward the Sun, this means that the plasma flow is toward the Earth, the well known Earthward convection due to the dawn-dusk electric field [25].

The panel (b) of the Figure 5.2 displays the three components of the ion current density $\mathbf{J}_i$: the current density has features similar to the ion bulk velocity. As for V_z, the z component of current density is a current toward the Earth and it is not a drift current because in the centre of the current sheet ions are not magnetized ($B_{0z}(0) \sim 0$). Both V_y and J_{iy} (solid line) vertical profiles are narrow and peaked and they do not exhibit any bifurcated structure, according to the fact that the level of magnetic fluctuations is zero and that the ratio between the ion thermal velocity and streaming velocity at injection is very small [25]. Indeed, the value of the anisotropy parameter is $\epsilon \sim 0.3$ and the obtained one-peaked density profile is in agreement with the analytical results of [92]. Beside, J_{iy} presents negative values around $z \sim \pm 0.2$ L due to the diamagnetic currents. This diamagnetic current is made up of three contributions: the ∇B drift, the curvature drift and the magnetization currents [76, 112]. These negative current "wings" are not so important for the choosen value of normal magnetic field component, but they could become very profound for larger value of B_n (see later).

5.2 Electron Moment Results

By solving the equation (2.20), the perpendicular electron velocity components are obtained. The profiles of the velocity components are shown in the panel (a) of Figure 5.3. The x and z components ($v_{e\perp x}$ is shown with long-dashed line and $v_{e\perp z}$ with short-dashed line) are completely due to the electric drift term and they are equal to

$$v_{e\perp x} = \frac{E_y B_{0z}}{B^2} \tag{5.1}$$

$$v_{e\perp z} = -\frac{E_y B_n}{B^2}\,; \tag{5.2}$$

where $\mathbf{B} = \mathbf{B}_{0z}(x) + \mathbf{B}_n$; indeed, the pressure gradient term does not contribute because the z and y derivatives are neglegible respect to the x deriva-

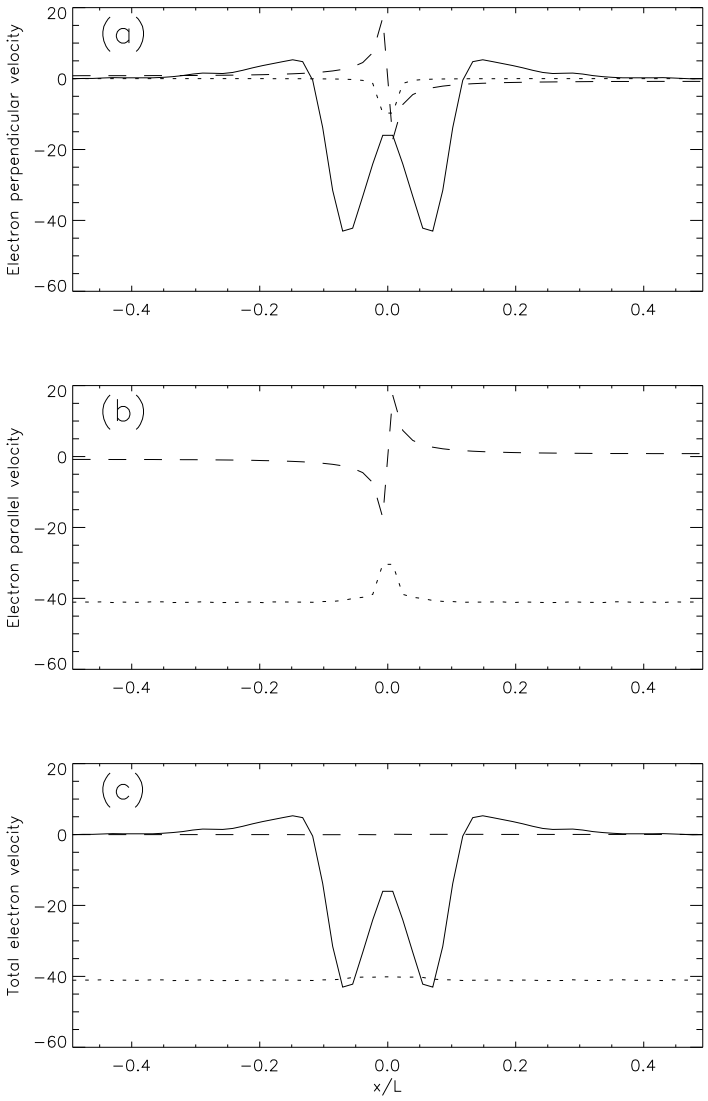

Figure 5.3: Panel (a): vertical profiles of the three components of the electron perpendicular bulk velocity: $v_{e\perp x}$ (long dashes), $v_{e\perp y}$ (solid) and $v_{e\perp z}$ (short dashes). Panel (b): vertical profiles of the two non-null components of the parallel electron bulk velocity: $v_{e\parallel x}$ (long dashes), $v_{e\parallel z}$ (short dashes). Panel (c): vertical profiles of total electron velocity: v_{ex} (long dashes), v_{ey} (solid) and v_{ez} (short dashes). Electron velocities are in units of V_E.

tive (being z the statistically ignorable coordinate and y dependence weak). On the contrary, the y component of the electron perpendicular velocity

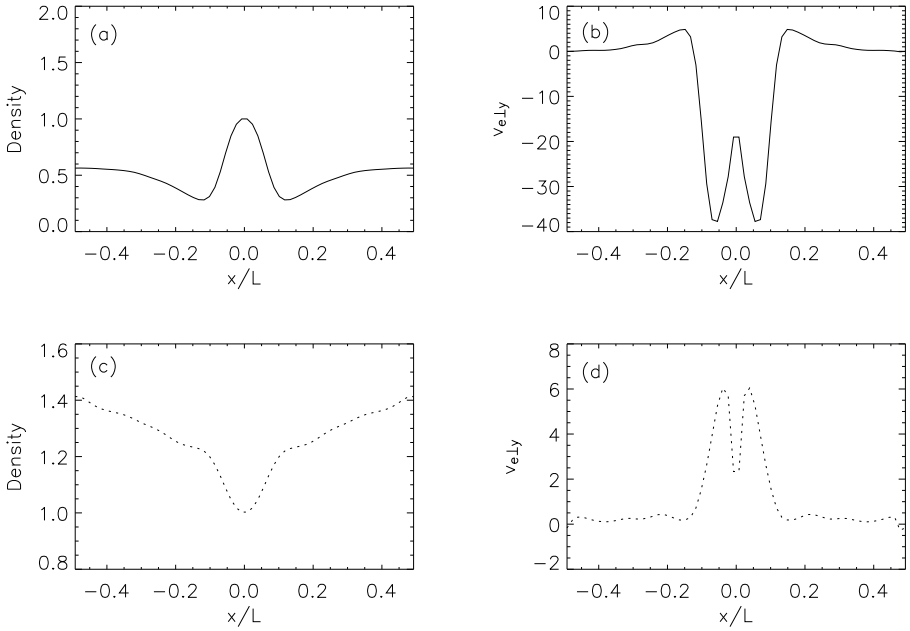

Figure 5.4: The dependence of the sign of $v_{e\perp y}$ on the shape of ion number density. Top: vertical profile of number density (panel (a)) and $v_{e\perp y}$ (panel (b)). Here $B_n = 0.02B_0$ and $v_D = 500$ km/s. Bottom: vertical profile of number density (panel (c)) and $v_{e\perp y}$ (panel (d)). Here $B_n = 0.05B_0$ and $v_D = 500$ km/s. Ion density vertical profiles are shown in units of density peak and electron perpendicular bulk velocity in units of V_E.

(displayed with solid line) is dominated by the x pressure gradient term as

$$v_{e\perp y} = -\frac{B_{0z}}{neB^2}\frac{\partial p}{\partial x} \tag{5.3}$$

and it shows a bifurcated structure which comes out from the combination of the x derivative of the electron pressure (or density) and the sign reversal field B_{0z}. At this point it is important to note that the sign of the y component of the electron perpendicular velocity depends on the shape of the ion density along x vertical direction: if it presents a peak (panel (a) of Figure 5.4, solid line) in the centre of the current sheet (as for this choice of parameters) then the y component of the electron perpendicular velocity is mostly negative (panel (b) of Figure 5.4, solid line), otherwise, if density has a depression around $x = 0$ (panel (c)), as for example when we use a new value for the normal magnetic field $B_n = 0.05B_0$ and the same drift velocity at the edges of the simulation box equal to $v_D = 500$ km/s, whereas we inject 50×10^6 ions

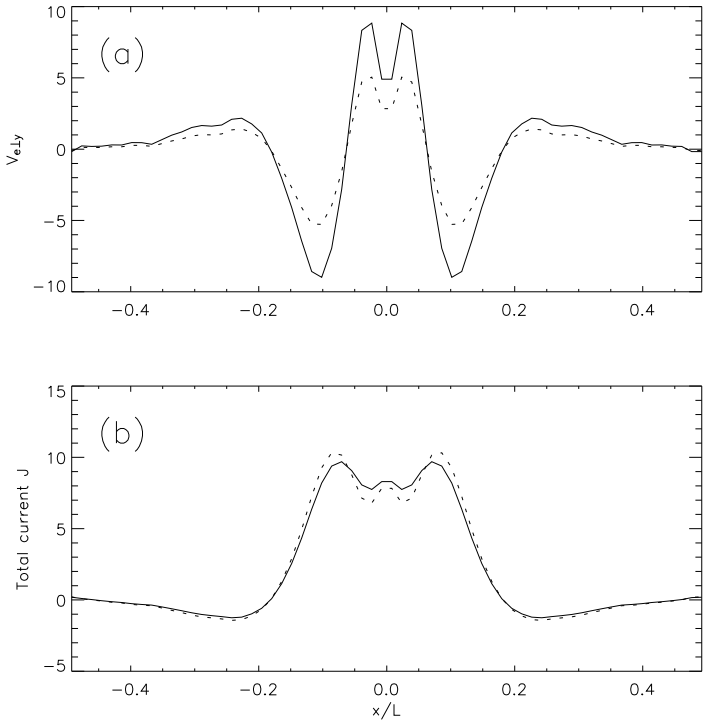

Figure 5.5: The behaviour of the electron bulk velocity respect with the equation of state, *i.e* isothermal (solid line) or adiabatic (short-dashed line). Panel (a): vertical profiles of y component of electron bulk velocity. Panel (b): vertical profiles of total current density along y. Velocities and currents are in units of V_E and $cB_0/4\pi L$, respectively. The total result seems to be insensitive to the use of different equations of state.

with a larger energy corresponding to about E_K=4.4 keV, then the electron perpendicular velocity along y is mostly positive (panel (d)). Beside, the behaviour of this component of the electron bulk velocity could depend on the equation of state, *i.e* isothermal or adiabatic. Actually, as shown in Figure 5.5, when we sum together the ion and electron current densities, the total result seems to not feel the effect of different equations of state.

By solving the equation (2.24) the parallel electron bulk velocity is computed. If we suppose that $\partial/\partial z$ and $\partial/\partial y << \partial/\partial x$, we could write the equation (2.24) as :

$$B_n \frac{\partial}{\partial x}\left(\frac{n v_{e\parallel}}{B}\right) \approx -\frac{\partial}{\partial x}\left(n v_{e\perp z}\right) \tag{5.4}$$

The analitical solution of equation (5.4) yields two results: first we obtain that $nv_{ex} \sim 0$, which means that $v_{ex} \sim 0$; second the expression of $v_{e\|} \approx -(E_y B_{0z})/BB_n$ is also obtained. The vertical profiles of the velocity components are shown in the middle panel of Figure 5.3. The x-component of the parallel electron bulk velocity is depicted with long-dashed line; it shows a bipolar variation in the centre of the neutral sheet, around $x \simeq 0$: $v_{e\|x} < 0$ at $x > 0$ and $v_{e\|x} > 0$ at $x < 0$. This indicates an equal but opposite flux of electrons moving along magnetic field from the edges to the centre of the current sheet; it is opposite to the perpendicular component in order that the total electron bulk velocity along x (shown in the panel (c) with long-dashed line) is almost zero, as expected. The z component of the total electron bulk velocity is shown with short-dashed line and it is equal to the expected value $\approx -40V_E$; it is the largest component and this indicates a tailward flux in the center of the current sheet and a Earthward flux at the edges. Finally, according to our model parameters, the y velocity component is null.

Once we have the parallel and perpendicular electron bulk velocity, the electron current density is computed from the expression $\mathbf{J}_e = (nq_e\mathbf{v}_e) = nq_e(\mathbf{v}_{e\|} + \mathbf{v}_{e\perp})$, where n is the ion density and $q_e = -e$ is the electron charge. The ion number density obtained from a test particle simulation is defined in arbitrary units, therefore the electron current density $\mathbf{J}_e$ is known except for a free parameter, say n_0. We can fix it requiring that the total current along y direction (made up with the ion and electron contributions) has to be strong enough to reproduce the magnetic field B_{0z} on the planes $x = \pm 0.5$ L of the simulation box [25]. In order to have the right normalization, we have to multiply ion, electron and total current densities by this new value of n_0.

5.3 Total Current Density and Comparison with Observations

The panels (a)-(c) of Figure 5.6 show vertical profiles of x and z components of ion, electron and total current densities. Along the Earth-Sun line connection, the electron current density is almost opposite to the ion one, so the total current density is very small (the solid line in the top panel). Along the direction perpendicular to the current sheet no current density appears (the solid line in the panel (a)).
The y component of the total current density is displayed in the panel (b) of the same Figure 5.6 with the ion and electron contributions. It is clear from

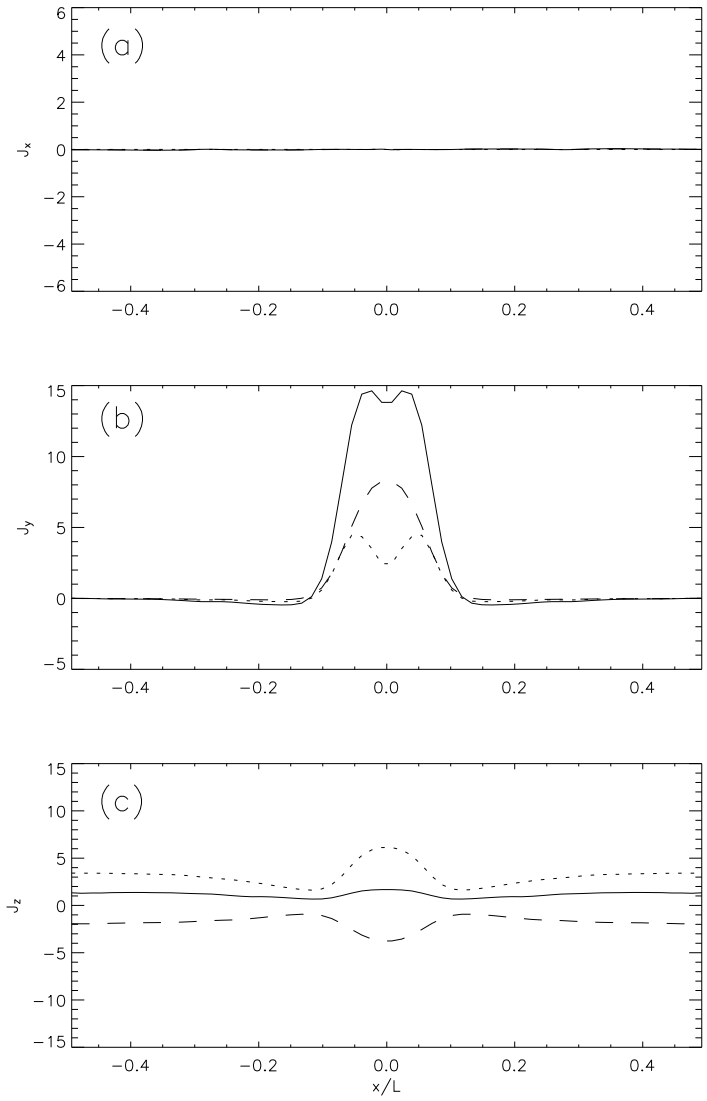

Figure 5.6: Vertical profiles of the dimensionless total current density (solid line), showing contributions of partial ion (short-dashes) and electron (long-dashes) current densities; x components on panel (a), y components on panel (b) and z components on panel (c), respectively. Currents are in units of $cB_0/4\pi L$.

this figure that both the ions and electrons contribute to the total cross-tail current: the role of electrons is the most substantial in the center of the current sheet [26], where they support a double peak structure embedded in

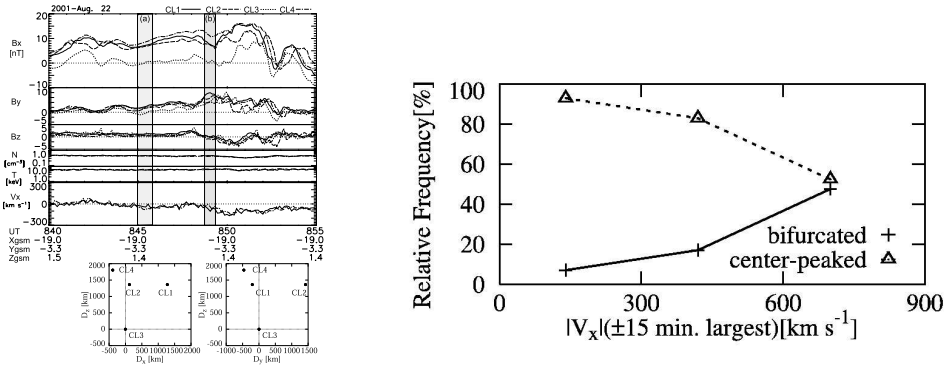

Figure 5.7: Left-hand panel: Cluster observation and position on interval under study in [6]. Rigth-hand panel: relative occurence frequency of bifurcated current sheets (solid line) and center-peaked current sheets (dotted line), from [6].

the ion current, although the ion net contribution is seen to be about 70 % of the total current density. In turns, the bifurcated structure in the electron current density derives from the finite Larmor radius term $\nabla p_e/ne$. The obtained profiles of the current density show the same spatial scale for ions and electrons. In [115], the authors consider an anisotropic electron pressure. Due to this anisotropy, they take into account the influence of curvature drifts, in electron current, which are predominant in a very narrow region in the center of the sheet (where the magnetic field clearly shows the larger curvature gradient). This leads to the narrow electron current maximum in the vicinity of the neutral plane, which is embedded inside a thicker ion current. In our model, the electron pressure is isotropic, so that the anisotropy effects are due to ions. Also in [10, 95], the electron anisotropy seems to be one of the most important physical explanation for the formation of bifurcated (and also tripled) structure of the current sheets. On the contrary, in [21] the authors invoke a resonant mechanism of scattering of crossing ions into non-crossing region of phase space. This leads to a charge separation across the current sheet which in turn produces an electrostatic potential. The latter produces the bifurcated structure in the enhanced electron flow velocity. The effect of bifurcation seem to be quite widespread in the tail of the Earth's magnetosphere. Recent *in-situ* measurements by Cluster spacecraft [6] have

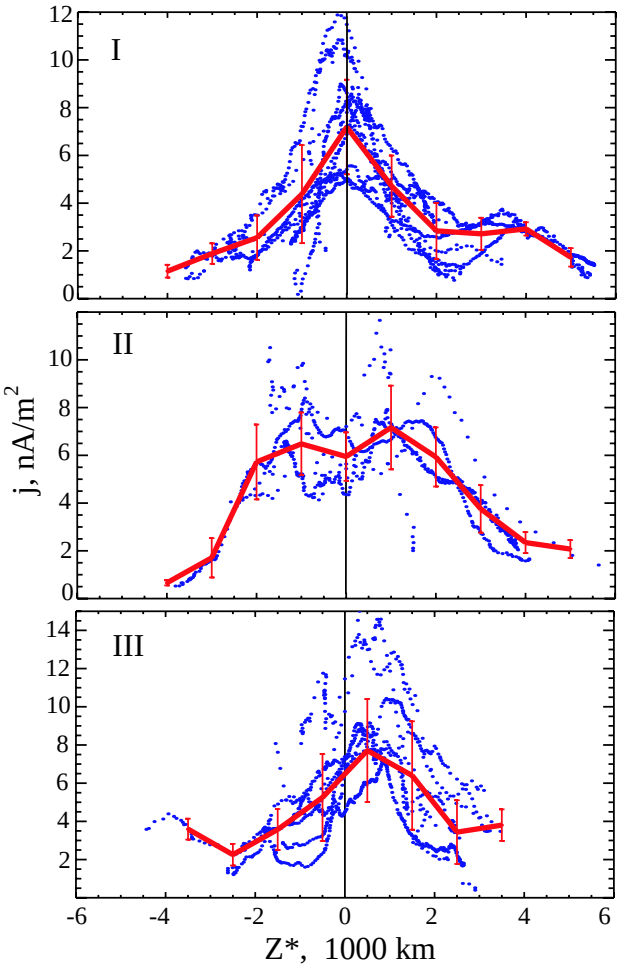

Figure 5.8: Summary of the current density distributions: center-peaked (type I), bifurcated (type II), and asymmetric (type III) current sheets together with the averaged vertical profiles (red lines).

shown that the occurence frequency of bifurcated current sheets is 17 %, in a current sheet of thickness of about $\sim$ 1500 km, without any fast flows or significant turbulence, and increases up to 48 % in association with fast flow, as shown in Figure 5.7 taken from [6]. Similar analysis performed for flapping current sheets, have given similar results [85]. Thus, the deviation from the Harris model seems to be significant, and it is most likely a stable effect rather than a transitory feature of the current sheet (see also [6, 105, 86]). The width of the bifurcated structure (Figure 5.6) is estimated as $\leq 1\lambda \sim$

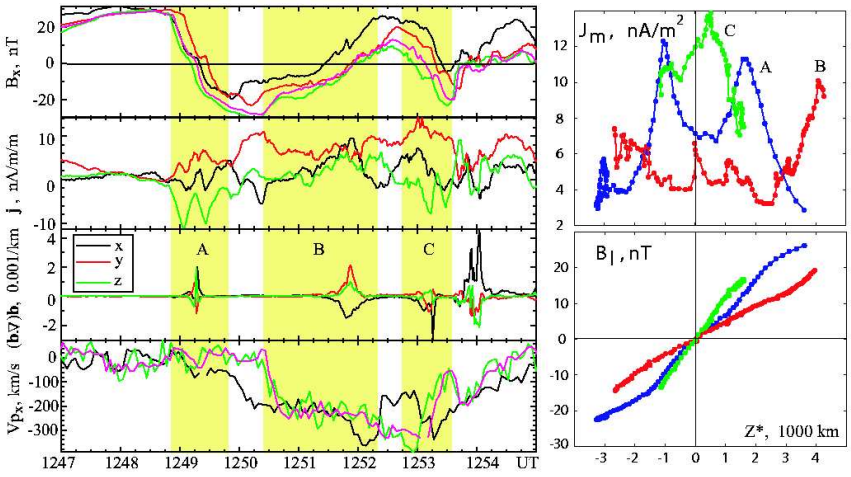

Figure 5.9: October 8, 2001: Cluster data (left panel); reconstructed vertical profiles of current density (cross-tail component) and magnetic field (rigth panels).

10 r_{Li}, where λ is the current sheet half thickness and r_{Li} is the ion Larmor radius at the edges. This means that we are describing a moderately thick current sheet and we are slightly above the typical length where ions are decoupled from electrons.

The analysis of some rapid crossing of the magnetotail current sheet by the Cluster spacecraft, during July-October 2001 at a geocentric distance of 19 R_E, [86] shows that three types of current sheet distributions are distinguished (center-peaked, bifurcated and asymmetric sheets) indicating that the typical scale of the bifurcated current structures is $\sim$ 4000 km (see middle panel in Figure 5.8), which corresponds to $\sim$ 10 r_{Li}. This is in good agreement with our numerical results which show a typical separation between the current peaks of about 2000-3000 km. Recently, using Cluster four-point measurements about magnetotail current sheet crossing of October 8, 2001 [84], the reconstructed spatial profiles of the cross-tail current density show that the electric current (depicted in Figure 5.9) has a typical intensity of about 12 nA/m^2 with an error of 20%; these observations agree well with the

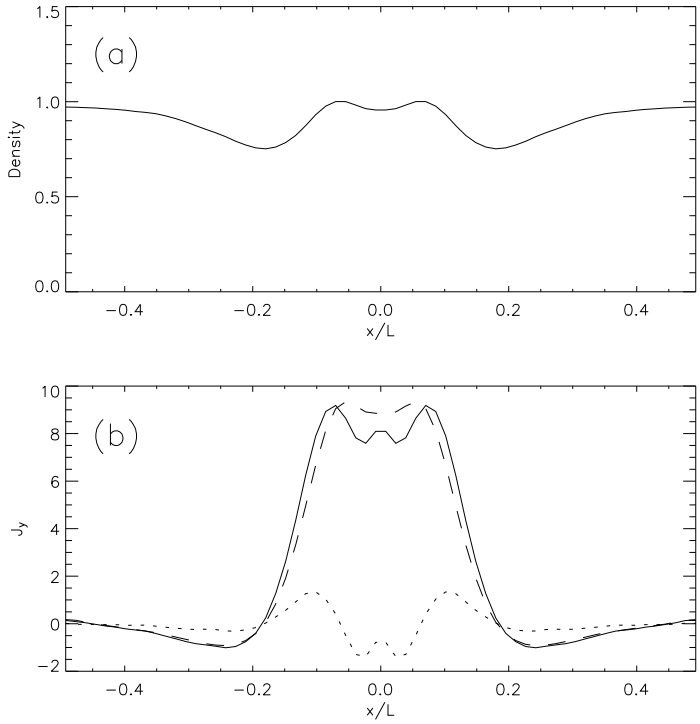

Figure 5.10: Panel (a): vertical profiles of n_i. Panel (b): vertical profiles of the y component of the ion current density (long-dashed line), electron current density (short-dashed line) and total current density (solid line). Density and current profiles are shown in units of density peak value and $cB_0/4\pi L$, respectively.

numerical peak value obtained from our simulation of $(14 \div 15)\ cB_0/4\pi\mathrm{L} \sim (11 \div 12)$ nA/m^2 (see Figure 5.6).

5.3.1 Three-peak Current Sheet

We now discuss the numerical results of the hybrid simulation when we use the same value of the previous run for normal magnetic field component $B_n = 0.02B_0$ and the same drift velocity at the edges of the simulation box equal to $v_D = 500$ km/s, whereas we inject 10^6 ions with a larger energy corresponding to about $E_K = 4.4$ keV. The panel (a) of Figure 5.10 shows the vertical density profile: the central peak is much broader and it is due to the larger Larmor radius of the ion orbits which move in the current sheet; this result is in good agreement with the study in [116] for large values of

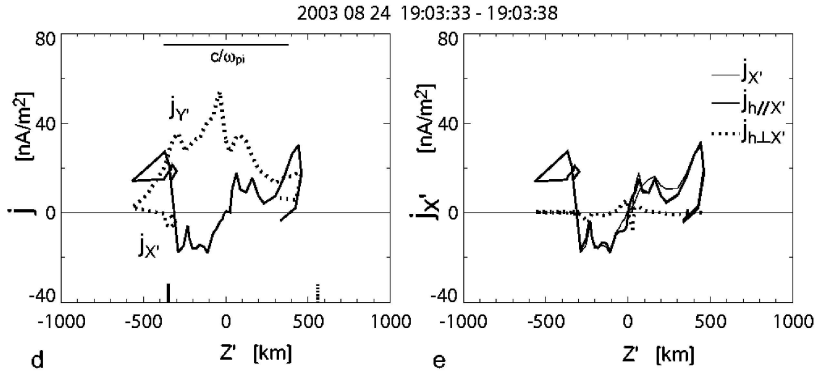

Figure 5.11: Reconstructed current density j_y (left-hand panel) and j_x obtained for the rapid current-sheet crossing event between 19:03:33 and 19:03:38 UT (from [64]).

the ion injection energies. On the panel (b), we display the y component of the total current density with the ion and electron contributions. The ion current density is also much broader and the electron one is partially negative; this profile of the electron current density is quite different from that one obtained using the previous set of magnetotail parameters. We argue that this could depend on the fact that the density profile has changed (see Figure 5.2 and 5.10) and in turn this influences the x derivative in the term $\nabla p_e/ne$. The most interesting result of this run is, however, the triple peak structure which appears in the total current density profile and which is due, once again, to the electrons. Some analytical models predict current sheets with a sharp peak at the center and secondary peaks at the edges due to the anisotropy of electron and/or ion temperatures [115, 95]. In Ref. [115], the authors obtain cross-tail current profiles with tripled peaks by using a one-dimensional self-consistent model based on the Vlasov-Maxwell equations which takes into account the electron anisotropy and a ratio between ion and electron temperature equal to 5. The dynamics of tripled-peak current

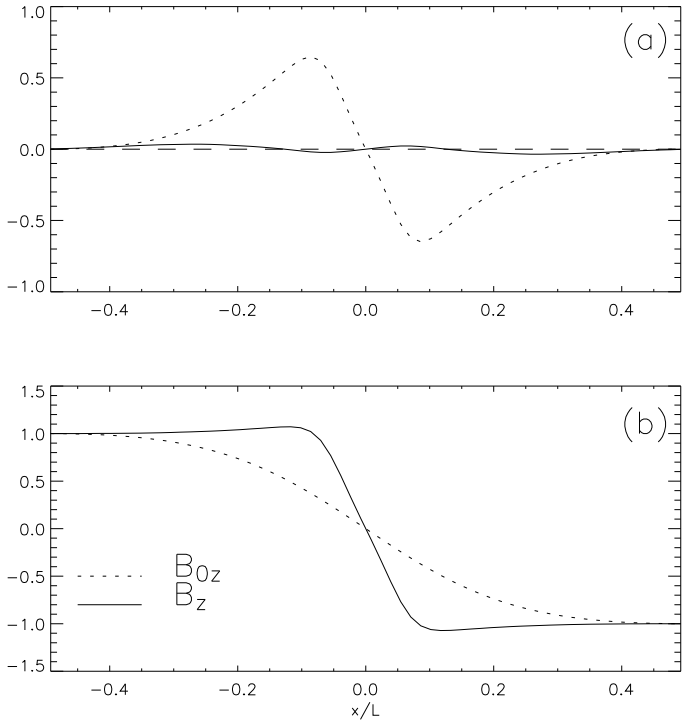

Figure 5.12: Panel (a): vertical profile of the magnetic field correction **b**: b_x (long-dashed line), b_y (solid line) and b_z (short-dashed line). Panel (b): vertical profile of the total magnetic z field component (solid line) and Harris field B_{0z} (short-dashed line). Magnetic field corrections are in units of B_0.

sheets are also explored using a full particle code with realistic ion anisotropy (η_i=1.2 ($T_{\parallel i} > T_{\perp i}$)) and an electron-to-ion mass ratio equal to 1/64 [95]. Such three-peaked current sheet profiles (Figure 5.11) were indeed found in the examination of the structure of thin current sheet and their evolution during a substorm interval on August 24, 2003, using multi-point Cluster data [64]. Although there is a single observation of triple-peak current sheets, up to now, it seems interesting to investigate this new class of equilibria, too.

5.4 Field Results: New Magnetic Field

The top panel of Figure 5.12 displays the vertical profile of the non-null component of the magnetic field correction **b**: namely b_z. The b_x component is almost zero because it is proportional to the y and z derivatives of the

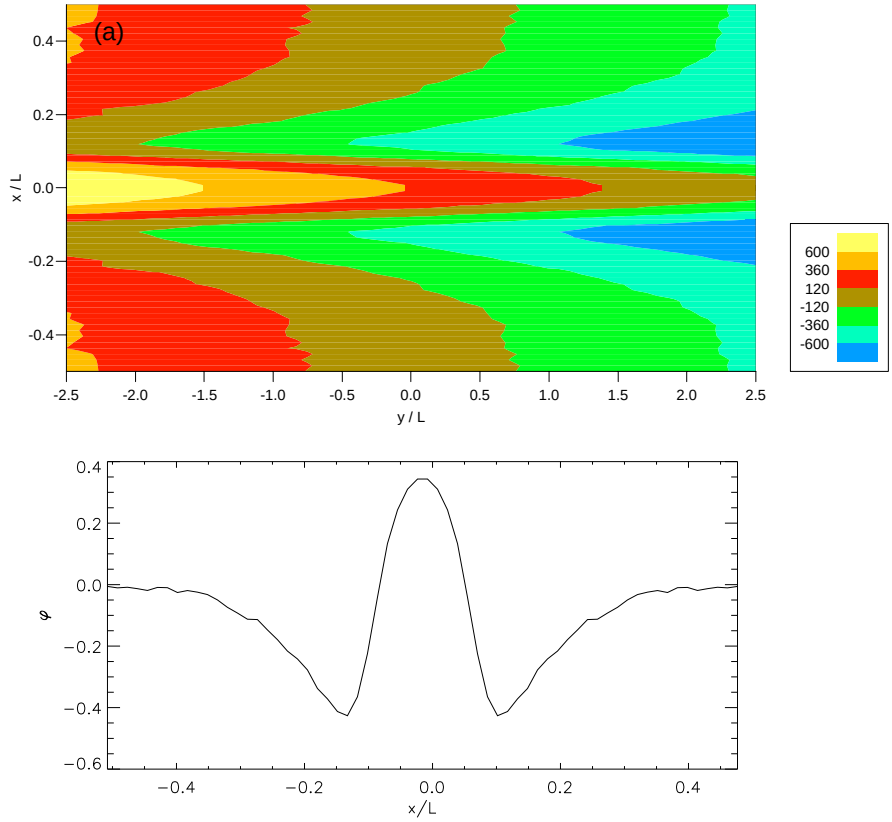

Figure 5.13: Panel (a): two dimensional contour plot of vector potential φ in the plane xy. Panel (b) : vertical profile of φ as function of coordinate x for $y = 0$.

reduced vector potential **a**, which are very small. Therefore, the new magnetic field does not vary, remaining equal to the normal component B_n. The component b_y is very small because it comes from the presence of a negligible current density along z direction. Then, the new magnetic field in the dawn-dusk direction remains zero. Finally, on the contrary, the correction b_z is not small; typical values are of the order of 0.5 B_0, where B_0 is the input magnetic field reached at the edges $x = \pm 0.5$L. It is worth to note that this correction to the input magnetic field B_{0z} is due to the electrons which modify the profile of the input current density $\partial B_{0z}/\partial x$ along y direction, providing the two off-center peaks and more profound negative wings. As a consequence, the new magnetic field along z, $B_z^{new} = B_{0z} + b_z$ display two overshoots and it is steeper in the center of the current sheet than the Harris

field B_{0z}, as shown in the panel (b) of Figure 5.12. It is important to note that it is not possible to obtain information about all of B_x, B_y and B_z if a 1D or 2D numerical model is used to describe the magnetotail configurations or dynamics, because some components of the current may not be computed. For example in Refs. [115, 95] (and the earlier study of [72]), the authors show only the self-consistent profiles of B_z, because they do not consider the other two component of the current, J_x and J_z.

5.4.1 New Electric Field

In the panel (a) of Figure 5.13, the two-dimensional contour plot of the electrostatic potential φ is depicted in the plane xy; φ displays a linear dependence on y (it comes from the y dependence on φ_0) and it depends on x through the density n, as the equation (3.35) shows. The electrostatic potential is mostly positive for negative values of y and becomes negative for positive values. In the panel (b) we show the vertical profile vs x of φ for $y = 0$. The panel (a) of the Figure 5.14 shows the x component of the new electric field E_x; this new component is due to the pressure gradient term ∇p_e along the direction normal to the current sheet. It has a quadrupole variation, but it mostly points away from the current sheet. This electric field is different from that which comes from the Hall term (due to charge separation within the ion diffusion region near a X-line): whereas the latter points towards the neutral sheet, the former points away from it. The presence of these two kinds of electric fields in the magnetotail are confirmed by Cluster crossing on August 17, 2003, that shows that an electric field due to the electron pressure tensor of the order of 1 mV/m points away from the current sheet along the direction normal to the sheet [31] (rigth-hand side of the Figure 5.14). This observation is in agreement with our numerical results which display an electric field with a peak value of the order of 15 $E_0 \sim 1.5$ mV/m. Finally, the y component of the new electric field E_y is constant (panel (b) of Figure 5.14) and it is equal to the input electric field into dawn-dusk direction E_0, while the electric z field component is equal to zero, depending on small variation of charge density with y and z coordinates.

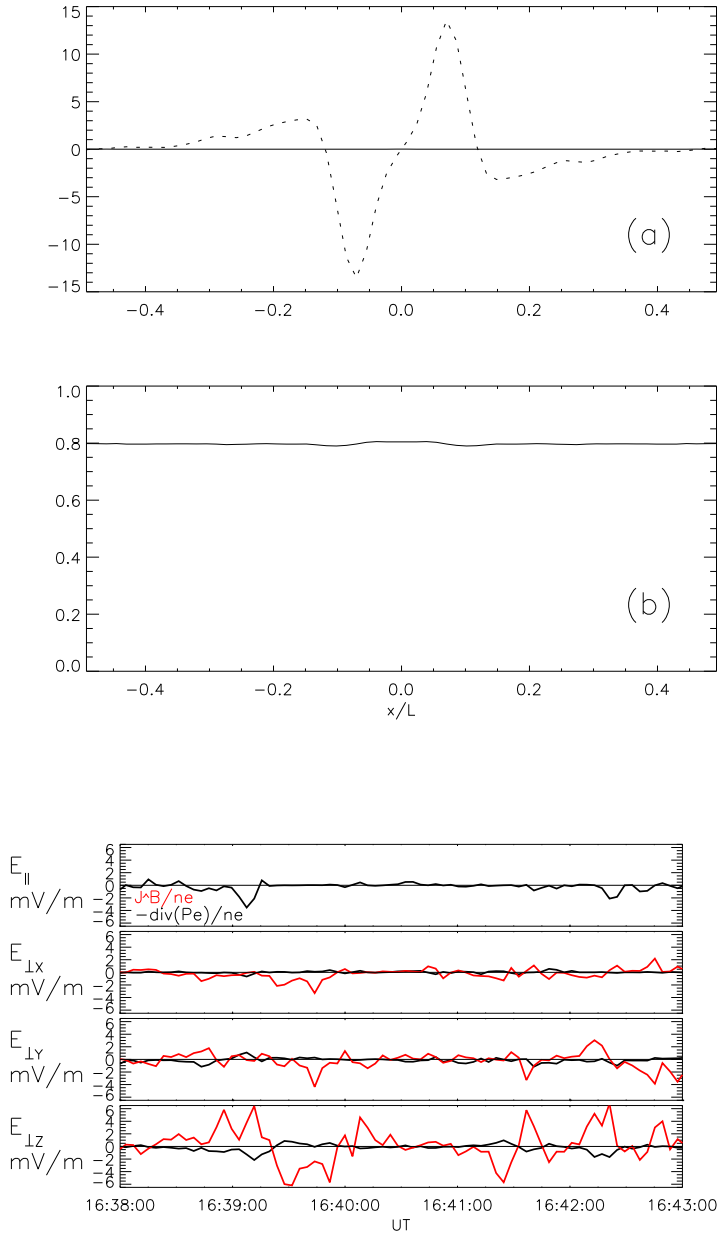

Figure 5.14: Left. Panel (a): vertical profile of electric x field component (solid line) and profile of electric z field component (short-dashed line). Panel (b): vertical profile of the y component of the elctric field $\mathbf{E}$. Electric field components are in units of E_0. Right. Electric field data of Cluster crossing on August 17, 2003. The perpendicular components of the electric field from Hall term (red line) and the electron pressure divergence (black).

5.5 Further Iterations

The numerical model that we described in the previous chapter, requires an iterative self-consistent procedure to study what is the effect of the new fields (B_z and E_x) on particles. To reach the convergence more iterations are needed, although the first iteration already shows a rapid convergence, when compared to the following iterations.

5.5.1 Numerical Investigation

We recall that our hybrid method treats the full motion of the ions, but treats the electrons as a charge-neutralizing fluid using an isothermal equation of state. The ions are initially traced through the input electric ($\mathbf{E}_0$) and magnetic ($\mathbf{B}_{0z}(x) + \mathbf{B}_n$) fields, with the resulting moments calculated on the simulation grid (64^3 points). The new fields ($\mathbf{B}^{new}$, $\mathbf{E}^{new}$) are then computed using these moments, as explained in the previous chapters, and the particles are traced through these new fields. This process should be repeated until the fields converge from one iteration to the next.

The electric field is initially set to E_0. On subsequent iterations, we calculate it by

$$\mathbf{E}^{new} = \mathbf{E}_0 + \mathbf{e} \tag{5.5}$$

with $\mathbf{e} = -\nabla\varphi$

The magnetic field on the zeroth-order iteration is given by the hyperbolic tangent with a constant normal component. On the subsequent iterations, we find the magnetic field by:

$$\mathbf{B}^{new} = \mathbf{B}_0 + \mathbf{b} \tag{5.6}$$

with $\mathbf{b} = \nabla \times \mathbf{a}$ and $\nabla^2\mathbf{a} = (\mathbf{J} - \mathbf{J}_0)$, where $\mathbf{J} = \mathbf{J}_i + \mathbf{J}_e$ and all other symbols have their usual meaning. The ion current density is computed directly from the particle distribution at each grid point. The electron current density is computed by electron bulk velocity $\mathbf{v}_e = \mathbf{v}_{\|e} + \mathbf{v}_{\perp e}$. An additional electric field in the x direction and a magnetic field correction along z arise from the zeroth-order iteration. The electrons acquire a perpendicular bulk velocity

$$v_{e\perp x} = \frac{E_y B_z}{B^2} - B_z \frac{\partial p_e}{\partial y} \frac{1}{n q_e B^2} \tag{5.7}$$

$$v_{e\perp y} = -\frac{E_x B_z}{B^2} - \left(B_n \frac{\partial p_e}{\partial z} - B_z \frac{\partial p_e}{\partial x} \right) \frac{1}{n q_e B^2} \tag{5.8}$$

$$v_{e\perp z} = -\frac{E_y B_n}{B^2} - B_n \frac{\partial p_e}{\partial y} \frac{1}{n q_e B^2} \tag{5.9}$$

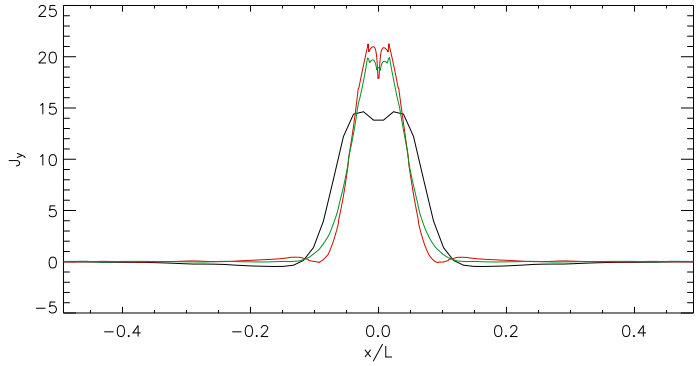

Figure 5.15: Total current density J_y in units of $cB_0/4\pi L$. Comparison of the first three iterations. The red and green curves on the graph correspond to the second and third iteration respectively, while the black curve displays the first-order solution.

caused by the changing electric and magnetic fields

$$E_x = e_x$$

and

$$B_z = B_{0z} + b_z.$$

The derivatives in the y and z directions are very small, so that they do not influence the calculation of the electron perpendicular velocity, as already seen. The new electric and magnetic fields introduce a drift term $(E_x B_z/B^2)$ in the y component of $\mathbf{v}_{e\perp}$ and modify the terms due to the pressure gradient of $\mathbf{v}_{e\perp x}$ $(B_z \partial p_e/\partial y)$ and $\mathbf{v}_{e\perp y}$ $(B_z \partial p_e/\partial x)$.

The total current density is thus used to calculate the new magnetic field correction $\mathbf{b}$ and finally the new magnetic field using the equation (5.6). To calculate the new electric field correction $\mathbf{e}$, the ion density of the first iteration is substituted again in the equation (2.32). The electrostatic potential is thus used to calculate the new electric field correction and the new electric field by the equation (5.5). This iteration procedure is then repeated until the desired convergent solution is reached. Due to the very large number of ion trajectories which we need to integrate, a single iteration takes a very long computational time, but the convergence for this method typically takes only a few iterations. We report here the first three iterative step results. The total current density along the y direction is plotted in Figure 5.15. The calculated J_y for the first, second and third iteration are indicated with black, red and green line, respectively. The two profiles determined by the

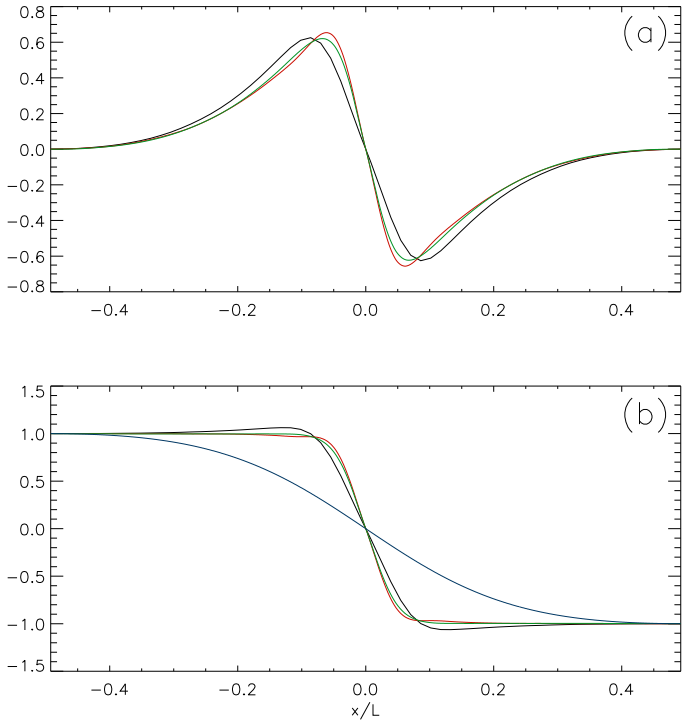

Figure 5.16: Magnetic field correction b_z in units of B_0. Comparison of the first three iterations. The red and green curves on the graph correspond to the second and third iteration respectively, while the black curve displays the first-order solution. The input (Harris) magnetic field is depicted with the blue line.

second and third iterations, are similar but not identical. These two iterations decrease the thickness of the inner current sheet with respect with the first-order iteration, and this effect is probabily due to the modified fields. It is interesting that already for the third iteration, we predict a value of current density supporting the idea that the procedure is converging. The comparison between the red and green profile indicates the existence of a stationary solution, and indicates the stability of the method. The corresponding magnetic field profiles are shown in Figure 5.16 (panels (a) and (b)). The 1st-order magnetic field correction b_z (panel (a), black line) is compared to that of the 2nd (red line) and 3rd (green line) order solutions. Note the reduction in magnitude and the spreading of the magnetic field correction. The total magnetic field B_z of the 1st-order calculation (black line), of the 2nd iteration (red line) and of the 3rd iteration (green line) are

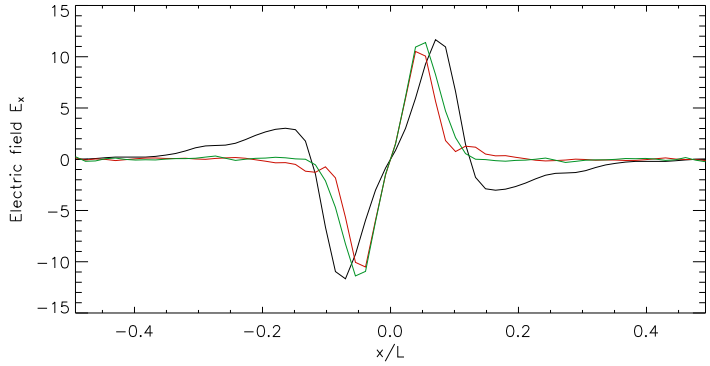

Figure 5.17: Electric field E_x in units of E_0. Comparison of the first three iterations. The red and green curves on the three consecutive graphs correspond to the second and third iteration respectively, while the black curve displays the first-order solution.

plotted on the panel (b) of the Figure 5.16. From this panel we note the less steep slope at $x = 0$ for the 1st-order case. These preliminary investigations show that, for the given number of iterations, with this self-consistent hybrid approach, it can be possibile to give a convergent value of the magnetic field correction b_z and of the total magnetic field B_z. Further iterations are performed for the electric field, too. Once this is done, E_x changes and the previous and new functions can be compared in the Figure 5.17. The process shoud continue until the results have converged, but already the first three step profiles can considered to be close enough to each other.

Summing up, to reach the exact convergence a few more iterations are needed; the first three iterations already showing a rapid convergence; it seems quite possible that a stationary solution of the studied current sheet can exist.

Chapter 6

Current Sheet Simulations in The Quiet Magnetotail

For many years kinetic studies of current sheets in space and laboratory plasmas were based on the Harris equilibrium model [30]. In particular, the Harris model was used to fit observations of the current sheet structure [59, 87, 105]. However, significant deviations from the Harris model have been reported, with the most notable effects being observed for thin current sheets, whose thickness is comparable to a few thermal ion gyroradii based on the field outside the sheet. In particular, [58, 90, 87, 77] found relatively thin current sheets with unusually large current densities, embedded in much thicker plasma sheets. On the other hand, [90] reported several cases, in which the current density, estimated from the differences between the magnetic fields measured by two spacecraft ISEE 1 and 2 had a minimum at the center of the current sheet. However, all those earlier results were based on one or at best two spacecraft observations. Therefore, they could not fully explain the mechanism of observed effects, because of the difficulties in reconstructing their spatial profile. Under which conditions and how often they are formed is still unrevealed. As a result, they left significant freedom for theoretical interpretations. For instance, [90] interpreted current splitting as an effect of the plasma anisotropy, while [39] discussed a possible model to explain the formation of the double-peaked current sheet in terms of large-scale magnetic reconnection associated with slow shocks. Everything drastically changed after the launch of four-spacecraft Cluster mission, which enabled separation of spatial and temporal effects for the first time. Even the first studies of the 2001 Cluster tail period data with spacecraft separations from 1500 to 2000 km confirmed that the spatial structure of the cross-tail current sheet is often different from the normal Harris-type sheets, i.e. the shape of the current density profile may substantially evolve with time, exhibiting double

or multiple peaks [63, 80, 81, 82, 91]. A few models attempted to explain such complicated current sheet structures that at least in some cases could not be explained either by the classical picture of collisionless reconnection or by flapping motions [91, 2]. Finding bifurcated current sheets has become a challange for theoreticians. Observations demand a significant generalization of the steady state models of current sheets, and in particular the Harris equilibrium. In the late seventies [19, 20], with a model based on a fluid theory for gyrotropic plasmas, showed that rather modest values of the plasma anisotropy should provide drastic changes in the current sheet structure. However, significant nongyrotropic effects may indeed appear in the current sheets when their thickness becomes comparable to the thermal ion gyroradius [56]. Recently, [93] presented a kinetic and nongyrotropic generalization of the theory presented in [19, 20], which interprets current splitting, taking into account the ion pressure anisotropy outside the sheet; the bifurcation of the current sheet appears in the case of small ion anisotropy with $T_{\perp i} > T_{\parallel i}$ (pancake ion distribution). Moreover, [113, 114] have developed a self-consistent model where the current sheet aging leads to the splitting of the sheet. Another mechanism has been proposed, considering magnetic turbulence [25] concentrated in a quasi-neutral sheet. A substantial level of turbulence, $\delta B/B_0 > 0.2$, where B_0 is the the magnetic field outside the sheet, is needed to have the bifurcation of the current sheet, but the level of turbulence grows with that of B_n, where B_n is the normal field component, and it is necessary to have $\delta B \sim 5B_n$ to find this effect. Other mechanisms have been also proposed, considering ion-ion kink instability [42, 43] coupling the lower-hybrid drift instability with the Kelvin-Helmoltz instability [79] or showing the formation of the bifurcated current sheet as a feature of a steady-state Vlasov model [10]. In this chapter we elaborate a new approach [23], which generalize the Harris current sheet theory, taking into account the effects of a certain number of current sheet parameters, as well as using our 3D hybrid particle code. This allow us to explain some interesting new effects in the thin magnetotail current sheets revealed by Cluster mission. The properties of the current sheet, indeed, depend on a number of parameters, including the drift velocity $v_D = (cE_y/B_0)/v_{th}$ and $b_n = B_n/B_0$, where v_{th} is the ion thermal velocity.

6.1 Parametric Study: Different B_n

Following [7], we assume, as typical values, that $v_D = 200$ km/s and $v_{th} = 170$ km/s, corresponding to a particle energy $E_K = 0.3$ keV and to an ion source anisotropy $\epsilon = 0.85$, and we varied b_n from 0.02 to 0.05.

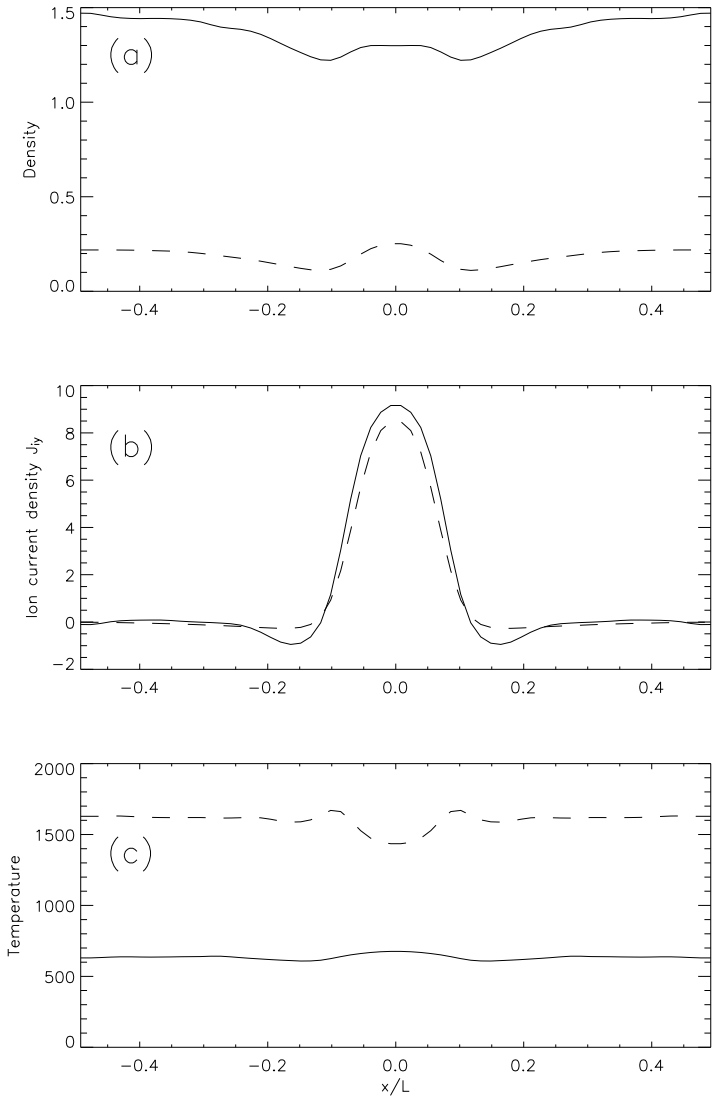

Figure 6.1: Vertical profiles of density n, ion current density J_{iy} and temperature T for $\epsilon = 0.85$ and $v_{th} = 170$ km/h. Here $b_n = 0.02$ (long dashes) and $b_n = 0.05$ (solid line). Dimensionless units. See Table 1 for the normalization.

6.1.1 Ion Moments

Figure 6.1 shows profiles of ion density n, dawn-dusk directed current density J_{iy} and temperature T, for b_n ranges between 0.02 (long dashes)-0.05 (solid line). The number density profiles are rather flat, with a small broad

maximum in the vicinity of the neutral sheet, being narrower for the smallest value of b_n.
The current density profiles are narrow and peaked near the neutral plane, where the ions are demagnetized, experiencing non adiabatic motion and cross field acceleration. This result supports the experimental observations of a thin current sheet embedded inside a more thicker current sheet. At injection, the ion Larmor radius in the asymptotic field B_0 is $r_L = 0.026$ L, so that $r_L \simeq \lambda/10$. Thus, this choice of parameters corresponds to a moderately thick current sheet [107].

With the increase of b_n from 0.02 to 0.05, we can see that the influence of the diamagnetic current (∇B drift, curvature drift and magnetizzation currents) on the final current profile in the current sheet, becomes more evident. The temperature profiles are rather flat, showing an increasing behaviour with the decrease of b_n and a characteristic kinematic effect for the smallest normal component: two small peaks off the center at about $|x| = 0.1$ L; they are due to the mixing of incoming ions, which have large velocity dispersion, with ions performing mandering orbits (see [25]).

6.1.2 Electron Moments

The increase of temperature can be expresed as a function of b_n [103]. Apart from very small values of b_n, the temperature increase scales as b_n^{-2} (see [25]). The corresponding electron contribution to the current density (J_{ey}) and the total current density are shown in Figure 6.2. The electrons are not only a neutralizing background, but their presence leads to the characteristic current sheet splitting into a double layer, as we can see from the top panel of Figure 6.2. The electron current density shows two narrow peaks at about $|x| = 0.1$ L, and a strong b_n dependence of their maximum values in the neutral plane can be seen: the peak intensity increases with the decrease of b_n. As already explained, the electron current density is computed as a function of electron velocity: $\mathbf{J_e} = nq_e\mathbf{v_e} = nq_e(\mathbf{v}_{\perp\mathbf{e}} + \mathbf{v}_{\parallel\mathbf{e}})$; J_{ey} is the sum of y component of electron perpendicular and parallel velocity , respectively. The y component of perpendicular velocity is due to x pressure gradient drift term $(B_{0z}\partial p_e/\partial x)/(nq_eB^2)$ (the z pressure gradient drift term does not contribute, being z the statistically ignorable coordinate), while y parallel velocity is null, according to our model parameters. The shape of electron current density is due to the combination of the x derivative of the electron pressure, namely of density n, and the temperature value. Being the density rather flat, J_{ey} is mostly influenced by temperature, showing an increase with the temperature increase, *i.e.* ranging b_n from 0.05 to 0.02. The total current density represents the relative ion and electron contributions to the plasma

sheet current density. The total current density profile rather concides with the ion current, showing double-humped structure due to electrons (small-scale structure), while the large-scale structure is formed by current-carrying ions (diamagnetic wings persistence). The density n used to calculate the electron current density, is the ion density obtained from the ion test particle simulation therefore, the normalization for the number density, say n_0 is, to as good extent, arbitrary. Following [25], we can fix it on the consideration that the total current has to be strong enough to reproduce the unperturbed magnetic field B_{0z} introduced in our model. In order to have the right normalizzation, electron and total current densities have to be multiplied by n_0.

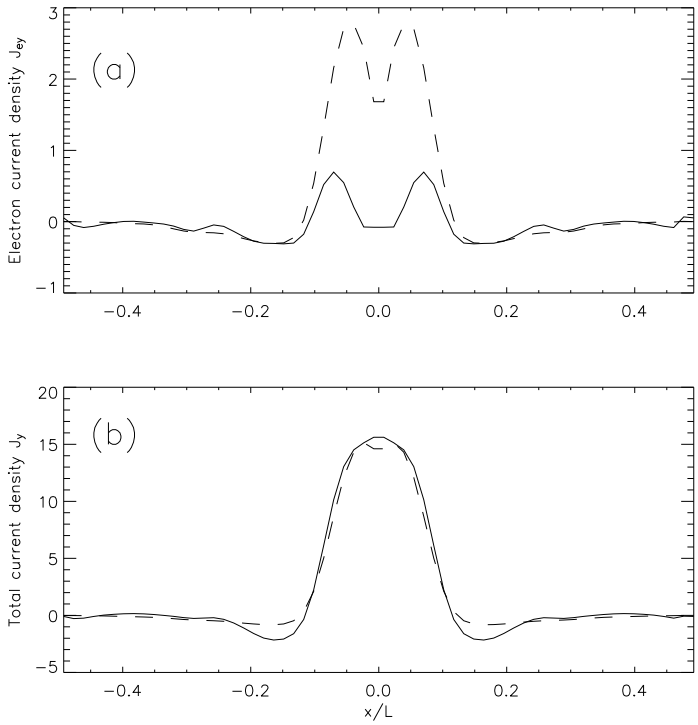

Figure 6.2: Vertical profiles of electron current density J_e in the dawn-dusk direction and total current density $\mathbf{J} = \mathbf{J}_i + \mathbf{J}_e$, for $\epsilon = 0.85$ and $v_{th} = 170$ km/h. Here $b_n = 0.02$ (long dashes) and $b_n = 0.05$ (solid line).

6.1.3 Electromagnetic Fields

The profiles of x-component of electric field E_x, the non null magnetic field correction b_z and the total magnetic field z-component B_z, are presented in Figure 6.3. All plasma parameters show the characteristic dependence only

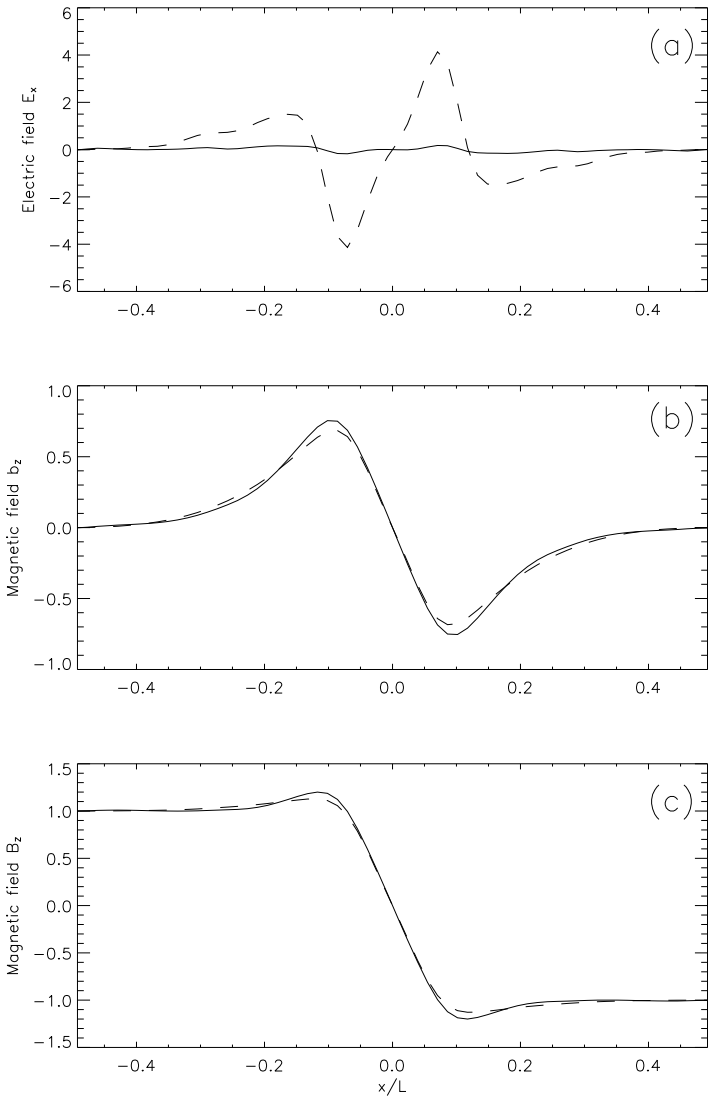

Figure 6.3: Vertical profiles of x-component of electric field E_x, magnetic field correction b_z and z-component of magnetic field B_z, for $\epsilon = 0.85$ and $v_{th} = 170$km/h. Here $b_n = 0.02$ (long dashes) and $b_n = 0.05$ (solid line).

on the x coordinate, while z is the statistically ignorable coordinate and y is the coordinate the dependence on which is usually weak. The electric field profiles show a quadrupolar behaviour, out of the neutral sheet. We interpret this situation as a quasi-neutrality condition: the ions have all the inertia and momentum, and the electrons tend to follow the ion dynamics, setting up small quadrupolar electric fields to mantain quasi-neutrality in the plasma. Indeed, the x component of the new electric field is due to the x derivative of electrostatic potential, therefore depends on the temperature value and the x derivative of the density logarithm. As already explained for the electron current density, the temperature contribution is dominant and a temperature increase causes a more intense electric field in the x direction. This effect is more important for small b_n.
The new magnetic field in y direction is due solely to magnetic field correction b_y correction, because we had not any input magnetic field along dawn-dusk direction. The z component of ion current density (not shown) is positive and it is not a drift current because the ions are not magnetized in the center of the neutral sheet ($B \sim 0$). The z component of electron current density, J_{ez}, is again given by the sum of z component of electron perpendicular and parallel velocity. The z component of perpendicular velocity is dominated by the electric drift ($\propto E_y B_n/B^2$). The z component of parallel electron velocity is the largest component of electron bulk velocity and it is dominant with respect to the perpendicular one. If we sum the ion and the electron current density they cancel each other giving a negligible total current density along z direction, then the new magnetic field in the dawn-dusk direction remains zero, $B_y = b_y \simeq 0$. The parallel velocity along z direction grows with b_n decrease and its dominant contribution to the total current sees that the total current density works in the same way.
The corresponding new magnetic $B_z = B_{0z} + b_z$ field profiles and the magnetic field correction b_z, shown in the middle and lower panel of Figure 6.3, respectively, are nearly the same. Indeed, the correction $b_z = B_{0z}/B_0$ is due to the x derivative of the total y current density (bottom panel of Figure 6.2); as the total current is little sensitive to b_n but for the appearence of double-peaks ($b_n = 0.02$) and much more pronounced diamagnetic wings ($b_n = 0.05$), the B_z profiles exhibit overshoots at about $|x| = 0.1$L, which intensity derives from diamagnetic wings deepness.

6.2 Different E_K

The next parameter that is investigated is the total injection kinetic energy $E_K = \frac{1}{2} m_i v_i^2$. In the first run, at injection the Larmor radius in the

asymptotic magnetic field B_0 is $r_L \simeq 0.064$ L, so that $r_L \simeq 3\lambda/10$, corresponding again to a moderately thick current sheet. In order to investigate more fully the ion dynamics in a thick current sheet, we make other runs decreasing the ion Larmor radius, that is decreasing the injection velocity (thermal and streaming velocity, respectively), while keeping all the other

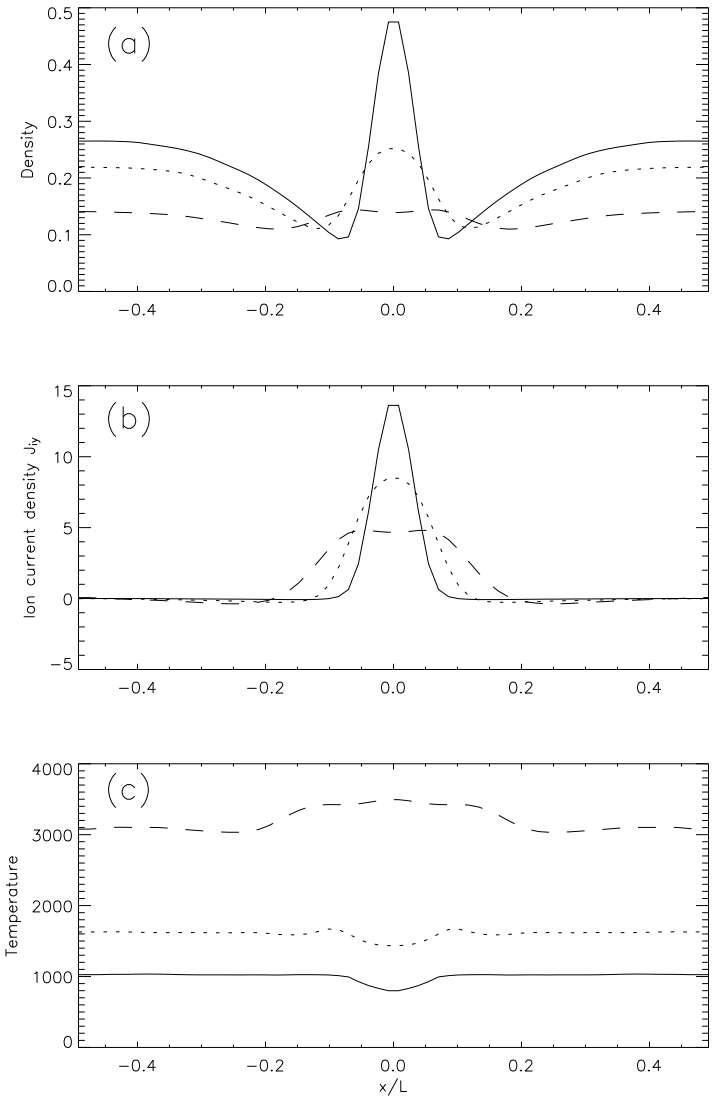

Figure 6.4: Vertical profiles of density n, ion current density J_{iy} and temperature T for $\epsilon = 0.85$ and $b_n = 0.02$. Here $v_{th} = 50$ km/s (solid line), and $v_{th} = 170$ km/s (short dashes), and $v_{th} = 400$ km/s (long dashes).

parameters the same, that is $b_n = 0.02$ and $\epsilon = 0.85$. The injection kinetic energy is varied from $E_K \simeq 690 m_i V_E^2$ (corresponding to 0.6 keV - long dashes), to $E_K \simeq 345 m_i V_E^2$ (corresponding to 0.3 keV - short dashes), and $E_K \simeq 92 m_i V_E^2$ (corresponding to 30 eV - solid line, with the typical values of the parameters). Accordingly, the ratio between the ion Larmor radius at the injection and the current sheet thickness varied as $r_L/\lambda \simeq 3/10, 1/10, 3/100$.

6.2.1 Ion Moments

The results about the ion moments are shown in Figure 6.4 and it can be seen that the ion number density and ion current density decrease with the increase of the injection velocity and there is no current splitting, in each of the studied runs. Decreasing the thermal velocity means reducing the ion Larmor radius, forcing the ions in a narrow region in the very center of the current sheet. Moreover, as v_{th} diminishes, the injection energy rate and the temperature increase.

6.2.2 Electron Moments

We checked whether the current splitting is consistent with the structure of the electron moments, showing electron current density and the effect on total current density in Figure 6.5. The electron current density profiles show a splitting into a double layer that is more evident for higher injection velocity and this introduces a splitting into the total current density. The current splitting persists for each injection velocity and for each current sheet thickness. This shows once more that the double current sheet is due to the electron dynamics and not to the thinness of the current layer. Moreover, we can see that the maximum of electron current in the center of the current sheet varies in an inverse proportion to the value of ion injection thermal velocity. As already explained, the electron current depends on temperature value (or v_{th} values) and pressure gradient (*i.e.* density gradient). The vertical profiles of ion density show larger variations for smaller v_{th}, which determine electron and total current dependence on ion injection thermal verlocity: $\mathbf{J}_e$ and $\mathbf{J}$ increase as v_{th} decreases. As for ions, the electrons, experiencing a Larmor radius decreasing, describe a narrowing of the current sheet.

6.2.3 Electromagnetic Fields

The corresponding electric and magnetic field components are shown in Figure 6.6. The x electric field component decreases with v_{th} decreasing and

a reletive maximum and minimum profile shift around $|x| \simeq 0.1$ L to the neutral sheet crossing is noted. The density variations affect the electric field intensity and its dependence on v_{th}. Even with this new set of parameters, the total current density along z direction is negligible giving a negligible new magnetic field along y direction. By the same analysis made above for the total current density along y direction, we explain the shape of the total B_z magnetic field. The magnetic overshoots are more pronounced for larger v_{th}. Indeed, the profiles of the total current density along y direction show more pronunced diamagnetic wings for bigger v_{th}. The peak-values of these currents characterize a substantial steepness near the neutral plane and the more the thermal velocity increases, the less the steepness is evident.

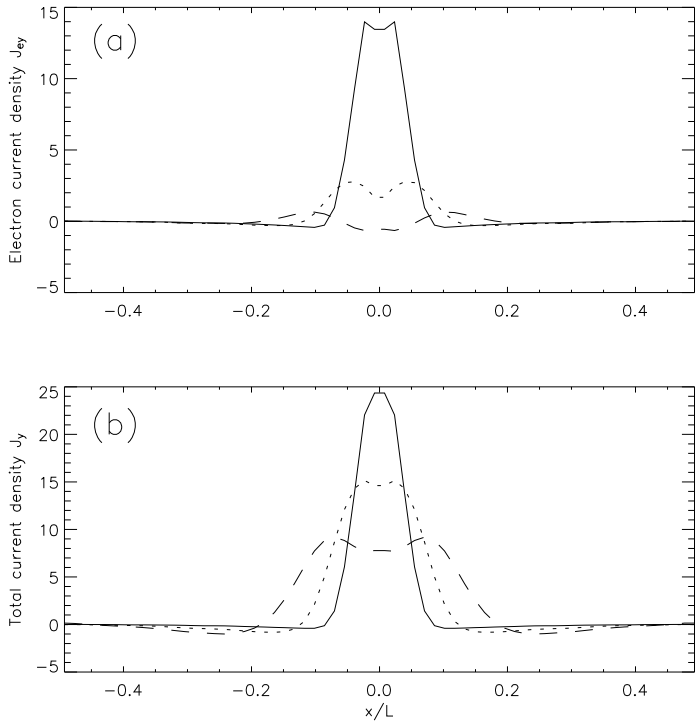

Figure 6.5: Vertical profiles of electron current density J_e in the dawn-dusk direction and total current density $\mathbf{J} = \mathbf{J}_i + \mathbf{J}_e$, for $\epsilon = 0.85$ and $b_n = 0.02$. Here $v_{th} = 50$ km/s (solid line), and $v_{th} = 170$ km/s (short dashes), and $v_{th} = 400$ km/s (long dashes).

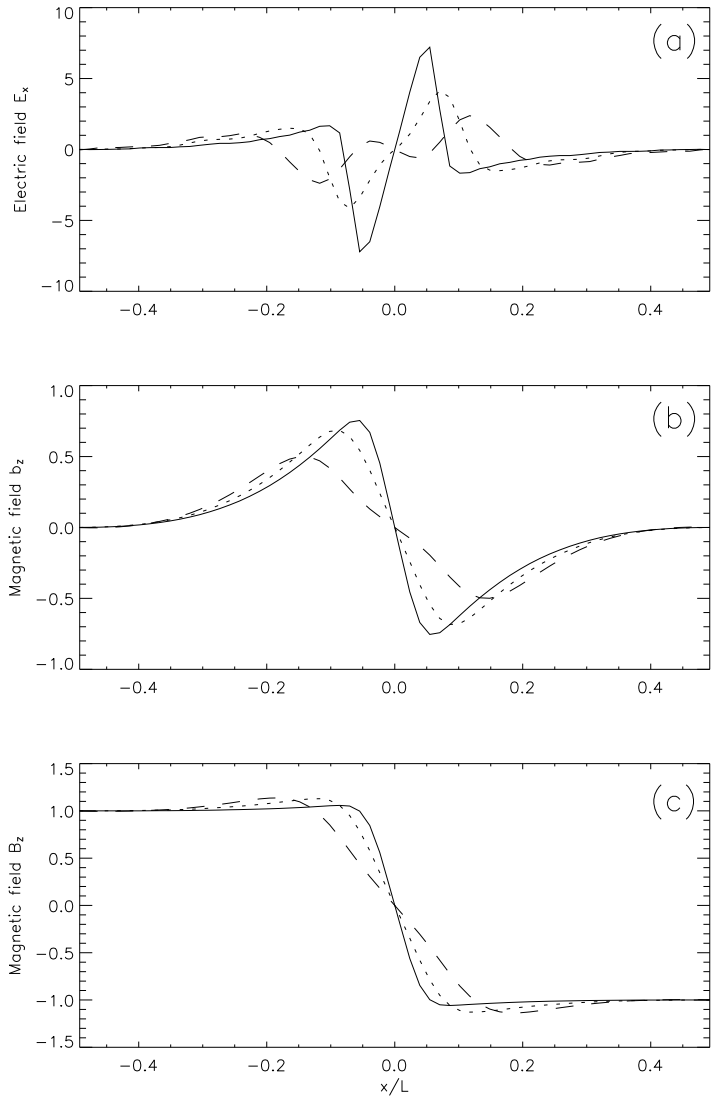

Figure 6.6: Vertical profiles of x-component of electric field E_x, magnetic field correction b_z and z-component of magnetic field B_z, for $\epsilon = 0.85$ and $b_n = 0.02$. Here $v_{th} = 50$ km/s (solid line), and $v_{th} = 170$ km/s (short dashes), and $v_{th} = 400$ km/s (long dashes).

6.3 Different ϵ

Finally the influence of varying the ion anisotropy is explored.

6.3.1 Ion Moments

In Figure 6.7 the vertical profiles of ion density n, current density in the dawn-dusk direction J_{iy} and the temperaure T are shown for $b_n = 0.02$ and different values of the ion source anisotropy. In the first run $\epsilon = 2$, which corresponds

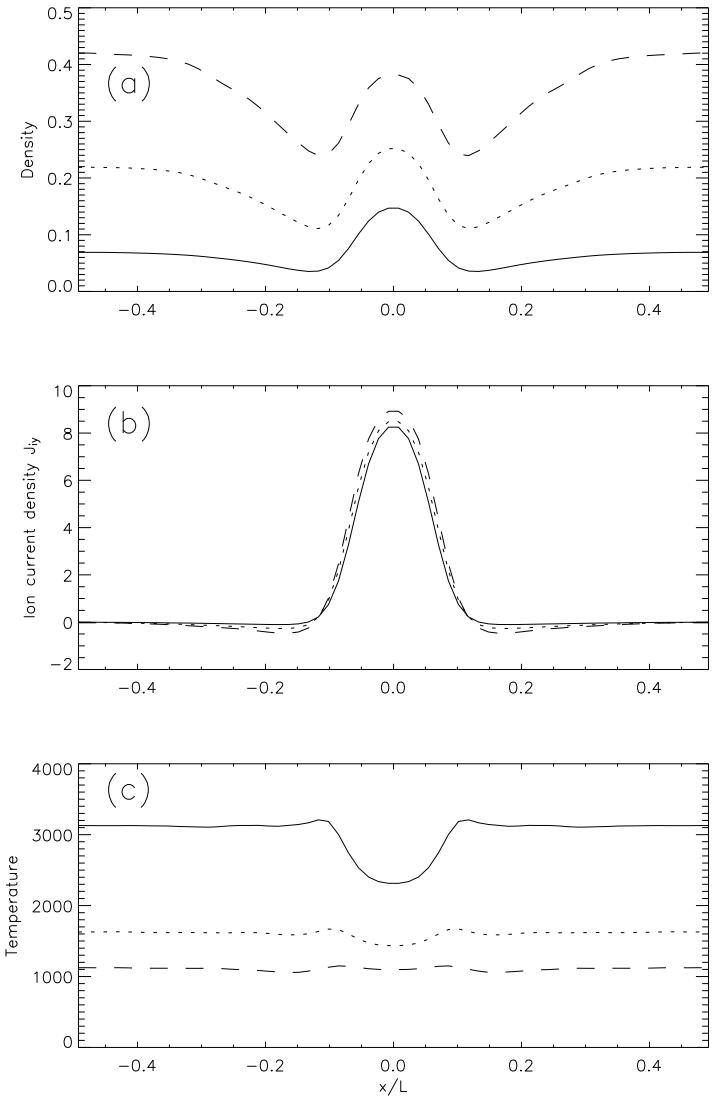

Figure 6.7: Vertical profiles of density n, ion current density J_{iy} and temperature T for for $v_{th} = 170$ km/s and $b_n = 0.02$. Here $\epsilon = 0.3$ (solid line), $\epsilon = 0.85$ (short dashes), and $\epsilon = 2$ (long dashes).

to an high anisotropy, whereas a small anisotropy value corresponds to an high streaming velocity u. The density grows with ϵ, remaining roughly the same, as a function of x, showing a small peaked profile and small variations. A bell-shaped current density profile is obtained and the peak value is higher for bigger ϵ. The temperature profiles (in the bottom panel of Figure 6.7) are rather flat, except for $\epsilon = 0.3$, and the temperature appears to increase with the decrease of ϵ. In particular, as the anisotropy decreasing is obtained fixing the thermal velocity ($v_{th} = 170$ km/s), varying the streaming velocity from 85 km/s, 200 km/s to 510 km/s, ϵ decreasing corresponds to a current sheet heating and to the temperature increasing.

6.3.2 Electron Moments

It appears (Figure 6.8) that the presence of electrons has a strong influence on the global current sheet dynamics, causes the double humped profiles of

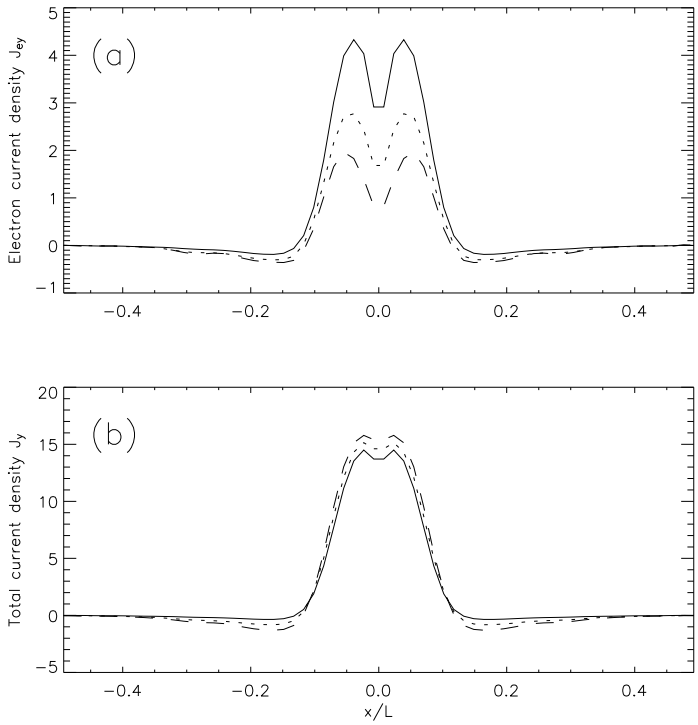

Figure 6.8: Vertical profiles of electron current density J_e in the dawn-dusk direction and total current density $\mathbf{J} = \mathbf{J}_i + \mathbf{J}_e$, $v_{th} = 170$ km/s and $b_n = 0.02$. Here $\epsilon = 0.3$ (solid line), $\epsilon = 0.85$ (short dashes), and $\epsilon = 2$ (long dashes).

the current as in the previous cases. The peak amplitude of electron current density is directly proportional to the decreasing anisotropy and this is due to a dominant effect of the temperature with respect to the pressure gradient.

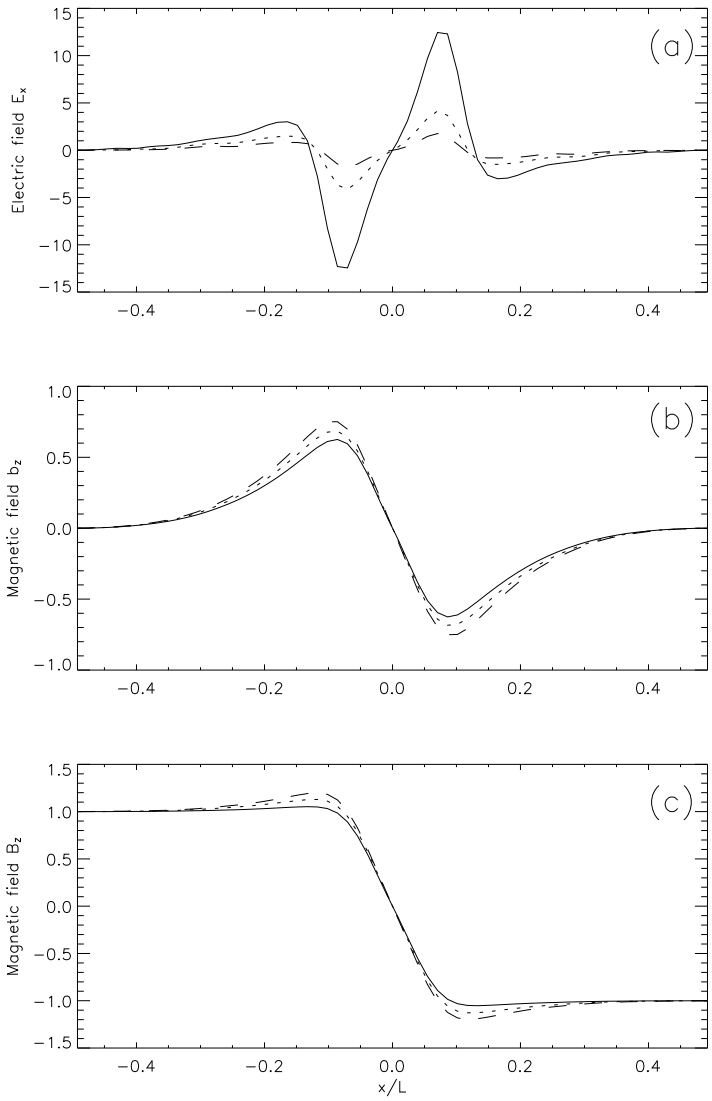

Figure 6.9: Vertical profiles of x-component of electric field E_x, magnetic field correction b_z and z-component of magnetic field B_z, for $v_{th} = 170$ km/s and $b_n = 0.02$. Here $\epsilon = 0.3$ (solid line), $\epsilon = 0.85$ (short dashes), and $\epsilon = 2$ (long dashes).

6.3.3 Electromagnetic Fields

The anisotropy dependence of magnetic field results in a decrease of b_y with anisotropy for $|x| < 0.1$ L. However, in the vicinity of neutral sheet, b_y increases with ϵ increasing. The bottom panel of Figure 6.9 shows the total z magnetic field profiles computed for different anisotropy levels; the diamagnetic currents are deeper for higher ϵ , then the magnetic overshoots increase with anisotropy and the profile of magnetic field converges to the injection limiting profile (compare to similar results of of [116]). As already observed in the case of different b_n, the same order-like peak-value of the total current density affects the behaviour of B_z, showing the same steepness in the very center of the current sheet. On the top panel of Figure 6.9, we present the electric field structure. The quadrupolar shape grows with anisotropy and it is more evident for bigger ϵ. Here the temperature effect is again stronger than the density gradient. Moreover, the density term in the equation 2.32 becomes more negative for small values of n/n_0, explaining the electric field variation with anisotropy.

Chapter 7

Summary and Discussion

We have motivated the need for and the usefulness of a hybrid plasma description in which ion kinetics are retained and the electrons are represented as a massless fluid. The details of a 3D hybrid code to study the equilibrium structure of the magnetotail have been discussed, and test problems have been illustrated. Predictions from this hybrid model have been compared with the observations in the magnetotail, which are currently available due to Geotail and Cluster missions. The result of hybrid simulation have demonstrated that the dominant contribution in the cross-tail current density comes from ions, but the electrons are responsible for the current bifurcation and also tripled structure of the current sheets. Moreover, it was shown that the current bifurcation effect could be explained by the pressure gradient term. The results recently provided by the Cluster spacecraft show typical scales and peak values of the bifurcated structures very close to those obtained from the numerical simulation. Further, for certain parameters of the magnetotail configuration, as the normal component of the magnetic field and ion injection energy and anisotropy, we obtain a triple peak in the total current density profile due, once again, to electrons. There is a single observation of a triple peaked structure up to now [64], and it is very interesting that our code can reproduce this observation.
Another implication of the electron dynamics is that the x component of the magnetic field is modified showing two overshoots and a steeper behaviour in the center of the current sheet than the Harris field profile. The magnetic overshoots are frequently found in the observations, too.
The effect of the electron dynamics correspond also to a different electric field structure inside the current sheet: whereas we find a constant electric field along y direction equal to the input one, a perpendicular electric field appears. This new component is due to the pressure gradient term ∇p_e along the direction normal to the current sheet. The presence of this electric field

in the magnetotail is confirmed by Cluster crossing on August 17, 2003, that shows that an electric field due to the electron pressure tensor of the order of 1 mV/m points away from the current sheet along the direction normal to the sheet [31]. This observation is in agreement with our numerical results which display an electric field with a peak value of the order of 15 E_0 corresponding to 1.2 mV/m. We can conclude from our study that a self-consistent structure of the current sheet should require the presence of an electrostatic potential and a magnetic field different from the Harris model [10, 95].
To study what is the effect of these new fields (B_z and E_x) on particles, a few iterations are needed. Convergence typically takes only three iterations. This indicates the existence of a stationary solution and guarantees the stability of the numerical method.

We have also studied by hybrid simulations the current sheet for the parameters typical of the plasma sheet which correspond to the near-Earth magnetotail, including the drift velocity $v_D = (cE_y/B_0)/v_{th}$ and the normal magnetic field $b_n = B_n/B_0$. It is found that there exists solutions of 3D current sheet configuration which are sensitive to the normal magnetic field component b_n, ion injection kinetic energy E_K and ion anisotropy ϵ at injection. The model presented here may be applied to explain some features of the current sheets observed in the magnetotail plasma layer. It is emphasized that the amplitude of current and plasma densities as well as of electric and magnetic fields profiles depends on the above mentioned parameters. The density decreases with the decrease in the normal magnetic field component, as the ion and total current density. The electron current density shows a double-humped profile with two peaks which are more narrow, with a larger intensity, for small b_n than for higher b_n; this effect leads to the current sheet splitting into a bifurcated structure for the smallest b_n value. In this case, E_x field profile decreases with b_n. Then, the magnetic z field component is quite insensitive to b_n changing, indeed the two profiles roughly coincide.
We have undertaken the parametric study of current sheet structure for different values of ion kinetic energy E_K. It is seen that as the thermal velocity increases (*i.e.* the Larmor radius increases) the amplitute of the densities decreases and their width increases. The temperature profile is roughly flattened increasing in a direct proportion to the value of ion thermal velocity. The ion current density exhibits a bell-shaped profile, it has a narrow sharp peak in the very center of the sheet which becomes much broader in the cases of higher thermal velocity, so that the bifurcated profile of current sheet is due to electrons once again. The electric and magnetic field components increase mostly with the decrease of thermal velocity except for a very small regions ($|x| < 0.1$ L) in B_z profile. The magnetic overshoots are more pro-

nounced for larger v_{th} and this is due to the diamagnetic wings in the total current density profiles, whose intensity affects the magnetic field steepness in the center of the current sheet: the more the thermal velocity increases, the less the steepness is evident. Finally we have shown the variation of typical current sheet features with the ion source anisotropy. Here, we observe that number and current density increase with ϵ. On the other hand, electron current density decreases showing, in all cases, a bifurcated structure which supports the current sheet bifurcation. The total current density shows diamagnetic wings sensitive to anisotropy growth whose intensity affects B_z, *i.e.* the magnetic overshoots appear explicitly in its profiles and the variation of overshoot amplitudes with increasing anisotropy is observed, as shown on the curves.

Our study shows that a variety of different equilibria could be obtained by varying the input parameters, something which is similar to the solutions of the Grad-Shafranov equations, which depend on the arbitrary functions of the magnetic surface. In this connection, we point out that the Harris equilibrium, appealing as it may be, is by no way the only possible equilibrium, but just one for which a complete analytical solution is possible. Indeed, a wider class of Vlasov equilibria has been investigated [114, 93]. Here we show that further configurations can be obtained by varying the parameters of our hybrid code.

Bibliography

[1] Alfven, H., Cosmic plasma (D. Reidel, Dordrecht), (1981)

[2] Arzner, K., Scholer, M., Kinetic structure of the post plasmoid plasma sheet during magnetotail reconnection, *J. Geophys. Res.*, **106**, 3827, (2001)

[3] Asano, Y., Mukai, T., Hoshino, M., Saito, Y., Hayakawa, H., Nagai, T., Evolution of the thin current sheet in a substorm observed by Geotail, *J. Geophys. Res.*, **118**, A5, 1189, (2003)

[4] Asano, Y., Mukai, T., Hoshino, M., Saito, Y., Hayakawa, H., Nagai, T., Current sheet structure around the near-Earth neutral line observed by Geotail, *J. Geophys. Res.*, **109**, A02212, (2004)

[5] Asano, Y., Mukai, T., Hoshino, M., Saito, Y., Hayakawa, H., Nagai, T., Statistical study of thin current sheet evolution around substorm onset, *J. Geophys. Res.*, **109**, A05213, (2004)

[6] Asano, Y., Nakamura, R., Baumjohann, W., Runov, A., V*ö*r*ö*s, Z., Volker, M., Zhang, T. L., Balogh, A., Klecker, B., R*é*me, H., How typical are atypical current sheets?, *Geophys. Res. Lett.*, **32**, (2005)

[7] Ashour-Abdalla, M., Zelenyi, L. M., Peroomian, V., Richard, R., Consequences of magnetotail ion dynamics, *J. Geophys. Res.*, **99**, 14 891, (1994)

[8] Ashour-Abdalla, M., Frank, L. M., Paterson, W. R., Peroomian, V., Zelenyi, L. M., Proton velocity distributions in the magnetotail: Theory and observations, *J. Geophys. Res.*, **101**, 2587, (1996)

[9] Baumjohann, W., Paschmann, G., Cattell, C. A., Average plasma properties in the central plasma sheet, *J. Geophys. Res.*, **94**, 6597, (1989)

[10] Birn, J., Schindler, K., and Hesse, M.: Thin electron current sheets and their relation to auroral potentials, *J. Geophys. Res.*, **109**, A02217, (2004)

[11] Borovsky, J. E., Elphic, R. C., Funsten, H. O., Thomsen, M. F., The Earth's plasma sheet as a laboratory for flow turbulence in high-β MHD, *J. Plasma Phys.*, **57**, 1, (1997)

[12] Brandt, J., Introduction to the Solar Wind, W. H. Freeman, New York, (1970)

[13] Brochu, T., Semi-Lagrangian Time Integration, Course Project CPSC542b (Level Set Methods), 2004-2005

[14] Burkhart, G. R., Dusenbery, P. B., Speiser, T. W., Lopez, R. E., Hybrid simulation of thin current sheets, *J. Geophys. Res. A*, **98**, A12, 21373, (1993)

[15] Byers, J. A., Cohen, B. I., Condit, W. C., Hanson, J. D., Hybrid simulation of quasi-neutral phenomena in magnetized plasma, *J. Comp. Phys.*, **27**, 3, 363, (1978)

[16] Camporeale, E., Lapenta, G., Model of bifurcated current sheets in the Earth's mahnetotail: Equilibrium and stability, *J. Geophys. Res.*, **110**, A07206, (2005)

[17] Cargill, P. J., Chen, J., Harold, J. B., One-dimensional hybrid simulations of current sheets in the quiet magnetotail, *Geophys. Res. Lett.*, **21**, 20, 2251, (1994)

[18] Coroniti, F. V., Kennel, C. F., Changes in magnetospheric configuration during substorm growth phase, *J. Geophys. Res.*, **77**, 3361-3370, (1972)

[19] Cowley, S. W. H., The effect of pressure anisotropy on the equilibrium structure of magnetic current sheets, *Planet. Space Sci.*, **26**, 1037, (1978)

[20] Cowley, S. W. H., On the distribution of B_y in the geomagnetic tail, *Planet. Space Sci.*, **27**, 769, (1979)

[21] Daughton, W., G. Lapenta, and P. Ricci, Nonlinear evolution of the lower-hybrid drift instability in a current sheet, *Phys. Rev. Lett.*, **93**, 105004, (2004)

[22] De Bartolo, R., Greco, A., Veltri, P., Pommois, P.,A three-dimensional hybrid code to model the particle dynamics in the magnetotail current sheet, in preparation, (2006)

[23] De Bartolo, R., Greco, A., Zimbardo, G., Veltri, P., Three-dimensional hybrid simulations of current sheets in the near magnetotail: parametric analysis , in preparation, (2006)

[24] Genot, V., Mottez, F., Fruit, G., Louarn, P., Sauvaud, J. A., Balogh, A., Bifurcated current sheet: Model and Cluster observations, *Planet. Space Sci.*, **53**, 229, (2005)

[25] Greco, A., Taktakishvili, A. L., Zimbardo, G., Veltri, P., Zelenyi, L. M., Ion dynamics in the near-Earth magnetotail: Magnetic turbulence versus normal component of the average magnetic field, *J. Geophys. Res.*, **107**, 1267, (2002)

[26] Greco, A., De Bartolo, R., Zimbardo, G., Veltri, P., A three-dimensional hybrid code to study the magnetotail configuration: the role of electrons in the formation of the double peak current sheet, in press, (2006)

[27] Gringauz, K. I., Some results of experiments in interplanetary space by means of charged particle traps on Soviet space probes, in Space Research, edited by H. C. van der Hulst, North Holland, Amsterdam, (1961)

[28] Harned, D. S., Quasi-neutral hybrid simulation of macroscopic plasma phenomena, *J. Comp. Phys.*, **47**, 452, (1982)

[29] Harold, J. B., Chen, J., Kinetic thinning in one-dimensional self-consistent current sheets, *J. Geophys. Res.*, **101**, 24 899, (1996)

[30] Harris, E.G., The equilibrium of oppositely directed magnetic fields, *Nuovo Cimento*, **23**, 115, (1962)

[31] Henderson, P. D., Owen, C. J., Lahiff, A. D., Fazakerley, A. N., Cluster PEACE observations of electron pressure tensor divergence in the magnetotail, in preparation, (2006)

[32] Hesse, M., Winske, D., Hybrid simulations of collisionless ion tearing, *Geophys. Res. Lett.*, **20**, 1207-1210, (1993)

[33] Hesse, M., Winske, D., Hybrid simulations of collisionless reconnection in current sheets, *J. Geophys. Res.*, **99**, 11 177-11 192, (1994)

[34] Hesse, M., Winske, D., Kuznetsova, M. M., Hybrid modeling of collisionless reconnection in two-dimensional current sheets: Simulations, *J. Geophys. Res.*, **100**, A11, pp. 21 815-21 825, (1995)

[35] Hesse, M., Winske, D., Kuznetsova, M.M., Birn, M., Schindler, K., Hybrid modeling of the formation of thin current sheet in magnetotail configurations, *J. Geomag. Geoelectr.*, **48**, 5-6, 749-763 (1996)

[36] Hesse, M., Winske, D., Birn, M., On the ion scale structure of thin current sheet in the magnetotail, *Phys. Scripta T*, **T-74**, 63, (1998)

[37] Hill, T. W., Voigt, G. H., Limits on plasma anisotropy in a tail-like magnetic field, *Geophys. Res. Lett.*, **12**, 2441, (1992)

[38] Holland, D., Chen, J., Self consistent current sheet structures in the quiet-time magnetotail, *Geophys. Res. Lett.*, **20**, 17, 1775, (1993)

[39] Hoshino, M., Nishida, A., Mukai, T., Saito, Y., Yamamoto, T., Kokubun, S., Structure of plasma sheet in magnetotail: Double-peaked electric current sheet, *J. Geophys. Res.*, **101**, 24 775-24 786, (1996)

[40] Hundhausen, A. J., Coronal Expansion and Solar Wind, Springer, New York, (1972)

[41] Israelevich, P. L., Ershkovich, A. I., Bifurcation of Jovian magnetotail current sheet, *Ann. Geophys.*, **24**, 1479-1481, (2006)

[42] Karimabadi, H., Daughton, P., Pritchett, L. , and Krauss-Varban, D.: Ion-ion kink instability in the magnetotail: 1. Linear theory, *J. Geophys. Res.*, **108**, A11, 1400, (2003a)

[43] Karimabadi, H., Pritchett, L. , Daughton, P., and Krauss-Varban, D.: Ion-ion kink instability in the magnetotail: 2. Three-dimensional full particle and hybrid simulations and comparison with observations, *J. Geophys. Res.*, **108**, A11, 1401, (2003b)

[44] Karimabadi, H., Krauss-Verban, D., Huba, J. D., Vu, H. X., On magnetic reconnection regimes and associated three-dimensional asymmetries: hybrid, Hall-less hybrid and Hall-MHD simulations, *J. Geophys. Res.*, **109**, A09205, (2004)

[45] Klimontovich, Yu. L., The statistical theory of non-equilibrium processes in a plasma, MIT Press, Cambridge, Mass (1967)

[46] Krauss-Varban, D., Omidi, N., Large-scale hybrid simulations of the magnetotail during reconnection, *Geophys. Res. Lett.*, **22**, 3271-3274, (1995)

[47] Krauss-Varban, D., From theorethical foundation to invaluable research tool: modern hybrid simulations, *Proceedings of ISSS-7*, 26-31 March, 2005, 15-18, (2005)

[48] Kuznetsova, M. M., Hesse, M., Winske, D., Hybrid modelling of collisionless tearing mode: Linear theory, *J. Geophys. Res. A*, **100**, 21 827-21 833 (1995)

[49] Kuznetsova, M. M., Hesse, M., Winske, D., Ion dynamics in a hybrid simulation of magnetotail reconnection, *J. Geophys. Res.*, **101**, A12, pp. 27,351-27,374, (1996)

[50] Kuznetsova, M.M., Hesse, M., Winske, D., Kinetic quasi-viscous and bulk inertia effects in collisionless magnetotail reconnection, *J. Geophys. Res.*, **103**, A1, 199-213, (1998)

[51] Lee, L. C., Zhang, L., Yan, M., Cai, H. J., Choe, G. S., Otto, A., Akasofu, S. I., Formation of a very thin current sheet during substrom growth phase and plasma dynamics in the recovery phase, in: Eds. J.R Kan, J. D. Carven and S. I. Akasofu, 143-148, Proc. of the second Int. Conf. on Substorms, Fairbanks, Alaska, (1994)

[52] Lin, Y., Lee, L. C., Structure of reconnection layers in the magnetopause, *Space Sci. Rev.*, **65**, 59-179, (1994)

[53] Lin, Y., Swift, D. W., A two-dimensional hybrid simulation of the magnetotail reconnection layers, *J. Geophys. Res.*, **101**, A9, pp. 19,859-19,870, (1996)

[54] Lipatov, A. S., Hybrid codes with finite electron mass, *Prceedings of ISSS-6*, 1-4, Copernicus Gesellschaft, (2001)

[55] Lottermoser, R. F., Scholer, M., Matthews, A. P., Ion kinetic effects in magnetic reconnection: Hybrid simulations, *J. Geophys. Res.*, **103**, A3, pp. 4547-4560, (1998)

[56] Lui, A. T. Y., Anderson, B. J., Takahashi, K., Zanetti, L. J., McEntire, R. W., Potemra, T. A., Lopez, R. E., Current Disruptions in the Near-Earth Neutral Sheet Region, *J. Geophys. Res.*, **97**, 1461, (1992)

[57] Matthews, A. P., Current advance method and cyclic leapfrog for 2D multispecies Hybrid plasma simulations, *J. Comp. Phys.*, **112**, 102, (1994)

[58] McComas, D. J., Russell, C. T., Elphic, R. C., Barne, S, J., The near-Earth cross-tail current sheet: Detailed ISEE 1 and 2 case studies, *J. Geophys. Res.*, **91**, 4287, (1986)

[59] McPherron, R. L., Nishida, A., Russell, C. T., Is near-Earth current sheet thinning the cause of auroral substorm onset?, Quantitative Modeling of Magnetosphere-Ionosphere Coupling Processes, edited by Kamide Y. and Wolf R. A., 252-265, Kyoto Sangyo University, Kyoto, Japan, (1987)

[60] Malova, H. V., Sitnov, M. I., Zelenyi, L. M., Sharma, A. S., Self-consistent model of 1-D current sheet: the role of drift, magnetization and diamagnetic currents, AGU Monograph Series, *Magnetospheric Current Systems*, **118**, 313-322, (2000)

[61] Nakabayashi, J., Machida, S., Electromagnetic hybrid-code simulation of magnetic reconnection: Velocity distribution functions of accelerated ions, *Geophys. Res. Lett.*, **24**, 11, 1339, (1997)

[62] Nakamura, M. S., Fujimoto M., Maezawa, K., Ion dynamics and resultant velocity space distributions in the course of magnetic reconnection, *J. Geophys. Res.*, **103**, A3, pp. 4531-4546, (1998)

[63] Nakamura, R. , Baumjohann, W., Runov, A., Volwerk, M., Zhang, T. L., Klecker, B., Bogdanova, Y., Roux, A., Balogh, A., Réme, H., Sauvaud, J. A., Frey, H. U., Fast flow during current sheet thinning, *Geophys. Res. Lett.*, **29**, 23, 2140, (2002)

[64] Nakamura, R. , Baumjohann, W., Runov, A., Asano, Y., Balogh, A., R'eme, H., Thin current sheet measured by Cluster at 200 km tetrahedron scale, paper presented at second Workshop on Thin current Sheets, College Park, Md. (available at http://www.glue.umd.edu/ sitnov/TCS/tcs_1_files/online.html)

[65] Ness, N. F., Magnetotail research: the early years, pp. 11-20 in Magnetotail Physics, edited by A.T.Y. Lui, The Johns Hopkins University Press, (1987)

[66] Neugebauer, M., and Snyder, C. W.,The Mission of Mariner 2: Preliminary observations, solar plasma experiment, *Science*, **138**, 1095, (1962)

[67] Nötzel, A., Schindler, K., Birn, J., On the cause of approximate pressure isotropy in the quiet near-Earth plasma sheet, *J. Geophys. Res.*, **90**, 8293, (1985)

[68] Omelchenko, Y. A., Karimabadi, H., Event-driven, hybrid particle-in-cell simulation: A new paradigm for multi-scale plasma modeling, *J. Comp. Phys.*, in press, (2006)

[69] Omidi, N., Karimabadi, H., Quest, K. B., Global hybrid simulations of solar wind interaction with the magnetosphere, *Proceedings of ISSS-6*, Copernicus Gesellschaft, 1-2, (2001)

[70] Parker, E. N., Dynamics of interplanetary gas and magnetic fields, *Astrophys. J.*, **128**, 664-676, (1958)

[71] Parker, E.N., Interplanetary Dynamical Processes, (New York: Wiley-Interscience), (1963)

[72] Peroomian, V., Zelenyi, L. M, Schriver, D., Imprints of small-scale nonadiabatic particle dynamics on large-scale properties of dynamical magnetotail equilibria, *Adv. Space Res.*, **12**, 2657, (2002)

[73] Pizzo, V.J., Goldstein, B.E., Meridional transport of magnetic flux in the solar wind between 1 AU and 10 AU: A theoretical analysis, *J. Geophys. Res.*, **92**, 7241, (1987)

[74] Pommois, P., Gaussian and anomalous magnetic field line transport in anisotropic 3D turbulence: application to solar wind, Ph.D thesis, University of Calabria, Italy (1997)

[75] Pritchett, P. L., Coroniti, F. V., A radiating one-dimensional current sheet configuration, *J. Geophys. Res. A*, **98**, A9, 15355, (1993)

[76] Pritchett, P. L., Coroniti, F. V., Convection and formation of thin current sheets in the near-Earth plasma sheet, *Geophys. Res. Lett.*, **21**, 1587, (1994)

[77] Pulkkinen, T. I., Baker, L. L., Cogger, L. L., Frank, L. A., Sigwarth, J. B., Kokubun, S., Mukai, T., Singer, H. J., Slavin, J. A., Zelenyi, L. M., Spatial extent and dynamics of a thin current sheet during the

substorm growth phase on december 10, 1996, *J. Geophys. Res.*, **104**, 28 475, (1999)

[78] Quest, K. B.: Hybrid Simulation, in Tutorial Course: Third International School for Space Simulation, edited by B. Lembege and J. W. Eastwood, pp. 177, Cepadues Ed., Toulouse, France, (1989)

[79] Ricci, P., Lapenta, G., and Brackbill, J. U.: Structure of the magnetotail current. Kinetic simulation and comparison with the satellite observations, *Geophys. Res. Lett.*, **31**, L06801, (2004)

[80] Runov, A., Nakamura, R., Baumjohann, W. , Zhang, T. L., Volwerk, M. ,Eichenberg, H. U., and Balogh, A., Cluster observation of a bifurcated current sheet, *Geophys. Res. Lett.*, **30**, 2, 1036, (2003)

[81] Runov, A., Nakamura, R., Baumjohann, W., Treumann, R. A., Zhang, T. L., Volwerk, M. , V*ö*r*ö*s, Z., Balogh, Gla*β*meier, K. H., Klecker, B., R*é*me, H., and Kistler, L., Current sheet structure near magnetic X-line observed by Cluster, *Geophys. Res. Lett.*, **30**, 11, 1579, (2003)

[82] Runov, A., Sergeev, V. A., Nakamura, R., Baumjohann, W., V*ö*r*ö*s, Z., Volwerk, M., Asano, B., Klecker, B., R*é*me, H., Balogh, A., Properties of a bifurcated current sheet observed on august 29, 2001, *Ann. Geophys.*, **22**, 2535, (2004)

[83] Runov, A., Nakamura, R., Baumjohann, W., Zhang, T. L., Volwerk, M., Eichelberger, H., Balogh, A., Cluster observations of a bifurcated current sheet, *Geophys. Res. Lett.*, **30**, 1036, (2005)

[84] Runov, A., Sergeev, V. A., Nakamura, R., Baumjohann, W., Zhang, T. L., Asano, B., Volwerk, M., V*ö*r*ö*s, Z., Balogh, A., R*é*me, H., Reconstruction of the magnetotail current sheet structure using multi-point Cluster measurements, *Planetary Space Sci.*, **53**, 237, (2005)

[85] Runov, A., Sergeev, V. A., Baumjohann, W., Nakamura, R., Apatenkov, S., Asano, B., Volwerk, M., V*ö*r*ö*s, Z., Zhang, T. L., Petrukovich, A., Balogh, A., Sauvaud, J. A., Klecker, B., R*é*me, H., Electric and magnetic field geometry in flapping magnetic current sheets, *Ann. Geophys.*, **23**, 1391, (2005)

[86] Runov, A., Sergeev, V. A., Nakamura, R., Baumjohann, W., Apatenkov, S., Asano, Y., Takada, T., Volwerk, M., V*ö*r*ö*s, Z., Zhang, T. L., Sauvaud, J. A., R*é*me, H., Balogh, A., Local structure of the

magnetotail current sheet: 2001 Cluster observations, *Ann. Geophys.*, **24**, 247, (2006)

[87] Sanny, J., McPherron, R. L., Russell, C. T., Baker, D. N., Pulkkinen T. I., Nishida, A., Growth-phase thinning of the near-Earth current sheet during the CDAW 6 substorm, *J. Geophys. Res.*, **99**, 5805, (1994)

[88] Schindler, K., Birn, J., Models of two-dimensional embedded thin current sheets from Vlasov theory, *J. Geophys. Res.*, **107**, A8, 1193, (2002)

[89] Schriver, D., Ashour-Abdalla, M., Richard, R. L., On the origin of the ion-electron temperature difference in the plasma sheet, *J. Geophys. Res.*, **103**, A7, 14 879, (1998)

[90] Sergeev, V. A., Mitchell, D. G., Russell, C. T., Williams, D. J., Structure of the tail plasma/current sheet at 11 R_E and its changes in the course of a substorm, *J. Geophys. Res.*, **98**, 17 345, (1993)

[91] Sergeev, V. A., Runov, A., Baumjohann et al., Current sheet flapping motion and structure observed by Cluster, *Geophys. Res. Lett.*, **30**, 1327, (2003)

[92] Sitnov, M. I., Zelenyi, L. M., Thin current sheet embedded within a thicker plasma sheet: Self-consistent kinetic theory, *J. Geophys. Res.*, **105**, 13029, (2000)

[93] Sitnov, M. I., Guzdar, P. N., and Swisdak, M.: A model of the bifurcated current sheet, *Geophys. Res. Lett.*, **30**, 13, 1712, (2003)

[94] Sitnov, M. I., Swisdak, M., Drake J. F., Guzdar, P. N., Rogers, B. N., A model of the bifurcated current sheet: Flapping motions, *Geophys. Res. Lett.*, **31**, L09805, (2004)

[95] Sitnov, M. I., Swisdak, M., Guzdar, P. N., Runov, A., Structure and dynamics of a new class of thin current sheets, *J. Geophys. Res.*, **111**, (2006)

[96] Slavin, J. A., Smith, E. J., Sibeck, D. G., Baker, D. N., Zwickl, R. D., Akasofu, S. I., An ISEE 3 study of average and substorm conditions in the distant magnetotail, *J. Geophys. Res.*, **90**, 10 875, (1985)

[97] Speiser, T. W., Perticle trajectories in model current sheets, 1. Analytical solution, *J. Geophys. Res.*, **70**, 17, 4219 (1965)

[98] Spiegelmann, M., Katz, R. F., A Semi-Lagrangian Crank-Nicolson algorithm for the numerical solution of advection-diffusion problems, *Geochem. Geophys. Geosyst.*, **7**, Q04014, (2006)

[99] Staniforth, A., Côté, J., Semi-lagrangian Integration Schemes for Atmosferic Models–A Review, *Monthly Weather Review*, **119**, 2206-2223, (1991)

[100] Steinhauer, L. C., End-shorting and electric field in edge plasmas with application to field-reversed configurations, *Phys. Plasma*, **9**, 3851-3856, (2002)

[101] Strain, J., Semi-lagrangian methods for level set equations, *J. Comp. Phys.*, **151**, 498-533, (1999)

[102] Swift, D. W., Use of a hybrid code for global-scale plasma simulation, *J. Comp. Phys.*, **126**, 109, (1996)

[103] Taktakisvili et al.: Ion dynamics in the magnetotail current sheet: opposite effects of magnetic turbulence and normal component, *J. Atmos. Sol. Terr. Phys.*, **65**, 315-322, (2003)

[104] Thomas, V. A., Winske, D., Omidi, N., Reforming supercritical quasi-parallel shocks: 1. One-dimensional simulations, *J. Geophys. Res.*, **95**, 18809, (1990)

[105] Thompson, S. M., Kivelson, M. G., Khurana, K.K., McPherron, R. L., Weygand, J. M., Balogh, A., Réme, H., Kistler, L. M., Dynamic Harris current sheet thickness from Cluster current density and plasma measurements, *J. Geophys. Res.*, **110**, (2005)

[106] Veltri, P., Zimbardo, G., Taktakishvili, A. L., Zelenyi, L. M., Effect of magnetic turbulence on the ion dynamics in the distant magnetotail, *J. Geophys. Res.*, **103**, A7, 14897-14910, (1998)

[107] Wiegelmann, T., Büuchner, J., Kinetic simulations of the coupling between current instabilities and reconnection in thin current sheets, *Nonl. Proc. Geophys.*, **7**, 141, (2000)

[108] Winske, D., Hybrid simulation codes with application to shocks and upstream waves, *Space Sci. Rev.*, **42**, 1-2, 53-66, (1985)

[109] Winske, D., Yin, L., Omidi, N., Karimabadi, H., Quest, K. B., Hybrid simulations Codes: Past. Present and Future - Tutorial, Space Plasma

Simulations, Büuchner, J., Dum, C. T., Scholer, M., eds., Lecture Notes in Physics, 615, 359, Springer, Berlin Heidelberg New York, /(2003)

[110] Yamada, M., Ji, H., Hsu, S., Carter, T., Kulsrud, R., Trintchouk, F., Experimental investigation of the neutral sheet profile during magnetic reconnection, *Phys. Plasma*, **7**, 1781, (2000)

[111] Yin, L., Winske, D., Gary, S. P., Birn, J., Hybrid and Hall-MHD simulations of collisionless reconnection: Effects of plasma pressure tensor, *Proceedings of ISSS-6*, 1-4, Copernicus Gesellschaft, (2001)

[112] Zelenyi, L. M, Sitnov, M. I., Malova, H. V., Sharma, A. S., Thin and superthin ion current sheets. Quasi-adiabatic and non adiabatic models, *Nonl. Proc. Geophys.*, **7**, 127, (2000)

[113] Zelenyi, L. M, Delcourt, D., Malova, H. V., and Sharma, A. S.: "Aging" of the magnetotail thin current sheets, *Geophys. Res. Lett.*, **29**, 10, 1029, (2002)

[114] Zelenyi, L. M, Malova, H. V., and Popov, V. Yu.: Bifurcation of thin current sheets in the Earth's magnetosphere, *JETP Lett.*, **78**, 296, (2003)

[115] Zelenyi, L. M, Malova, H. V., Popov, V. Yu., Delcourt, D., and Sharma, A. S.: Nonlinear equilibrium structure of thin current sheets: influence of electron pressure anisotropy, *Nonl. Proc. Geophys.*, **11**, 579-587, (2004)

[116] Zimbardo, G., Greco, A., Veltri, P., Taktakishvili, A. L., Zelenyi, L. M., Double peak structure and diamagnetic wings of the magnetotail current sheet, *Ann. Geophys.*, **22**, 2541, (2004)